

Dissertation

submitted to the
Combined Faculty of Mathematics, Engineering and Natural Sciences
of Heidelberg University, Germany
for the degree of
Doctor of Natural Sciences

Put forward by
M. Sc. Tobias Valentin Heldt
born in: Ostfildern
Oral examination: 07.05.2025

Femtosecond electron dynamics driven by ponderomotive gradients

Referees: Apl. Prof. Dr. José R. Crespo López-Urrutia
Prof. Dr. Selim Jochim

Femtosecond electron dynamics driven by ponderomotive gradients

Electrons driven by the oscillating electric field of intense femtosecond laser pulses experience an effective cycle-averaged ponderomotive potential. This thesis investigates the ponderomotive effects of circularly polarized few-cycle pulses and standing waves on photoionization, photoemission, and the subsequent electron motion. Reconstructing the time-dependent dipole moment of recolliding electron wave packets from an extreme ultraviolet absorption spectrum reveals an envelope-driven recollision channel in circularly polarized light, as predicted by the theory of recolliding periodic orbits. Furthermore, tomography of photoelectron angular distributions is achieved using velocity-map imaging within a femtosecond enhancement cavity operating at 100 MHz. This cavity supports two counter-propagating pulses that form a transient standing wave at the focus. Exploiting the standing wave structure allows to probe the photoemission at different crystal facets of a tungsten nanotip and to minimize the source volume of above-threshold ionization. In addition, the high-intensity Kapitza-Dirac effect for resonantly ionized electrons in the picosecond regime is presented together with still unexplained diffraction results for femtosecond pulses. The intense intra-cavity standing waves are a promising tool for coherent control of electron matter waves, potentially advancing the development of a femtosecond electron interferometer at low energies.

Femtosekunden Elektronendynamik getrieben durch ponderomotorische Gradienten

Elektronen, die durch das oszillierende elektrische Feld intensiver Femtosekundenlaserpulse angetrieben werden, erfahren ein effektives zyklusgemittelttes ponderomotives Potenzial. In dieser Arbeit werden die ponderomotorischen Effekte von zirkular polarisierten Lichtpulsen mit wenigen Zyklen und stehenden Wellen auf Photoionisation, Photoemission und die anschließende Elektronenbewegung untersucht. Die Rekonstruktion des zeitabhängigen Dipolmoments von rekollidierenden Elektronenwellenpaketen aus einem XUV-Absorptionsspektrum zeigt einen Rekollisionskanal in zirkular polarisiertem Licht, getrieben von der Pulseinhüllenden, wie er von der Theorie der rekollidierenden periodischen Bahnen vorhergesagt wurde. Darüber hinaus wird die Tomographie von Photoelektronen-Winkelverteilungen mit Hilfe von Geschwindigkeitsabbildungen in einer Femtosekunden-Verstärkungskavität, die bei 100 MHz arbeitet, erreicht. Diese Kavität unterstützt zwei gegenläufige Pulse, die im Fokus vorübergehend eine stehende Welle bilden. Die Ausnutzung der Knotenstruktur der stehenden Welle ermöglicht es, die Photoemission an verschiedenen Kristalloberflächen einer Wolfram-Nanospitze zu untersuchen und das Quellvolumen von Überschwellen-Ionisation zu minimieren. Darüber hinaus wird der hochintensive Kapitza-Dirac-Effekt für resonant ionisierte Elektronen im Pikosekundenbereich zusammen mit noch unerklärten Beugungsergebnissen für Femtosekundenpulse vorgestellt. Die intensiven stehenden Wellen innerhalb von Kavitäten sind ein vielversprechendes Werkzeug für die kohärente Kontrolle von Elektronenmateriewellen und könnten die Entwicklung eines Femtosekunden-Elektroneninterferometers bei niedrigen Energien vorantreiben.

List of publications

This thesis is based on the following published articles:

- **T. Heldt**, J. Dubois, P. Birk, G. D. Borisova, G. M. Lando, C. Ott, and T. Pfeifer, "Attosecond real-time observation of recolliding electron trajectories in helium at low laser intensities", *Physical Review Letters*, 130, 183201 (2023). DOI: 10.1103/PhysRevLett.130.183201.
- J.-H. Oelmann, **T. Heldt**, L. Guth, J. Nauta, N. Lackmann, V. Wössner, S. Kokh, T. Pfeifer, and J. R. Crespo López-Urrutia., "Photoelectron tomography with an intra-cavity velocity-map imaging spectrometer at 100 MHz repetition rate", *Review of Scientific Instruments*, 93, 123303, (2022). DOI: 10.1063/5.0104679.
- **T. Heldt**, J.-H. Oelmann, L. Guth, N. Lackmann, L. Matt, T. Pfeifer, and J. R. Crespo López-Urrutia, "Nanometric probing with a femtosecond, intra-cavity standing wave", *Nanophotonics*, 13, 25, 4639-4646, (2024). DOI: 10.1515/nanoph-2024-0332.
- **T. Heldt**, J.-H. Oelmann, L. Guth, N. Lackmann, T. Pfeifer, and J. R. Crespo López-Urrutia, "Velocity-map imaging with counter-propagating laser pulses", *Optics Letters*, 49, 23, 6825-6828 (2024). DOI: 10.1364/OL.540612.

Additional publications with own contributions:

- **T. Heldt**, C. Ott, and T. Pfeifer, J. Dubois, "Elektronenbewegung fotografiert", *Physik in unserer Zeit*, 54, 5, 218-219, (2023). DOI: 10.1002/piuz.202370507.
- **T. Heldt**, J.-H. Oelmann, L. Guth, N. Lackmann, J. Nauta, T. Pfeifer, and J. R. Crespo López-Urrutia, "Intra-cavity femtosecond standing waves for multiphoton pump-probe experiments at 100 MHz", 2023 Conference on Lasers and Electro-Optics Europe and European Quantum Electronics Conference (2023). DOI: 10.1109/cleo/europe-eqec57999.2023.10232698.
- J.-H. Oelmann, L. Guth, **T. Heldt**, N. Griesbach, R. Hector, N. Lackmann, J. Nauta, T. Pfeifer, and J. R. Crespo López-Urrutia, "Closed-cycle noble gas recycling system for high-repetition rate high-harmonic generation", *Review of Scientific Instruments*, 95, 035115, (2024). DOI: 10.1063/5.0176563.
- P. Birk, V. Stooß; M. Hartmann, G. D. Borisova, A. Blättermann, **T. Heldt**, K. Bartschat, C. Ott, and T. Pfeifer, "Attosecond transient absorption of a continuum threshold", *Journal of Physics B: Atomic, Molecular and Optical Physics*, 53 ,12 , 124002, (2020). DOI: 10.1088/1361-6455/ab7c3f.
- G. D. Borisova, V. Stooß, A. Dingeldey, A. Kaldun, T. Ding, P. Birk, M. Hartmann, **T. Heldt**, C. Ott, and T. Pfeifer, "Strong-field-induced single and double ionization dynamics from single and double excitations in a two-electron atom", *Journal of Physics Communications*, 4, 5, 055012, (2024). DOI: 10.1088/2399-6528/ab6175.

Contents

1	Introduction	1
2	Theoretical background	5
2.1	Ultrashort pulses and frequency combs	5
2.1.1	The wave equation and linear absorption	5
2.1.2	Ultrashort pulses	8
2.1.3	Frequency combs	11
2.2	Optical cavities	13
2.2.1	Longitudinal modes	13
2.2.2	Femtosecond enhancement cavities	15
2.2.3	Transverse modes	17
2.3	Strong-field light-matter interaction	19
2.3.1	Schrödinger equation	19
2.3.2	Ionization in intense laser fields	22
2.3.3	Photoemission from metals	25
2.3.4	Electron diffraction in standing waves - The Kapitza-Dirac effect	27
3	Publications	31
3.1	Attosecond real-time observation of recolliding electron trajectories in helium at low laser intensities	32
3.2	Photoelectron tomography with an intra-cavity VMI spectrometer at 100 MHz	42
3.3	Nanometric probing with a femtosecond, intra-cavity standing wave	55
3.4	Velocity-map imaging with counter-propagating laser pulses	64
4	Prospects of strong standing waves for Kapitza-Dirac experiments	69
4.1	High-intensity Kapitza-Dirac effect in the literature	69
4.2	State-resolved high-intensity Kapitza-Dirac effect	70
4.2.1	Classical electron trajectories in standing waves	73
4.3	Observed effects of a standing wave on ATI for femtosecond pulses	74
4.3.1	Influence of the ionization position on the electron momentum	77
5	Concluding discussion	79
5.1	Measuring electron dynamics at the atomic scale	79
5.2	Femtosecond enhancement cavities for MHz-rate strong-field studies	80
5.3	A velocity-map imaging spectrometer for intra-cavity strong-field experiments	82
5.4	Studying nanometric objects and crystal structure with intra-cavity standing waves	82
5.5	Standing waves for above-threshold ionization	85
5.6	Ponderomotive control of slow electron matter waves	86
6	Summary	87
	Bibliography	89
	Acknowledgments	101

List of Figures

2.1	Difference between traveling and standing waves	7
2.2	Buildup of a mode-locked laser pulse	9
2.3	Influence of the spectral phase on an ultrashort pulse	10
2.4	Frequency combs in the energy and time domain	12
2.5	Airy distribution of the cavity enhancement	14
2.6	Femtosecond enhancement cavities	16
2.7	Gaussian beam	18
2.8	Split-operator method	20
2.9	Strong-field ionization	23
2.10	Different regimes of photoemission at sharp metallic tips	26
2.11	Kapitza-Dirac effect	28
4.1	The high-intensity Kapitza-Dirac effect measured by Bucksbaum <i>et al.</i>	69
4.2	VMI of xenon revealing the high-intensity Kapitza-Dirac effect	71
4.3	Monte Carlo simulation of classical electron trajectories in standing waves	72
4.4	Intensity-dependent comparison of ATI in traveling and standing waves	75
4.5	Tunnel ionization with a standing wave	76
4.6	Dependence of the ionization position on ATI signal	77
5.1	Back action of the tip on the cavity	84
5.2	Intensity doubling in a standing wave	85

Acronyms

ATAS	attosecond transient absorption spectroscopy
ATI	above-threshold ionization
ATP	above-threshold photoemission
CC	channel closing
CEP	carrier-envelope phase
CW	continuous wave
FDTD	finite-difference time-domain
FEM	field-emission microscopy
FFT	fast Fourier transform
FIM	field-ion microscopy
FSR	free spectral range
FWHM	full width at half maximum
GD	group delay
GDD	group delay dispersion
HHG	high-harmonic generation
LIED	laser-induced electron diffraction
MCP	microchannel plate
MPI	multiphoton ionization
NIR	near-infrared
OBI	over-the-barrier ionization
PAD	photoelectron angular distribution
PINEM	photon-induced near-field electron microscopy
REMI	reaction microscope
SEM	scanning electron microscopy
SFA	strong-field approximation
STED	stimulated emission depletion
STM	scanning tunneling microscope
TBP	time-bandwidth product
TDSE	time-dependent Schrödinger equation
TEM	transmission electron microscopy
TI	tunnel ionization
TOD	third-order dispersion
VMI	velocity-map imaging
XUV	extreme ultraviolet

1 Introduction

Light not only allows us to see the beauty of the world, it carries energy from the Sun nourishing life on our Earth and it offers us a glimpse into the mysteries of the ancient universe. Since the Stone Age, humankind has sought to control light, starting with campfires and progressing to candles and electric bulbs for illumination. For our modern technology, light has become a common indispensable tool for precision measurements, material processing, medical applications, communication, and even the cheapest energy source available [1].

The phenomena of light-matter interaction, including absorption, diffraction, and dispersion, give rise to stunning natural spectacles such as sunsets and rainbows. At the same time, excessive solar radiation can lead to severe consequences, ranging from sunburns to droughts and desertification. However, for all these effects we observe in nature, the light is weak from a physical point of view. It interacts linearly with matter, causing only a small perturbation to the strong bonds between nuclei and electrons. Only the invention of the laser [2] allowed entry into the world of nonlinear optics [3]. Pushing the light intensities higher and higher eventually led to the regime of strong fields, where the light no longer just tickles the matter, but really shakes it. In this regime, the electric field of the light becomes comparable to atomic fields, which significantly alters the matter, at least during the interaction time. In order to achieve the required intensities, it is not enough to focus the light to a small spot, it is also necessary to temporally compress the light energy into a short pulse. Why is it interesting to study this regime of intense light and ultrashort pulses, far from everyday experience? The cycle of the light limits the duration of the shortest optical pulses to a few femtoseconds, where $1 \text{ fs} = 10^{-15} \text{ s}$. This corresponds to the relevant time scale for many atomic and molecular processes. Thus, these short, intense pulses can trigger dynamics in quantum systems to study, or even control them, in a time-resolved manner.

The central objective of this work is to better understand the response of electrons to intense light pulses. Given the small mass of electrons, most of the effects induced by light in matter can be attributed to them. The electron response strongly depends on their environment — whether free, quasi-free (i.e., within the Coulomb potential of an ion but with enough energy to escape), bound, or even delocalized in the band structure of a solid. This dissertation explores all of these regimes.

Among the numerous aspects of light that can be studied, this thesis specifically focuses on different types of intensity gradients of light. A spatial gradient implies structure, while a time-dependent gradient suggests dynamics. Both lead to interesting phenomena, appearing across various scales. Although the electric field of light oscillates at frequency ω , the intensity is cycle-averaged and proportional to the square of the field envelope. Thus, a strong temporal gradient can be found at the rising and falling edges of a short pulse. A standing wave builds up a pronounced subcycle structure with strong spatial gradients between nodes of vanishing intensity and antinodes of maximum intensity. And on a much longer length scale, the intensity of light changes as it passes through a focus. All these cases are investigated in this thesis.

One of the most direct ways to study strong-field light-matter interactions is to focus

1 Introduction

a strong optical or near-infrared (NIR) laser pulse into a cloud of gas atoms in vacuum and detect the ionized electrons. For noble gases, the photon energy is lower than the ionization potential. Therefore, in multiphoton ionization (MPI), an atom absorbs many photons until their combined energy exceeds the ionization threshold. Experimental electron spectra consist of several peaks spaced by the photon energy $\hbar\omega$, demonstrating that additional photons can be absorbed beyond the minimum required for MPI, a phenomenon called above-threshold ionization (ATI) [4]. Analysis of these spectra revealed the significance of the ponderomotive energy, which is the average kinetic energy of an electron quivering in an electromagnetic field [5, 6]. This ponderomotive energy, or potential, which is proportional to the laser intensity, is a central quantity in this thesis.

Both MPI and ATI can still be described using high-order perturbation theory. However, even before the first experimental realization, Keldysh [7] had published a theory that proposed a regime beyond MPI and ATI, namely tunnel ionization (TI). When the transition to this regime of even higher intensity was investigated, unexpected results were found, such as a plateau for high-harmonic generation (HHG) [8] or a "knee" in non-sequential double ionization [9, 10]. These findings could finally be explained by the concept of ionized electrons being driven back to their parent ion by the field, resulting in a recollision. This mechanism was first described in a semiclassical framework [11] and later formulated in a fully quantum mechanical theory [12, 13]. The importance of these recollisions cannot be overstated. First, the physical process itself is interesting because it probes the atom not only with light, but also with a coherent electron originating from the same atom, effectively making recollisions a driven scattering experiment. Second, the model of driven electron trajectories successfully explains many observations, supporting the validity of an intuitive classical picture in the strong-field regime. Third, the HHG resulting from these recollisions has become the workhorse for an entire scientific community dedicated to study quantum mechanics on the native electronic timescale in attosecond physics ($1 \text{ as} = 10^{-18} \text{ s}$). The significance of this tool was recognized in 2023 with the Nobel Prize in Physics [14].

The availability of a tabletop, broadband, attosecond extreme ultraviolet (XUV) light source from HHG has also led to the development of a new method known as attosecond transient absorption spectroscopy (ATAS) [15–17]. This technique captures transient dynamics by measuring the absorption spectrum of XUV light while scanning the delay of a strong femtosecond NIR pulse that interacts with the medium. ATAS has proven to be a valuable tool to study bound transitions in atoms [18–20], molecules [21, 22] or solids [23, 24]. The phase changes introduced by a strong light pulse are accessible [25], and Stooß *et al.* [26] have shown that, under certain conditions, the time-dependent dipole moment can be extracted without a delay sweep. All-optical ATAS has become a state-of-the-art method for investigating bound transitions, complementary to approaches that detect charged fragments, such as electrons or ions, to study dynamics with final states in the continuum.

Methods for measuring the spectra of charged particles have also evolved significantly from initial retarding potential techniques [4], time of flight, or deflecting field methods [27]. The development of reaction microscopes, which detect electrons in coincidence with ions for a solid angle of 4π , allows the kinematically complete observation of scattering processes [28, 29]. Velocity-map imaging (VMI), introduced by Parker and Eppink [30], is another powerful method that employs an electrostatic lens to measure angularly resolved momentum projections with a 4π solid angle. Due to its reduced complexity compared to coincidence schemes and robust operation without count rate constraints,

VMI is now widely used for strong-field experiments [31–34].

The first part of this thesis utilizes ATAS, not for the study of bound states, but of the continuum. In contrast to fragment detection, this approach focuses on the time-resolved recollision process itself rather than the final momenta. HHG spectroscopy, which extracts information about matter from the HHG signal [35–38], could be considered methodologically similar. However, the approach presented here provides additional temporal control over the ionization step, which was crucial for the results obtained.

The second part of the thesis employs a VMI spectrometer to study photoelectrons emitted due to intense, ultrafast standing waves. In addition to a high-power NIR frequency comb, the key technology for generating such light is a femtosecond enhancement cavity, which coherently superimposes ultrashort pulses. While conventional laser systems for free-space strong-field studies typically operate at kilohertz repetition rates, cavity enhancement enables reaching the required intensities of $\sim 10^{13}$ W/cm² even at 100 MHz. This high repetition rate facilitates the study of processes with small cross sections or those at the low-intensity onset of strong-field physics [39]. HHG in such femtosecond enhancement cavities can transfer the coherence of the fundamental NIR frequency comb to the XUV regime [40–42]. These XUV frequency combs are highly promising light sources for precision spectroscopy in a spectral range where narrowband lasers are not available [43]. Interesting targets include the thorium-229 isotope, which has a isomeric state at 8.2 eV that could be used for a nuclear clock [44–46], or highly charged ions [42, 47–49].

The ring cavity utilized in this thesis has a unique feature: it supports coupling of light into both directions, enabling photoionization studies as a function of light direction. In the dipole approximation, there should be no directional dependence, but recent studies have demonstrated that electric and magnetic nondipole contributions directionally affect strong-field ionization [50–53]. Simultaneously coupling light into both propagation directions generates two counter-propagating pulses, which form an intense, transient standing wave at the focus when they overlap. Standing waves are fascinating because they can interact with free electrons through the Kapitza-Dirac effect. This phenomenon, originally proposed in 1933 by Kapitza and Dirac [54], describes the diffraction of matter by a grating of light. It can be understood in a particle picture as stimulated Compton scattering or in a wave picture as matter wave diffraction (for details, see Subsec. 2.3.4). Beyond the conceptually intriguing idea of reversing the roles of light and matter gratings in normal diffraction, this effect could advance modern technologies such as electron microscopy, by exploiting the quantum nature of electrons. There are already promising examples in ultrafast transmission electron microscopy (UTEM) that utilize photon-electron interactions for impressive time-resolved spectroscopy [55–59], recently even with interferometry of fast electrons [60, 61]. The demonstration of the ultrafast Kapitza-Dirac effect [62], where a time-delayed standing wave leads to a coherent superposition of two momentum wave packets, is a very promising step towards a femtosecond electron interferometer with slow electrons, which could open a new door to probe matter.

After this general introduction, Chapter 2 introduces the relevant fundamental physical concepts, including the theory of ultrashort laser pulses, their enhancement in optical cavities, and the foundation of strong-field light-matter interaction.

Chapter 3 presents the main results of this thesis, summarized in four publications, ordered from the smallest to the largest length scale studied. Publication 3.1 employs ATAS to investigate the recollision dynamics of a quasi-free electron wave packet in the

1 Introduction

vicinity of its parent helium ion. A theoretically predicted recollision channel for circularly polarized light, enabled by a small field envelope at the time of ionization, is confirmed. In Sec. 3.2 the methodology shifts from an all-optical approach to the detection of electrons. A detailed description of the VMI electron spectrometer is given, and the tomographic reconstruction of 3D photoelectron angular distributions, triggered by a 100-MHz intracavity frequency comb, is demonstrated. Publication 3.3 uses the same setup to explore the photofield electron emission of a tungsten nanotip in a standing wave. The strong gradients in the node-antinode pattern can shift the angle of photoemission depending on the phase of the wave, proving that structured light can probe the nanometric crystal structure. Publication 3.4 studies the highly nonlinear ATI of xenon in the same intense, transient standing waves. The counter-propagating pulses transfer their temporal width into the spatial intensity distribution along the beam propagation axis, leading to a strongly confined ionization volume and a doubled maximum intensity.

Chapter 4 reports unpublished experimental results on high-intensity Kapitza-Dirac electron diffraction by comparing ATI photoelectron spectra ionized in traveling and standing waves. In the case of picosecond pulses, which lead to the classical rainbow scattering regime, state-selective electron diffraction has been observed by exploiting Freeman resonances during ionization. For femtosecond pulses, standing waves also modify the photoionization spectra, but a theoretical description has yet to be developed.

Chapter 5 discusses all the work of this thesis, highlighting connections between the publications and raising further questions. Finally, Chapter 6 gives a summary of the main results.

2 Theoretical background

The purpose of this chapter is to introduce the key concepts of this thesis, namely the description of ultrashort pulses, the fascinating properties of optical cavities and the interaction of light with matter in the limit of strong light fields. The discussion is deliberately kept brief, with no claim to completeness.

2.1 Ultrashort pulses and frequency combs

This section summarizes how to describe the electric field for laser pulses in the time and frequency domain. Starting with the wave equation for the electric field, plane waves are introduced as a solution. By summing these plane waves, the generation of ultrashort pulses is explained. At the end, frequency combs are discussed as the natural description of an ideal mode-locked pulsed laser in the frequency domain. For a more detailed description, refer to [63–65].

2.1.1 The wave equation and linear absorption

For a nonmagnetic dielectric medium, the wave equation of the electric field \mathbf{E} follows directly from Maxwell's equations

$$\Delta \mathbf{E} - \frac{1}{c^2} \frac{\partial^2}{\partial t^2} \mathbf{E} = \mu_0 \frac{\partial^2}{\partial t^2} \mathbf{P}, \quad (2.1)$$

with the Laplace operator Δ and the speed of light c connected to the vacuum permittivity ϵ_0 and the vacuum permeability μ_0 by $c^2 = \epsilon_0 \mu_0$. In general, the polarization \mathbf{P} of a medium is a nonlinear function of the electric field. A Taylor expansion allows to express the polarization in the perturbative regime as a function of the field

$$\mathbf{P} = \underbrace{\epsilon_0 \chi^{(1)} \mathbf{E}}_{\mathbf{P}_L} + \underbrace{\epsilon_0 \chi^{(2)} \mathbf{E}^2 + \epsilon_0 \chi^{(3)} \mathbf{E}^3 + \dots}_{\mathbf{P}_{NL}} \quad . \quad (2.2)$$

The n -th order susceptibilities $\chi^{(n)}$ are material properties represented as tensors. They become scalars in the homogeneous, isotropic media discussed here for simplicity. For most light sources, experienced in everyday life, the field amplitudes are so small that the nonlinear part \mathbf{P}_{NL} can be neglected. In linear optics, the electric susceptibility $\chi^{(1)}$ is the only relevant contribution, so $\chi = \chi^{(1)}$. It is in general frequency dependent, so that polarization can be best described in the frequency domain

$$\mathbf{P}(\omega) = \mathbf{P}_L(\omega) = \epsilon_0 \chi(\omega) \mathbf{E}(\omega). \quad (2.3)$$

The refractive index of a medium is then defined by $n(\omega) = \sqrt{1 + \chi(\omega)}$. Considering the dispersion-free case of $\chi(\omega) = \text{const.}$, the wave Eq. (2.1) can be written in the linear

2 Theoretical background

regime as

$$\Delta \mathbf{E} - \frac{1}{c_n^2} \frac{\partial^2}{\partial t^2} \mathbf{E} = 0, \quad (2.4)$$

with the speed of light in a medium $c_n = c/n$.

Plane waves as solutions to the wave equation

Assuming an eigenmode ansatz of the form $\mathbf{E}(\mathbf{r}, t) = e^{-i\omega t} \tilde{\mathbf{E}}(\mathbf{r})$, results in the Helmholtz equation

$$\nabla^2 \tilde{\mathbf{E}}(\mathbf{r}) = - \left(\frac{\omega}{c_n} \right)^2 \tilde{\mathbf{E}}(\mathbf{r}). \quad (2.5)$$

For the one-dimensional case with propagation along the z -axis, the plane-wave solutions $\tilde{\mathbf{E}}(z) = \mathbf{E}_0^\pm e^{\pm ikz}$ can be used to write the electric field as

$$\mathbf{E}(z, t) = \mathbf{E}_0^+ e^{i(\omega t - kz)} + \mathbf{E}_0^- e^{i(\omega t + kz)}, \quad (2.6)$$

introducing the wave number $k = \omega/c_n = 2\pi/\lambda$. Here, $\mathbf{E}_0^\pm = |\mathbf{E}_0^\pm| e^{i\phi^\pm}$ are complex amplitudes with the phase ϕ^\pm for waves traveling in the positive z -direction (\mathbf{E}_0^+) and in the negative z -direction (\mathbf{E}_0^-), respectively. Since the wave equation is linear, any linear combination of solutions are also solutions, which gives rise to the well known superposition principle. This can also be used to calculate back to real valued fields by adding the complex conjugate (c.c.)

$$|\mathbf{E}_0^+| \cos(\omega t - kz) = \frac{1}{2} \left[\mathbf{E}_0^+ e^{i(\omega t - kz)} + \text{c.c.} \right] = \frac{1}{2} \left[\mathbf{E}_0^+ e^{i(\omega t - kz)} + (\mathbf{E}_0^+)^* e^{-i(\omega t - kz)} \right]. \quad (2.7)$$

Inserting the plane wave solution into Maxwell's equation shows that the electric field has to be orthogonal to the propagation direction $\mathbf{k} \perp \mathbf{E}$. If the propagation is set along the z -direction, this leads to the general case of an elliptical polarized plane wave

$$\mathbf{E} = \begin{pmatrix} E_x \\ E_y e^{i\Phi} \\ 0 \end{pmatrix} e^{i(\omega t - kz)}. \quad (2.8)$$

For $\Phi = n\pi$ with $n \in \mathbb{Z}$, or if either E_x or E_y equal zero, the wave is linearly polarized. In the special case of equal amplitudes $E_x = E_y$ and a phase shift of $\Phi = (2n + 1)\pi/2$ with $n \in \mathbb{Z}$, the wave is circularly polarized and the field vector moves around a circle.

The magnetic field \mathbf{B} of the electromagnetic wave is not discussed here in detail. It oscillates in phase with the electric field and for a plane wave $\mathbf{k} \times \mathbf{E} = \omega \mathbf{B}$.

Standing waves

If two plane waves are counter-propagating with the same amplitude \mathbf{E}_0 and polarization, they interfere and form a standing wave

$$\mathbf{E}(z, t) = \mathbf{E}_0 (e^{i(\omega t - kz)} + e^{i(\omega t + kz)}) = 2\mathbf{E}_0 \cos(kz) e^{i\omega t}. \quad (2.9)$$

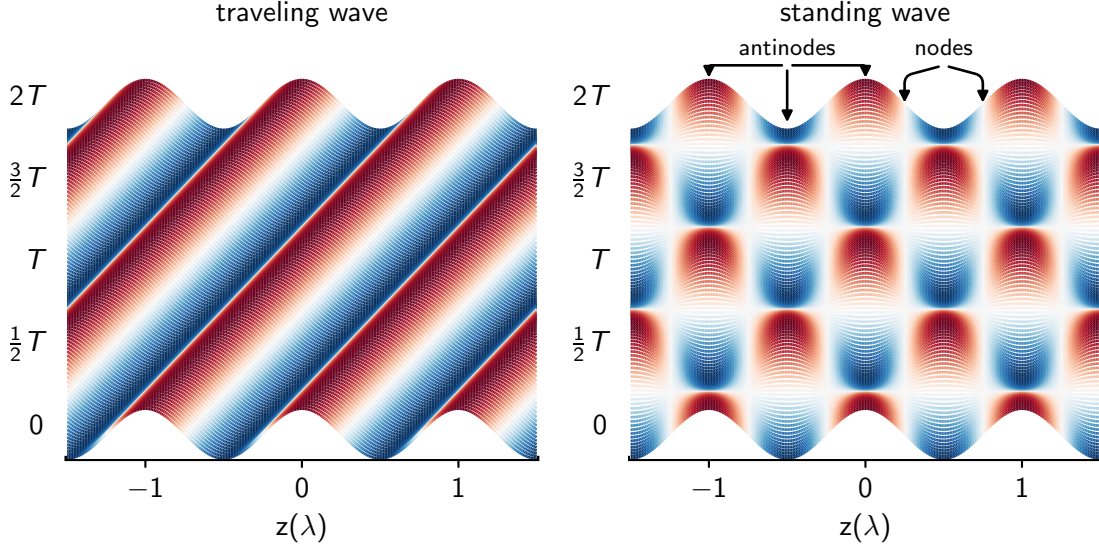


Figure 2.1: Time evolution of a traveling plane wave and of a standing wave, which is formed by two counter-propagating plane waves. The oscillation period is T , the wavelength λ .

For this type of wave, the amplitude is modulated along the propagation axis. As illustrated in Fig. 2.1, there are specific points in space, given by $z = n\lambda/2$ with $n \in \mathbb{Z}$, that have maximum amplitude. These points are called antinodes. Conversely, precisely midway between two antinodes, the electric field is always zero, defining a node.

The role of the dipole moment in linear absorption

For an isotropic gas in the linear optics regime, given by Eq. (2.3), the macroscopic polarization is related to the atomic dipole moment $d(\omega)$ by the atomic number density ρ_N

$$P(\omega) = \rho_N d(\omega). \quad (2.10)$$

If the medium is sufficiently dilute, the polarization and the electric susceptibility are small and the refractive index can be approximated by

$$n(\omega) \approx 1 + \frac{\Re[\chi(\omega)]}{2} + i\frac{\Im[\chi(\omega)]}{2}. \quad (2.11)$$

The real part $\Re[\chi(\omega)]$ leads to diffraction and the imaginary part $\Im[\chi(\omega)]$ is related to absorption in the medium. An absorption coefficient can be defined as

$$\alpha_L(\omega) = \frac{\omega}{c} \Im[\chi(\omega)]. \quad (2.12)$$

The total absorption after propagating for a length z through a medium is called the optical density or absorbance $A(\omega)$. It is defined by the ratio of the transmitted intensity to the original intensity, given by the Beer-Lambert law as

$$\frac{I(\omega, z)}{I(\omega, 0)} = 10^{-A(\omega)} = e^{-\alpha_L(\omega)z}, \quad (2.13)$$

2 Theoretical background

where the intensity is given by

$$I = \frac{c_n \epsilon_0}{2} |E|^2. \quad (2.14)$$

Since $\chi(\omega) \propto P(\omega)/E(\omega)$, Eq. (2.10) allows to link the experimentally measurable quantity absorbance to the atomic dipole moment by

$$A(\omega) \propto \omega \Im \left[\frac{d(\omega)}{E(\omega)} \right]. \quad (2.15)$$

For ultrafast processes, it is instructive to consider the dipole moment in the time domain, expressed as $d(t) = \mathcal{F}\{d(\omega)\}$, where \mathcal{F} denotes the Fourier transform. If the excitation field is assumed to be a delta distribution in time, Veit *et al.* have shown in [26] that the Eq. (2.15) can be inverted due to causality to reconstruct the time-dependent dipole moment from the absorption spectrum

$$d(t) = \mathcal{F}^{-1} \{iA(\omega)\} = \frac{1}{2\pi} \int_{-\infty}^{\infty} iA(\omega) e^{i\omega t} d\omega, \quad \text{for } t > 0. \quad (2.16)$$

The approximation of delta-like excitation can be well justified in transient absorption spectroscopy, where the exciting attosecond XUV pulse is much shorter than any subsequent perturbation to the dipole moment realized by a strong NIR pulse.

2.1.2 Ultrashort pulses

For a dispersive medium with a frequency-dependent refractive index $n(\omega)$, it is convenient to describe light in the frequency domain, which is linked to the time domain by the Fourier transform

$$\tilde{E}(\omega) = \mathcal{F}\{E(t)\} = \int E(t) e^{-i\omega t} dt. \quad (2.17)$$

In an analogous manner, the time domain can be recovered by the inverse Fourier transform

$$E(t) = \mathcal{F}^{-1} \{\tilde{E}(\omega)\} = \frac{1}{2\pi} \int \tilde{E}(\omega) e^{+i\omega t} d\omega. \quad (2.18)$$

In this expression, the electric field can be considered as a wave packet that consists of an infinite sum of plane waves. The complex function $\tilde{E}(\omega)$ determines the spectral amplitude as well as the phase of the light pulse. For simpler notation, the z -dependence and vector identity of the field are omitted here and subsequently.

Figure 2.2 shows how a pulse builds up from a sum of plane waves. It is not only instructive to look at a discrete set of frequencies ω_j with $j = 1, 2, \dots, m$, but also very relevant, since most ultrashort light sources originate from mode-locked resonators with discrete longitudinal modes. The integral from Eq. (2.18) simplifies in this case to

$$E(t) = \frac{1}{2\pi} \sum_{j=1}^m \tilde{E}(\omega_j) e^{i\omega_j t}. \quad (2.19)$$

A few modes are enough, e.g. $m = 4$, to see the clear appearance of a pulse. In Fig. 2.2

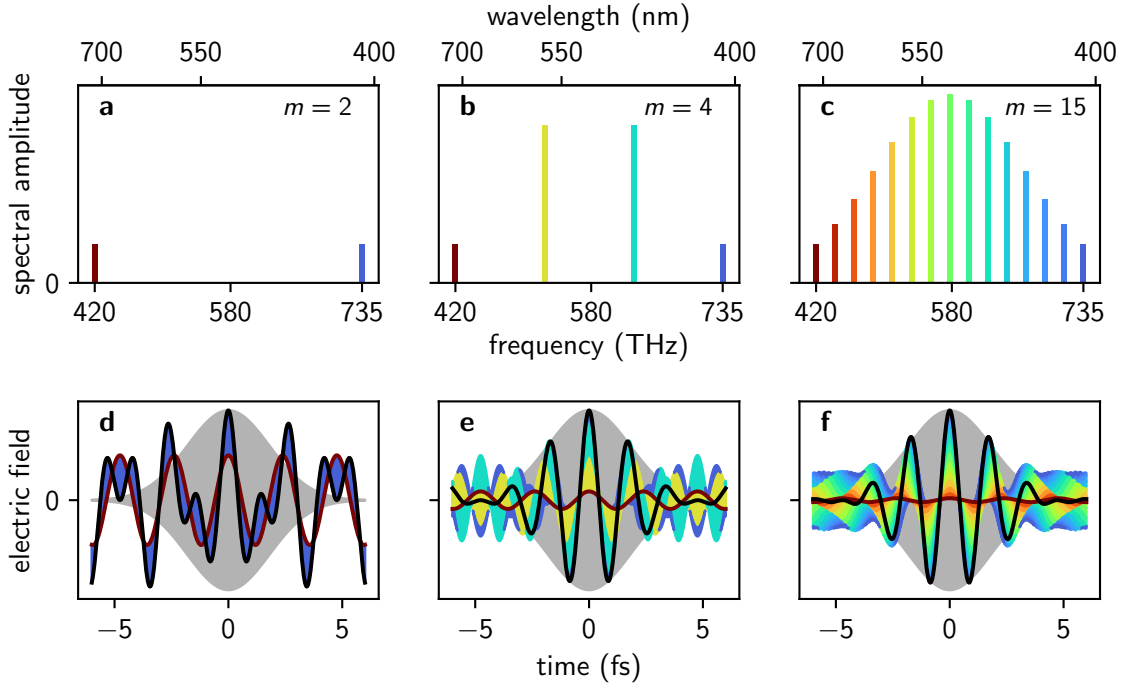


Figure 2.2: Buildup of a mode-locked laser pulse. **a-c** Spectral amplitudes of a discrete set of plane waves with a Gaussian envelope, illustrating various mode spacings. **d-f** The corresponding electric fields in the time domain. The contribution of each mode is indicated by its color. The black line is the total field, the sum of all modes. The shortest Gaussian pulse supported by the selected spectral bandwidth is shown as a gray-shaded envelope.

the gray-shaded area corresponds to the pulse envelope

$$A(t) = \frac{1}{2\pi} \int \tilde{A}(\Delta\omega) e^{i\Delta\omega t} d\Delta\omega \quad (2.20)$$

that is supported by the bandwidth of the spectrum. Here, the substitution $\omega = \omega_0 + \Delta\omega$ was used, which takes into account that the spectrum is finite in width and centered around the carrier frequency ω_0 . The frequency-shifted spectrum, also known as the spectral envelope, is defined as $\tilde{A}(\Delta\omega) \equiv \tilde{E}(\omega_0 + \Delta\omega)$. The electric field in the time domain can then be expressed by

$$E(t) = A(t) e^{i\omega_0 t}. \quad (2.21)$$

The length of a pulse τ_{FWHM} is commonly defined by the full width at half maximum (FWHM) of its intensity envelope $|A(t)|^2$. Analogously, the FWHM of the spectral intensity $|\tilde{A}(\Delta\omega)|^2$ is the bandwidth $\Delta\omega_{\text{FWHM}} = 2\pi\Delta\nu_{\text{FWHM}}$. Due to the properties of the Fourier transform, the broader the bandwidth of the laser, the shorter a pulse can become. This is commonly expressed in the time-bandwidth product (TBP)

$$\text{TBP} = \tau_{\text{FWHM}} \Delta\nu_{\text{FWHM}} \geq C_{\text{TL}}. \quad (2.22)$$

The constant C_{TL} is dependent on the pulse shape; for instance, in the case of a Gaussian

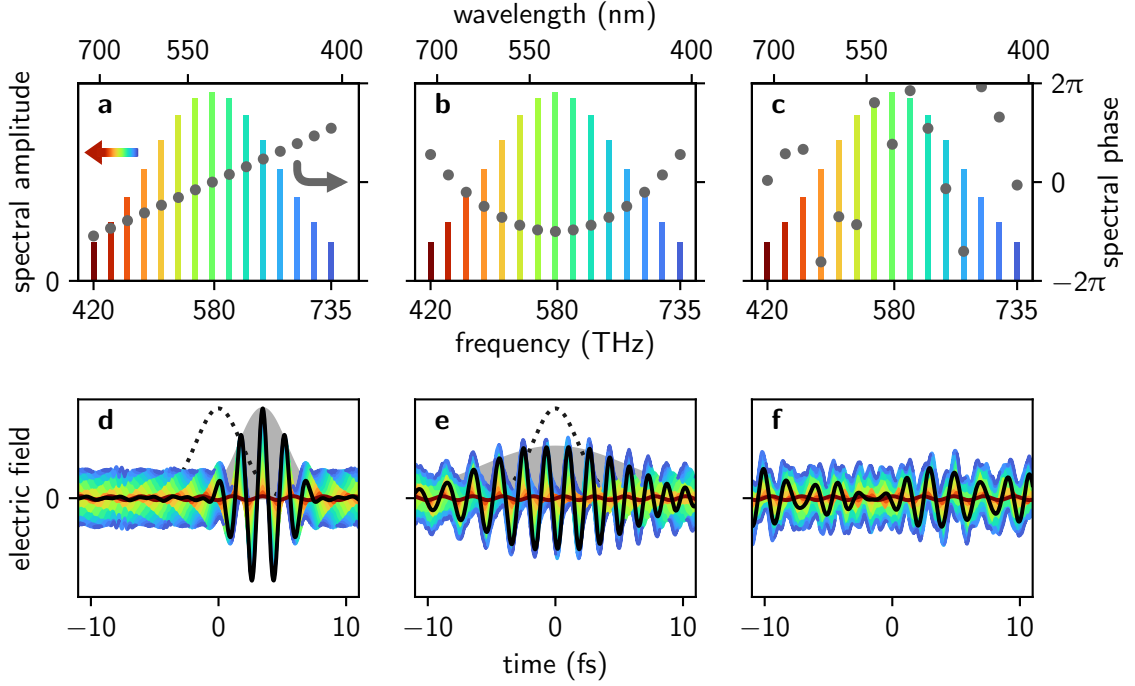


Figure 2.3: Influence of the spectral phase on an ultrashort pulse. Spectral amplitude and phase of a pulse with **a** linear phase ($\text{GD}=3.5 \text{ fs}$), **b** quadratic phase ($\text{GDD}=10 \text{ fs}^2$, $\text{CEP}=-\pi$), **c** random phase. **d-f** The corresponding electric fields in the time domain. The shaded areas indicate the current field envelope, the dotted line shows the field envelope of a pulse with constant phase as in Fig. 2.2 c. The pulse with $\tau_{\text{FWHM}}=3 \text{ fs}$ is shifted by 3.5 fs in **d** and broadened to 9.7 fs in **e**.

pulse $C_{\text{TL,Gauss}} = 0.441$. The pulse is said to be transform limited if the TBP is equal to the C_{TL} of the respective pulse shape. Achieving this shortest possible pulse is generally not an easy task, as it requires careful tuning of the spectral phase.

The spectral phase $\phi(\Delta\omega)$ of the spectral amplitude $\tilde{A}(\Delta\omega) = |\tilde{A}(\Delta\omega)|e^{i\phi(\Delta\omega)}$ is often expanded in a Taylor series at the carrier frequency

$$\phi(\Delta\omega) = \underbrace{\phi(0)}_{\text{CEP}} + \underbrace{\left. \frac{\partial\phi}{\partial\Delta\omega} \right|_0}_{\text{GD}} \Delta\omega + \frac{1}{2!} \underbrace{\left. \frac{\partial^2\phi}{\partial\Delta\omega^2} \right|_0}_{\text{GDD}} \Delta\omega^2 + \frac{1}{3!} \underbrace{\left. \frac{\partial^3\phi}{\partial\Delta\omega^3} \right|_0}_{\text{TOD}} \Delta\omega^3 + \dots \quad (2.23)$$

The first contribution, called the carrier-envelope phase (CEP), is the absolute spectral phase between the carrier and the envelope of the pulse. A nonzero value will lead to a shift between the maximum of the electric field and its envelope. The linear part of the expansion, the group delay (GD), shifts the full pulse in time, without altering its shape, illustrated in Fig. 2.3 **a** and **d**.

The quadratic coefficient is called group delay dispersion (GDD) or chirp. A positive value indicates that the pulse has traveled through a medium with normal dispersion and that the blue part of the spectrum is more delayed than the red part. Since a non-vanishing GDD means that the phase difference between spectral components is dependent on frequency, the pulse has to be longer than the transform limit, as shown in Fig. 2.3 **b** and **e**. This effect gets stronger for shorter pulses because they are supported by a larger

spectral bandwidth. For Gaussian pulses, the broadening is given by [63]

$$\tau_{\text{FWHM}}(\text{GDD}) = \tau_{\text{FWHM}}(0) \sqrt{1 + \left(\frac{4 \ln 2 \text{ GDD}}{\tau_{\text{FWHM}}^2(0)} \right)^2}. \quad (2.24)$$

To compress the pulses, the GDD can be adjusted with gratings [66], prisms [67], or chirped mirror pairs [68]. The third-order dispersion (TOD) leads to a more complex distortion of the pulse shape. Compensation of this third and even higher order dispersion terms is possible with more sophisticated setups, which is necessary when aiming for the shortest few-cycle pulses [69, 70]. In the case of a randomly fluctuating spectral phase, as in Fig. 2.3 **c**, the time-dependent field also fluctuates randomly and no pulse can build up.

Achieving a fixed phase relation between the different modes in an optical resonator is called mode-locking. For ultrashort pulses this is accomplished passively by self-amplitude modulation of the light in the resonator. Experimentally, there are several options to introduce losses that depend on the intensity of the light. In saturable absorbers, made of dyes or semiconductors, the short lifetime of the excited states is transferred to the temporal envelope of the pulse by modulating the resonator losses [71, 72]. This means that absorption is high for the low intensities of random mode phases, but when modes constructively interfere, a pulse builds up that saturates the absorber, allowing the pulse to be progressively amplified. In Kerr-lens mode-locking, the nonlinear Kerr effect causes the refractive index to change based on the intensity of light. This intensity-dependent alteration, driven by the medium's third-order susceptibility $\chi^{(3)}$, leads to intensity-dependent self-focusing. A well-placed aperture that transmits mainly the self-focused light strongly favors the shortest pulses [73]. An extensive discussion of mode-locking with these and other methods is given in [63].

2.1.3 Frequency combs

Laser oscillators are optical resonators, which typically support many longitudinal modes equidistantly separated by the free spectral range (FSR). It corresponds to the inverse time T_{rep} that light needs to propagate through the cavity, thus for a mode-locked pulsed laser the FSR is identical to the repetition rate f_{rep} . Since the mode-spacing is then given by f_{rep} , there is only one free parameter left to fully determine the frequency of all modes, namely the carrier envelope offset frequency f_{CEO} . This is the shift of the full spectrum away from zero, defined by $f_{\text{CEO}} = (f_n \bmod f_{\text{rep}})$ for any mode; thus $0 \leq f_{\text{CEO}} < f_{\text{rep}}$ holds. Given the mode number n , the absolute frequency of each mode can then be calculated by

$$f_n = f_{\text{CEO}} + n f_{\text{rep}}. \quad (2.25)$$

Since the spectrum is a sum of discrete equidistant modes, lasers that fulfill this condition are called frequency combs.

Figure 2.4 illustrates the influence of the frequencies f_{CEO} and f_{rep} on the spectrum and the temporal shape of the pulses. The repetition rates are chosen for clarity of the illustration, in most systems they are in the megahertz or gigahertz range. In the temporal domain, as shown in Fig. 2.4 **c-d**, the repetition rate changes the spacing between the pulses. The action of f_{CEO} is more subtle. It leads to a phase slip of ΔCEP from pulse

2 Theoretical background

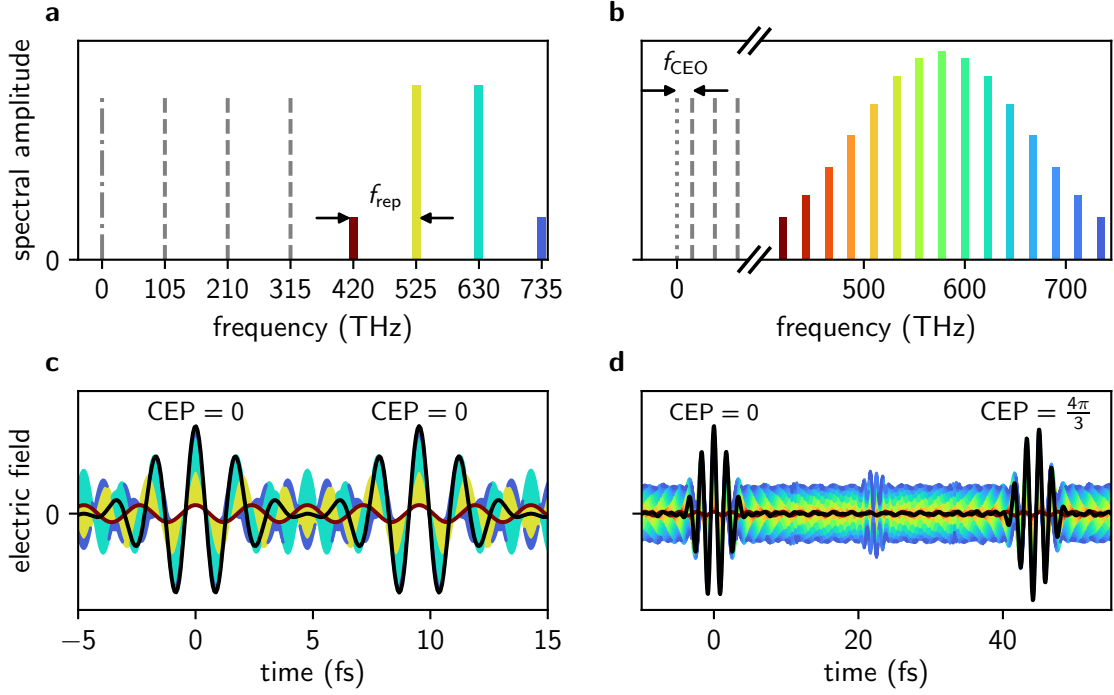


Figure 2.4: Frequency combs in the energy (a, b) and time domain (c, d). The left and right panels differ only in the parameters f_{CEO} and f_{rep} . For a and c: $f_{\text{CEO}} = 0$ THz, $f_{\text{rep}} = 105$ THz. For b and d: $f_{\text{CEO}} = 15$ THz, $f_{\text{rep}} = 22.5$ THz.

to pulse, defined by

$$f_{\text{CEO}} = \frac{1}{2\pi} f_{\text{rep}} \Delta\text{CEP}. \quad (2.26)$$

In summary, including the envelope \tilde{A} defined in Eq. (2.20), the full electric field for a frequency comb is given by [74]

$$\tilde{E}(\omega) = \tilde{A}(\omega - \omega_0) \sum_{n=0}^{\infty} \delta(\Delta\text{CEP} - \omega T_{\text{rep}} - 2\pi n) \quad (2.27)$$

$$E(t) = \sum_n A(t - nT_{\text{rep}}) e^{i(\omega_0 t + n(\Delta\text{CEP} - \omega_0 T_{\text{rep}}))}. \quad (2.28)$$

Whereas the repetition rate can straightforwardly be measured with a fast photodiode, the measurement and stabilization of f_{CEO} is challenging. In 1999 and 2000, this pivotal technology was developed [75–77], culminating in the awarding of half of the Nobel Prize in Physics in 2005 [78, 79]. The simplest scheme is self-referencing using a so-called f -to- $2f$ interferometer. Starting with an octave-spanning spectrum, which can be achieved by nonlinear optical fibers [80], the second harmonic is generated. In the spectral overlap, the second harmonic of a mode of the red part of the spectrum $2f_n$ and the fundamental blue mode f_{2n} lead to the heterodyne beating

$$2f_n - f_{2n} = 2(f_{\text{CEO}} + nf_{\text{rep}}) - (f_{\text{CEO}} + 2nf_{\text{rep}}) = f_{\text{CEO}}. \quad (2.29)$$

With these techniques, frequency combs established as rulers for precision spectroscopy in the optical regime. The absolute frequency of any continuous wave (CW) laser can be determined by measuring the beat against a frequency comb, the repetition rate, f_{CEO} , and the mode number n . The frequency comb links optical frequencies to the radio regime, where established electronic devices are fast enough to count oscillations.

Over the past two decades, the applications of frequency combs have expanded significantly. These combs are now integral to a variety of spectroscopic techniques that span a broad spectral range, from the mid-infrared to the XUV [81–84]. The advent of dual-comb spectroscopy [85] has further broadened the scope of applications, making it particularly relevant for fields such as biology and chemistry. Beyond spectroscopy, frequency combs are also utilized in areas like distance measurement and laser ranging [86]. Ongoing advancements, including cost reduction and miniaturization [87], promise to unlock even more applications and expand the usage.

2.2 Optical cavities

If 10% of the light from a monochromatic laser passes through a mirror, what happens when a second identical mirror is placed behind the first?

Surprisingly, the total transmission can vary dramatically, ranging from less than 1% to 100%, depending on the exact distance between these two mirrors. This counterintuitive result not only astonishes many students, but also offers a glimpse into the fascinating world of optical cavities. The following section introduces the fundamental concepts of these resonators. More detailed discussions can be found in [49, 88–90].

2.2.1 Longitudinal modes

The most basic resonator is a so-called Fabry-Perot cavity consisting of two parallel flat mirrors facing each other. Here, we consider the slightly more general case of a ring cavity with one input coupler with field reflectivity r_{ic} and n additional mirrors with a combined field reflectivity given by $r_{\text{cav}} = \prod_{i=1}^n r_i$. The respective intensity reflectivities are denoted as $R_{\{\text{ic},\text{cav}\}} = r_{\{\text{ic},\text{cav}\}}^2$. All mirrors are assumed to be ideal with no scattering losses or absorption, so the intensity transmittance of each mirror is $T = 1 - R$, and the respective field transmittances satisfy $t^2 = T$. For an even number of mirrors, the phase acquired during one round trip in vacuum is equal to

$$\phi = kd = \frac{\omega}{c}d, \quad (2.30)$$

where d is the total round trip length. From the condition for constructive interference $\phi = 2\pi n$ for $n \in \mathbb{Z}$, the free spectral range (FSR) between neighboring longitudinal resonator modes follows as

$$\Delta\omega_{\text{FSR}} = 2\pi \frac{c}{d}. \quad (2.31)$$

For a Fabry-Perot resonator, the round trip length is twice the distance between the two mirrors $d = 2L$.

To derive the generic expression of the full circulating field E_{circ} inside a cavity, the following logic can be applied: E_{circ} reaches a steady state when the incoming field after the input coupler $E_0 t_{\text{ic}}$ balances the losses and phase shifts of the circulating field in one

2 Theoretical background

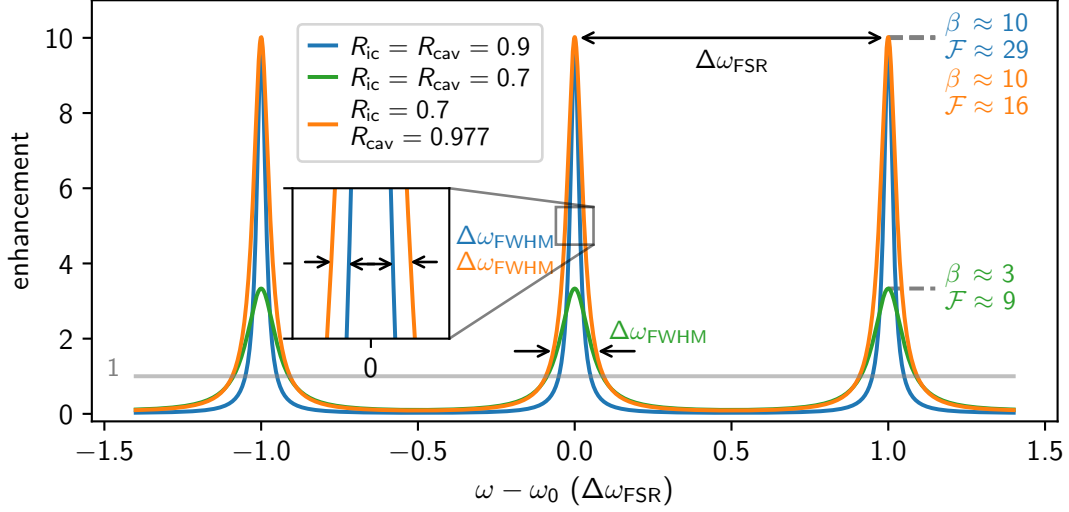


Figure 2.5: Airy distribution of the cavity enhancement for different mirror parameters. The blue and green lines indicate impedance-matched cavities, while the orange line represents a cavity in the over-coupled regime. The inset shows a comparison of the FWHM of the impedance-matched and the over-coupled cavity with the same enhancement. Note that overall higher mirror reflectivity results in higher but narrower cavity resonances, and that the over-coupled cavity can achieve the same enhancement with approximately half the finesse, corresponding to broader resonances.

round trip

$$E_{\text{circ}}(\phi) = E_0 t_{\text{ic}} + r_{\text{ic}} r_{\text{cav}} e^{-i\phi} E_{\text{circ}} \quad (2.32)$$

$$\implies E_{\text{circ}}(\phi) = \frac{E_0 t_{\text{ic}}}{1 - r_{\text{ic}} r_{\text{cav}} e^{-i\phi}}. \quad (2.33)$$

This results in the following expression for the circulating intensity

$$I_{\text{circ}}(\phi) = \frac{I_0 T_{\text{ic}}}{|1 - r_{\text{ic}} r_{\text{cav}} e^{-i\phi}|^2} \quad (2.34)$$

$$= \frac{I_0 T_{\text{ic}}}{(1 - \sqrt{R_{\text{ic}} R_{\text{cav}}})^2 + 4\sqrt{R_{\text{ic}} R_{\text{cav}}} \sin^2(\phi/2)}. \quad (2.35)$$

The enhancement

$$\beta(\phi) = I_{\text{circ}}(\phi)/I_0 \quad (2.36)$$

forms a so-called Airy distribution, as illustrated in Fig. 2.5. It resembles a sum of equally spaced Lorentzians [90]. In analogy to the natural lifetime of atomic transitions, the FWHM of the Lorentzians $\Delta\omega_{\text{Lorentzian}}$ is the inverse of the photon-decay time

$$\tau = \frac{2\pi}{-\log(R_{\text{ic}} R_{\text{cav}}) \Delta\omega_{\text{FSR}}}. \quad (2.37)$$

With the circulating intensity from Eq. (2.35), the transmitted light for each mirror is simply given by $I_{\text{trans},i} = T_i I_{\text{circ}}$. For the total reflected light at the input coupler, the interference between the reflected incoming beam and the light leaking out of the cavity results in

$$I_{\text{refl}}(\phi) = I_0 \frac{(\sqrt{R_{\text{ic}}} - \sqrt{R_{\text{cav}}})^2 + 4\sqrt{R_{\text{ic}}R_{\text{cav}}}\sin^2(\phi/2)}{(1 - \sqrt{R_{\text{ic}}R_{\text{cav}}})^2 + 4\sqrt{R_{\text{ic}}R_{\text{cav}}}\sin^2(\phi/2)} \quad (2.38)$$

$$= I_0 - \sum_{i=1}^n I_{\text{trans},i}. \quad (2.39)$$

Using the small-angle approximation $\sin(\phi) \approx \phi$, the finesse \mathcal{F} , which expresses the ratio between the FSR and the FWHM of the airy peaks, evaluates to

$$\mathcal{F} \equiv \frac{\Delta\omega_{\text{FSR}}}{\Delta\omega_{\text{FWHM}}} \approx \frac{\pi\sqrt{r_{\text{ic}}r_{\text{cav}}}}{1 - r_{\text{ic}}r_{\text{cav}}} \overset{T_{\{\text{ic},\text{cav}\}} \ll 1}{\approx} \frac{2\pi}{T_{\text{ic}} + T_{\text{cav}}}. \quad (2.40)$$

The enhancement at resonance $\beta = \beta(0)$ can be expressed as

$$\beta \approx \frac{T_{\text{ic}}\mathcal{F}^2}{\pi^2}, \quad (2.41)$$

using the approximation of small transmittances for all mirrors.

If $T \equiv T_{\text{ic}} = T_{\text{cav}}$, the cavity is impedance matched. According to Eq. (2.38) no light is reflected on resonance due to complete destructive interference and the enhancement for high reflectivities is given by $\beta = 1/T = \mathcal{F}/\pi$. For enhancement cavities with minimized phase noise, it makes sense to work in the over-coupled regime with $T_{\text{ic}} \gg T_{\text{cav}}$ [91]. This reduces the finesse but doubles the enhancement relative to it, since Eqs. (2.40) and (2.41) evaluate to $\beta = 4/T_{\text{ic}} = 2\mathcal{F}/\pi$.

Additional losses in the cavity can be accounted for by introducing the round-trip loss \mathcal{L} . By replacing the combined cavity reflectivity with

$$R'_{\text{cav}} = (1 - \mathcal{L})R_{\text{cav}}, \quad (2.42)$$

and the transmission with $T'_{\text{cav}} = 1 - R'_{\text{cav}}$, the above expressions describe a lossy cavity. Since in such a system not all of the power is transmitted or reflected, Eq. (2.39) needs an additional loss term, resulting in $I_{\text{refl}}(\phi) = I_0 - \sum_{i=1}^n I_{\text{trans},i} - \mathcal{L}I_{\text{circ}}$.

Another important aspect of a cavity is, that incoming light can only be resonantly enhanced if it spatially overlaps with the transverse cavity mode. Any mismatch of the incoming light and the cavity mode leads to a reduction of the mode matching factor $0 \leq \epsilon_{\text{mm}} \leq 1$. This decreases the circulating power to $I'_{\text{circ}} = \epsilon_{\text{mm}}I_{\text{circ}}$ and increases the reflected light to $I'_{\text{refl}} = \epsilon_{\text{mm}}I_{\text{refl}} + (1 - \epsilon_{\text{mm}})I_0$. Subsection 2.2.3 describes the spatial form of the most common transverse modes in cavities.

2.2.2 Femtosecond enhancement cavities

In contrast to resonators that enhance a continuous wave laser with a single frequency ω , enhancement cavities for ultrashort pulses need to be resonant with many modes ω_j simultaneously. The round-trip phase in the cavity generally depends on the frequency due to the mirror dispersion or the cavity medium, requiring the addition of a dispersion

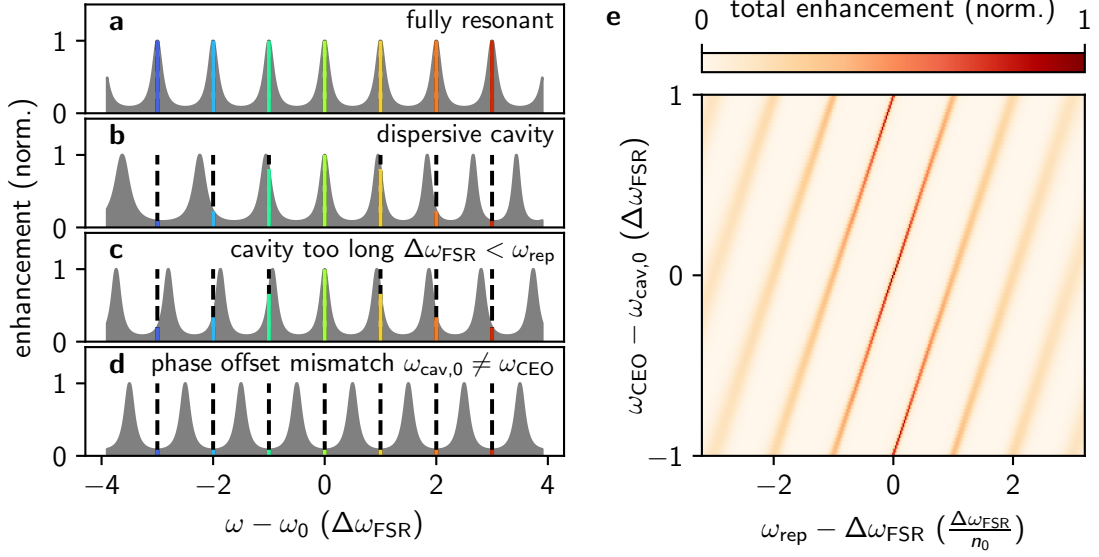


Figure 2.6: **a-d** Transmission function of a cavity with finesse $\mathcal{F} = 5$ in shaded gray with frequency comb modes as vertical lines for different scenarios. The colored fraction of the lines corresponds to the strength of the enhancement. **a** All modes are resonant. **b** Cavity dispersion causes unevenly spaced enhancement peaks. **c** The cavity is longer than the distance between two pulses, resulting in reduced temporal overlap and a different spacing of comb and cavity modes in the frequency domain. **d** The enhancement peaks are linearly shifted away from the modes due to a different phase offset. **e** The total enhancement for a Gaussian spectrum with FWHM bandwidth of 10% in a cavity with $\mathcal{F} = 30$ depends on the mismatch of repetition rate and offset frequency, calculated with Eq. (2.47). The center frequency is $\omega_0 = n_0 \Delta\omega_{\text{FSR}}$.

term $\phi_d(\omega)$ to Eq. (2.30). This modifies the resonance condition to

$$2\pi n = \frac{\omega}{c}d + \phi_d(\omega) \quad n \in \mathbb{Z}. \quad (2.43)$$

The frequency difference between two adjacent resonances ω_n can be expressed with the definition of Eq. (2.31) as

$$\frac{\omega_{n+1} - \omega_n}{\Delta\omega_{\text{FSR}}} = 1 - \frac{\phi_d(\omega_{n+1}) - \phi_d(\omega_n)}{2\pi}. \quad (2.44)$$

While a linear phase ϕ_d corresponds to a group delay and effectively alters the FSR, any nonlinear contribution leads to a frequency-dependent spacing of the resonances. Since the spectrum of a frequency comb, given by Eq. (2.25), consists of equidistant modes separated by $\omega_{\text{rep}} = 2\pi f_{\text{rep}}$, a dispersive cavity cannot enhance all laser modes simultaneously. This results in reduced enhancement and a narrower intra-cavity spectrum, as shown in Fig. 2.6 **a-b**.

For a constant, frequency-independent phase $\phi_{d,0}$ accumulated in a dispersion-free cavity, the resonances are equidistantly spaced. They can be derived from Eq. (2.43) as

$$\omega_n = n\Delta\omega_{\text{FSR}} - \frac{\phi_{d,0}}{2\pi}\Delta\omega_{\text{FSR}} = n\Delta\omega_{\text{FSR}} + \omega_{\text{cav},0}, \quad (2.45)$$

with the definition of the cavity offset frequency $\omega_{\text{cav},0} \equiv -\phi_{d,0}\Delta\omega_{\text{FSR}}/(2\pi)$. By direct comparison with the formula for the frequency comb modes Eq. (2.25), the two resonance conditions that must be satisfied for optimal enhancement are given by

$$\Delta\omega_{\text{FSR}} = \omega_{\text{rep}}, \quad \omega_{\text{cav},0} = \omega_{\text{CEO}}. \quad (2.46)$$

For any mismatch, not all modes can be resonantly enhanced as depicted in Fig. 2.6 **c-d**, resulting in a reduced total enhancement as shown in Fig. 2.6 **e**. This total enhancement for the full spectrum of a frequency comb with envelope $A(\omega)$ can be calculated by summing over all individual modes as

$$\beta_{\text{total}} = \sum_n A(n\omega_{\text{rep}} + \omega_{\text{CEO}})\beta(\phi) \quad (2.47)$$

$$\phi = 2\pi \left(n + \frac{n(\omega_{\text{rep}} - \Delta\omega_{\text{FSR}})}{\Delta\omega_{\text{FSR}}} + \frac{\omega_{\text{CEO}} - \omega_{\text{cav},0}}{\Delta\omega_{\text{FSR}}} \right). \quad (2.48)$$

To conclude, this section has shown that a femtosecond enhancement cavity must be free of dispersion for optimal enhancement. Since mirror coatings can only fulfill this condition over a limited spectral width this becomes the primary technical limitation for intra-cavity ultrashort pulses shorter than 50 fs [92], aside from the mirror damage threshold. In a dispersion-free cavity, the supported modes have the same structure as a frequency comb. For perfect enhancement, Eq. (2.46) must be satisfied. In the time domain, this means that the round-trip time must be equal to the time between two laser pulses, and the intra-cavity accumulated phase must cancel the CEP. Satisfying the first condition is more crucial because, even with a completely mismatched ω_{CEO} , a resonance with reduced enhancement can be achieved by tuning $\Delta\omega_{\text{FSR}}$ or ω_{rep} , which is not possible in reverse.

2.2.3 Transverse modes

In the previous sections, only the simplest solutions of the Helmholtz Eq. (2.5) were considered: plane waves. Due to their infinite transverse extent, they are not well suited to describe the propagation of laser beams. To overcome this limitation, the paraxial approximation is applied, where the light amplitude changes slowly in the propagation direction ($\partial/\partial z$) $A \ll kA$, leading to the paraxial Helmholtz equation. A well-known solution is the Gaussian beam, whose electric field is in cylindrical coordinates ($\rho^2 = x^2 + y^2$) given by:

$$E(\rho, z) = A_0 \frac{w_0}{w(z)} \exp\left(-\frac{\rho^2}{w(z)^2}\right) \exp\left(-i \left[kz + \frac{k\rho^2}{2R(z)} - \zeta(z) \right]\right). \quad (2.49)$$

The following quantities, illustrated in Fig. 2.7 **a** have been used in this expression.

- $w(z)$: The radius at which the intensity compared to the beam center ($\rho = 0$) has

2 Theoretical background

fallen to $1/e^2$. It evolves with

$$w(z) = w_0 \sqrt{1 + \left(\frac{z}{z_R}\right)^2}. \quad (2.50)$$

- w_0 : The waist radius at the focus $w(z = 0)$.
- z_R : The Rayleigh length is the distance at which the intensity on the propagation axis is half of the value it has at the focus. In a medium with refractive index n , it is given by

$$z_R = \frac{\pi w_0^2 n}{\lambda}. \quad (2.51)$$

- $R(z)$: The radius of the wavefront curvature which evolves as

$$R(z) = z \left[1 + \left(\frac{z_R}{z}\right)^2 \right]. \quad (2.52)$$

- $\zeta(z)$: The Gouy phase, which the beam acquires during propagation through the focus. It is given by

$$\zeta(z) = \arctan \frac{z}{z_R}. \quad (2.53)$$

Other properties, such as the far-field divergence $\theta = w_0/z_R$, can be derived from these definitions. For a given wavelength, specifying the position of the waist and w_0 is sufficient

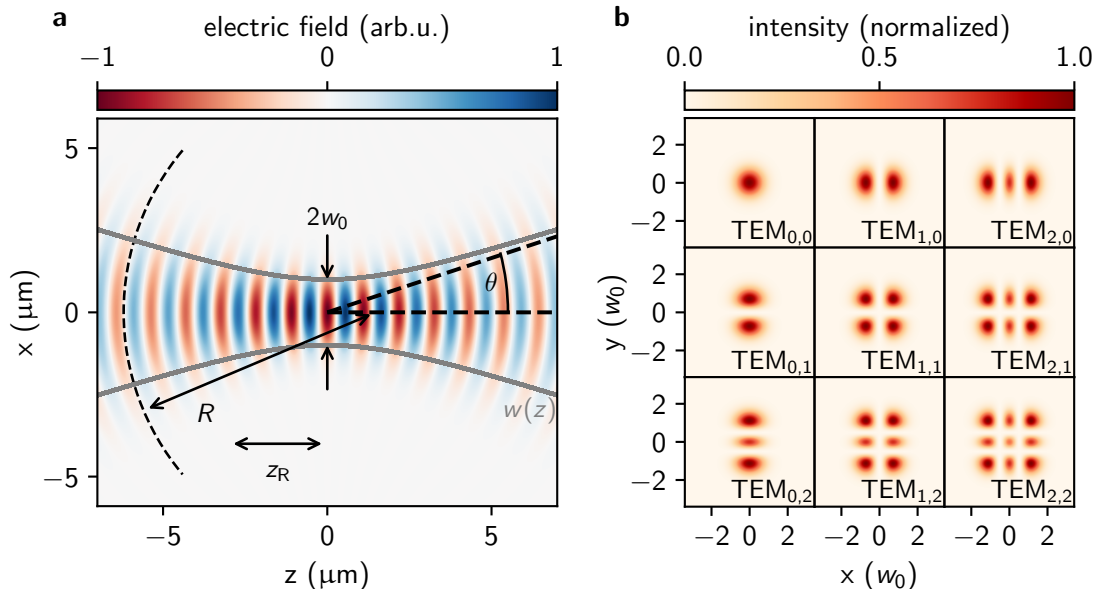


Figure 2.7: **a** Illustration of a Gaussian beam with $\lambda = 1039$ nm and waist radius $w_0 = 1$ μm . Rayleigh length z_R , beam radius $w(z)$, wavefront curvature R and beam divergence θ are marked. **b** Intensity profiles of the lowest-order Hermite-Gaussian TEM_{mn} modes.

to fully describe a beam. Along the propagation of the beam, the intensity profile follows a Lorentzian distribution, while transversely it has a Gaussian envelope, justifying its name.

The paraxial Helmholtz equation has also higher order solutions, which are in Cartesian coordinates known as Hermite-Gaussian modes. The first orders of these modes are depicted in Fig. 2.7 b. A derivation can for example be found in [89]. The order of the modes are represented by the natural numbers m and n . The fundamental Gaussian beam is modulated with the respective Hermite polynomial $H_{m,n}$ and the Gouy phase is multiplied accordingly. The expression for the electric field is obtained by replacing A_0 from Eq. (2.49) with the following spatially dependent amplitudes

$$A_{mn} = H_m \left(\frac{\sqrt{2}x}{w(z)} \right) H_n \left(\frac{\sqrt{2}y}{w(z)} \right) e^{-i(m+n)\zeta(z)}. \quad (2.54)$$

Since $H_0 = 1$, the fundamental of these transverse electromagnetic modes (TEM_{00}) is equal to the Gaussian mode.

2.3 Strong-field light-matter interaction

This thesis examines the interaction of light with matter in the regime of strong fields and high intensities. In this scenario, the response of matter to light, specifically the polarization, becomes highly nonlinear with respect to the incident field. The intensities can even reach a regime where the Taylor expansion of the polarization described in Eq. (2.2) becomes unsuitable due to the dominance of quantum effects such as tunneling.

This section introduces the time-dependent Schrödinger equation (TDSE), which best describes the response of atoms to intense light, and then discusses ionization and photoemission from metallic tips in strong fields, as well as matter wave diffraction by the Kapitza-Dirac effect.

2.3.1 Schrödinger equation

The non-relativistic evolution of a state $|\psi\rangle$ in a system with Hamiltonian $\hat{H}(t)$ follows the TDSE

$$i\hbar \frac{d}{dt} |\psi\rangle = \hat{H}(t) |\psi\rangle. \quad (2.55)$$

For an electron in a potential $V(\mathbf{r})$ under the influence of a time-varying electric field, the Hamiltonian in dipole approximation equals [93]

$$\hat{H}(t) = \frac{\hat{\mathbf{p}}^2}{2m_e} + e\mathbf{E}(t) \cdot \hat{\mathbf{r}} + V(\hat{\mathbf{r}}). \quad (2.56)$$

The dipole approximation assumes that the field is constant within the system, which is well justified since the optical wavelengths considered are much larger than the atomic size. In this approximation, any magnetic contributions are neglected. The Hamiltonian is expressed in the length gauge, but it is also common to use the velocity gauge, which is analytically equivalent but may yield different numerical results [94, 95].

Unfortunately, the TDSE with this Hamiltonian has exact analytic solutions only for certain special cases. For more general problems, there are analytic approaches for specific

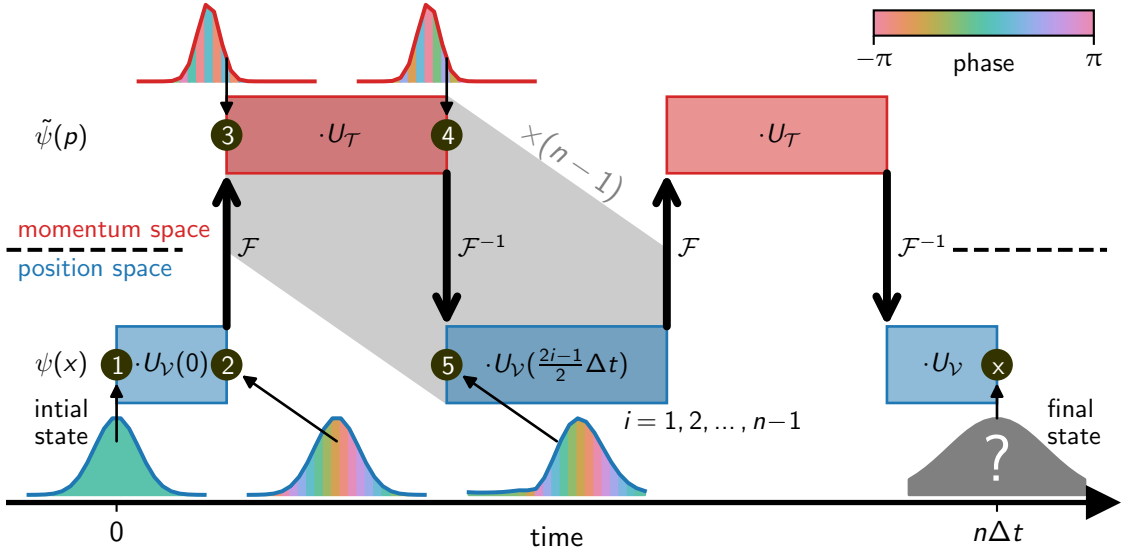


Figure 2.8: Numerical solution of the TDSE with the split-operator method. The initial wave function is propagated alternately in position and momentum space using the Fourier transform \mathcal{F} . The blue and red boxes illustrate the multiplication with arrays of complex numbers given by the operators $U_V(t, x)$ and $U_T(p)$. The steps covered by the gray area are repeated $n-1$ times. See the text for more details. The plotted envelopes of the exemplary wave functions for the first steps (1-5) represent their absolute values, with color indicating their phase.

approximations, such as the stationary phase or semiclassical approximation, as well as various numerical methods [96]. Since it has been used in Publication 3.1, the numerical split-operator method is briefly introduced here.

Solving the TDSE numerically with the split-operator method

The split-operator method is discussed here for an atom in single-active electron approximation in one dimension. The atomic Coulomb potential is modified with the soft-core parameter a to $V(x) = e(x^2 + a)^{-\frac{1}{2}}$ in order to avoid the numeric divergence at $x = 0$ [97]. The full Hamiltonian with these approximations can be separated into a part that only depends on momentum $\mathcal{T}(p)$ and a general potential term $\mathcal{V}(x, t)$, which is a function of position and time

$$H(x, p, t) = \underbrace{\frac{p^2}{2m_e}}_{\mathcal{T}(p)} + \underbrace{\frac{e}{\sqrt{x^2 + a}} + eE(t)x}_{\mathcal{V}(x, t)}. \quad (2.57)$$

Using the Zassenhaus formula [98], which gives an approximation for $\exp(x + y)$, the propagation operator $U_H(x, p, t, \Delta t)$ for a small time step Δt can be approximated by

$$\underbrace{\exp\left(-i\frac{H\Delta t}{\hbar}\right)}_{U_H(x,p,t,\Delta t)} = \underbrace{\exp\left(-i\frac{\mathcal{V}(x,t)\Delta t}{2\hbar}\right)}_{U_V(x,t,\Delta t/2)} \underbrace{\exp\left(-i\frac{\mathcal{T}(p)\Delta t}{\hbar}\right)}_{U_T(p,\Delta t)} \underbrace{\exp\left(-i\frac{\mathcal{V}(x,t)\Delta t}{2\hbar}\right)}_{U_V(x,t,\Delta t/2)} + O(\Delta t^3). \quad (2.58)$$

The propagation of a wave function in position space $\psi(x, t)$ with the operator $U_V(x, t, \Delta t/2)$ is numerically only the multiplication with a complex number

$$\psi\left(x, t + \frac{\Delta t}{2}\right) = U_V\left(x, t, \frac{\Delta t}{2}\right) \psi(x, t). \quad (2.59)$$

The same is true for a propagation in momentum space

$$\tilde{\psi}(p, t + \Delta t) = U_T(p, \Delta t) \tilde{\psi}(p, t). \quad (2.60)$$

Since momentum and position space are connected by the Fourier transform, the total propagation for one time step Δt can be expressed as

$$\psi(x, t + \Delta t) = U_V\left(x, t + \frac{\Delta t}{2}, \frac{\Delta t}{2}\right) \mathcal{F}^{-1}\left[U_T(p, \Delta t) \mathcal{F}\left\{U_V\left(x, t, \frac{\Delta t}{2}\right) \psi(x, t)\right\}\right]. \quad (2.61)$$

Figure 2.8 shows that the TDSE can therefore be solved step by step alternating in position and momentum space, which can be achieved numerically by fast Fourier transforms (FFTs) and multiplications of complex numbers. A suitable initial wave function can for example be condensed by propagating a random wave function in imaginary time $i|\Delta t|$ [99].

Volkov wave packet and the ponderomotive energy

One of the few examples that have an exact analytical solution is the propagation of a Gaussian wave packet [100] without external potential $V(x) = 0$ in a CW laser field $E(t) = E_0 \cos(\omega t)$. The one-dimensional solution assuming an initial Gaussian width of σ_0 is given by [96]

$$\psi(x, t) = \left(\frac{\sigma_0}{\sqrt{\pi}\sigma^2(t)}\right)^{1/2} \exp\left\{\frac{i}{\hbar}\left[\frac{U_p}{2\omega}\sin(2\omega t) - U_p t + xp(t)\right]\right\} \exp\left\{-\frac{(x - q(t))^2}{2\sigma^2(t)}\right\}, \quad (2.62)$$

$$\sigma^2(t) = \sigma_0^2 + i\frac{\hbar t}{m_e}, \quad (2.63)$$

with the solutions of the classical equations of motion for the initial momentum p_0 and initial position q_0

$$p(t) = p_0 - \frac{eE_0}{\omega} \sin(\omega t), \quad (2.64)$$

$$q(t) = q_0 + \frac{p_0 t}{m_e} + \frac{eE_0}{m_e \omega^2} [\cos(\omega t) - 1]. \quad (2.65)$$

Additionally, the ponderomotive energy U_p has been defined as the average kinetic energy of an oscillating electron over one period

$$U_p \equiv \frac{1}{T} \int_0^T \frac{p^2}{2m_e} dt = \frac{e^2 E_0^2}{4m_e \omega^2}. \quad (2.66)$$

The wave packet of Eq. (2.62) is constructed from Volkov states [101], which are plane electron waves. The resemblance of the wave packet evolution to classical mechanics is immediately apparent. This strongly supports the use of classical electron trajectories as a valuable tool for describing electron dynamics in the strong-field approximation (SFA), which neglects the atomic potential for continuum states.

The ponderomotive energy is an important scale for the strong-field interaction of ultrashort laser pulses with atoms. By evaluating all constants, the proportionality to the intensity $I = c\epsilon_0 E^2/2$ of a laser can be expressed in convenient units as

$$U_p \approx 9.33 \text{ eV} \frac{I}{10^{14} \text{ W/cm}^2} \frac{\lambda^2}{\mu\text{m}^2}. \quad (2.67)$$

2.3.2 Ionization in intense laser fields

Shortly after the invention of the laser in the 1960s, Keldysh developed a theory for the photoionization of a hydrogen-like atom with an ionization potential I_p much higher than the photon energy [7]. He calculated in first-order perturbation theory the transition amplitude from the unperturbed ground state to a Volkov state in the SFA. Modern reviews with generalizations can be found e.g. in [102, 103]. As a first result, the probability density per unit time of a multiphoton transition to a continuum state with momentum p is proportional to delta functions to satisfy energy conservation

$$\frac{dw}{dpdt} \propto \sum_{n \geq n_{\min}} \delta \left(\underbrace{\frac{p^2}{2m_e}}_{E_e} + U_p + I_p - n\hbar\omega \right), \quad (2.68)$$

where n denotes the photon number. For the minimum photon number n_{\min} , the energy is sufficient to overcome the ionization potential and the ponderomotive barrier

$$0 < n_{\min} \hbar\omega - U_p + I_p \leq \hbar\omega. \quad (2.69)$$

Above-threshold ionization

Ionization in strong fields is typically observed for several photon numbers at the same time, resulting in the photoelectron spectra of above-threshold ionization (ATI) [4, 104, 105]. The photoelectron spectra consist of several peaks separated by $\hbar\omega$, as schematically illustrated in Fig. 2.9 a. Since U_p is proportional to the intensity, the peaks of the electron energy E_e also shift linearly with the intensity [6]. In the limit of long pulses, this shift cannot be observed because the ponderomotive potential lasts long enough to accelerate the electrons out of the focus [5, 106, 107]. When the ponderomotive potential becomes large enough to require an additional photon for ionization, i.e. at $E_e = 0$, a channel closing (CC) occurs [108, 109].

One of the shortcomings of the SFA is that it neglects any intermediate atomic states. However, Freeman *et al.* [110] have discovered that these (Freeman) resonances play an im-

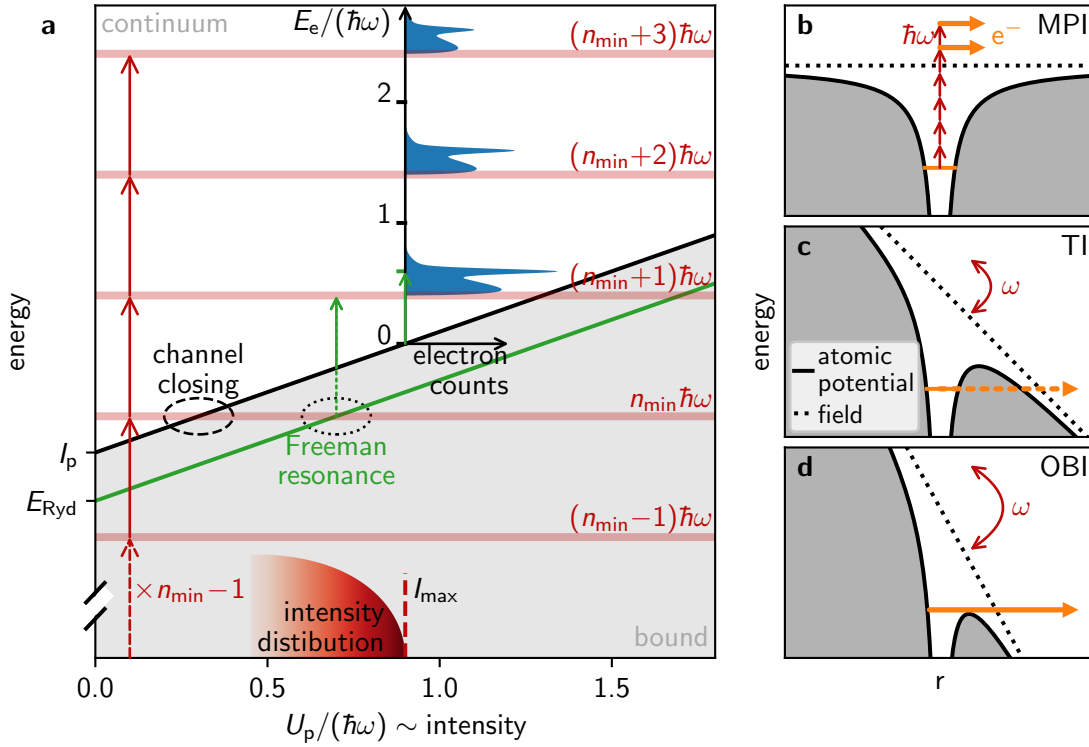


Figure 2.9: Strong-field ionization. **a** The ionization threshold (black line) and a Rydberg state (green line) shift with increasing ponderomotive potential. The red lines indicate the energies accessible for MPI with n photons. When $n\hbar\omega$ matches the ionization threshold, this ionization channel closes (CC, shown as a dashed ellipse), whereas a coincident Rydberg state results in a Freeman resonance (dotted ellipse). The red shaded area illustrates an exemplary intensity distribution formed by focal volume averaging of a Gaussian beam with maximum intensity I_{\max} . The resulting ATI electron spectrum is shown in blue, with the sharp features within the spectrum arising from the resonance. **b-d** Dominant ionization mechanisms for increasing intensity: multiphoton ionization (MPI), tunnel ionization (TI) and over-the-barrier ionization (OBI).

portant role in ATI, followed by observations in many atomic systems [111–114]. Freeman resonances originate from intermediate states that are shifted by the AC Stark effect into resonance with an integer number of photons for certain intensities, as shown in Fig. 2.9 **a**. For Rydberg states, the AC Stark shift can be approximated by the ponderomotive potential, while the ground state shift is often neglected [115]. Due to the enhanced ionization yield, the Freeman resonances can dominate the electron spectrum.

Ionization rates in different intensity regimes

The Keldysh theory allows not only to predict the qualitative observations of ATI (except for Freeman resonances), but also to calculate the ionization rate. For small continuum momenta $p \approx 0$, the intensity dependence of the ionization rate can be expressed in the

general Keldysh formula [7, 103]

$$\frac{dw}{dt} \propto \exp \left\{ -2 \frac{I_p + U_p}{\hbar\omega} \times \left[\operatorname{arcsinh} \gamma - \frac{\gamma \sqrt{1 + \gamma^2}}{1 + 2\gamma^2} \right] \right\}, \quad (2.70)$$

with the dimensionless Keldysh parameter defined as

$$\gamma = \sqrt{\frac{I_p}{2U_p}}. \quad (2.71)$$

It can also be thought of as the ratio of the tunneling time required for the electron to leave the atomic potential to the period of an optical cycle. The Keldysh parameter is often used to distinguish between the regime of multiphoton ionization (MPI) ($\gamma \gg 1$) and the regime of tunnel ionization (TI) ($\gamma \ll 1$), shown in Fig. 2.9 **b** and **c**. In these limits, the ionization rate can be expressed as

$$\text{MPI, } \gamma \gg 1: \quad \frac{dw}{dt} \propto \left(\frac{1}{2\gamma^2} \right)^{n_{\min}} \propto I^{n_{\min}} \quad (2.72)$$

$$\text{TI, } \gamma \ll 1: \quad \frac{dw}{dt} \propto \exp \left\{ -\frac{4}{3} \frac{\sqrt{2m_e} I_p^{3/2}}{\hbar e E_0} \right\}. \quad (2.73)$$

While in MPI, ionization is considered a nonlinear process in the photon picture, this perturbation approach breaks down in TI. Light is treated as a classical field, bending the binding potential until tunneling is likely. This has important consequences. Due to the high nonlinearity of the field, tunneling is limited to a fraction of an optical cycle, when the field amplitude is at its highest. This confinement on a sub-cycle level opens the door to attosecond physics, including the famous high-harmonic generation (HHG) of XUV pulses [14, 116, 117].

For completeness, the regime of over-the-barrier ionization (OBI) should also be mentioned, as illustrated in Fig. 2.9 **d**. In this regime, the field is so strong that the potential barrier disappears entirely, resulting in ionization even from a classical perspective. However, OBI of ground state noble gas atoms requires intensities $\gtrsim 10^{14} \text{ W/cm}^2$ [118], exceeding those discussed in this thesis.

Generalizations of Keldysh theory

One of the most common generalizations of Keldysh's theory was developed by Perelomov, Popov and Terent'ev [119], referred to as the PPT model. It calculates the three-dimensional photoionization rate for the ground state of hydrogen-like atoms with orbital angular momentum l and magnetic quantum number m , incorporating the Coulomb interaction as a first-order correction to the quasiclassical action. In the ADK theory [120], named after the authors Ammosov, Delone and Krainov, the PPT model is extended to arbitrary atoms and ions in the tunneling regime ($\gamma < 0.5$) [121]. For example, see Chang [122] for a review of the analytical expressions of these two models. Similarly, the strong-field photoionization in the velocity gauge is considered in Reiss [123] and is also extended to the relativistic case [124].

To conclude this section, numerous experiments have investigated photoionization in strong fields across various atomic systems and intensity regimes. Keldysh theory has

been extremely successful in explaining most findings and has served as the foundation for further, more refined theories.

2.3.3 Photoemission from metals

Transitioning from photoionization in atomic systems to photoemission in solid-state systems introduces several changes. Instead of discrete energy levels, electronic states are described in terms of bands, and the energy required to free an electron is determined by the work function W , rather than the ionization potential. In addition to these fundamental differences, there are several other factors to consider.

Schottky effect

Applied DC fields at the surface of solids can more easily reach substantial values compared to atomic systems, because the field between an emitter with local surface radius r and voltage U to an anode is

$$E_{\text{DC}} = \frac{U}{kr}, \quad (2.74)$$

where k is a geometric value that accounts for bulk shielding. For nanometric sharp tips it has been shown to be approximately $k \approx 4$ [125]. With a radius of $r \approx 50$ nm it is thus possible to easily reach $E_{\text{DC}} \approx 1$ GV/m with moderate voltages [126]. Due to the Schottky effect, this field lowers the effective work function to be overcome to

$$W_{\text{eff}} = W - \sqrt{\frac{e^3 E_{\text{DC}}}{4\pi\epsilon_0}}. \quad (2.75)$$

The field for which the barrier would vanish is given by $E_{\text{h}} = W^2 4\pi\epsilon_0 / e^3$. It is used to define the scaled barrier field as $f_{\text{h}} = E_{\text{DC}} / E_{\text{h}}$. Note that in most literature related to field emission, the electric field is denoted as F ; however, for consistency with the other sections, E is used here.

Fowler-Nordheim tunneling

The tunneling rate of electrons through a potential barrier under the influence of a static field is expressed using Fowler-Nordheim-type equations. In their original work, Fowler and Nordheim [127] assumed the barrier to have a triangular shape, softened by the imaging charge. This approximation has been refined over the years, and a common expression for the current density in a general Fowler-Nordheim equation is given by [128]

$$j = a \frac{E_{\text{DC}}^2}{W} \exp\left(-v(f_{\text{h}}) \frac{bW^{3/2}}{E_{\text{DC}}}\right), \quad (2.76)$$

with the first and second Fowler-Nordheim constants

$$a = e^3 / (16\pi^2 \hbar), \quad (2.77)$$

$$b = \frac{4\sqrt{2m_{\text{e}}}}{3e\hbar}. \quad (2.78)$$

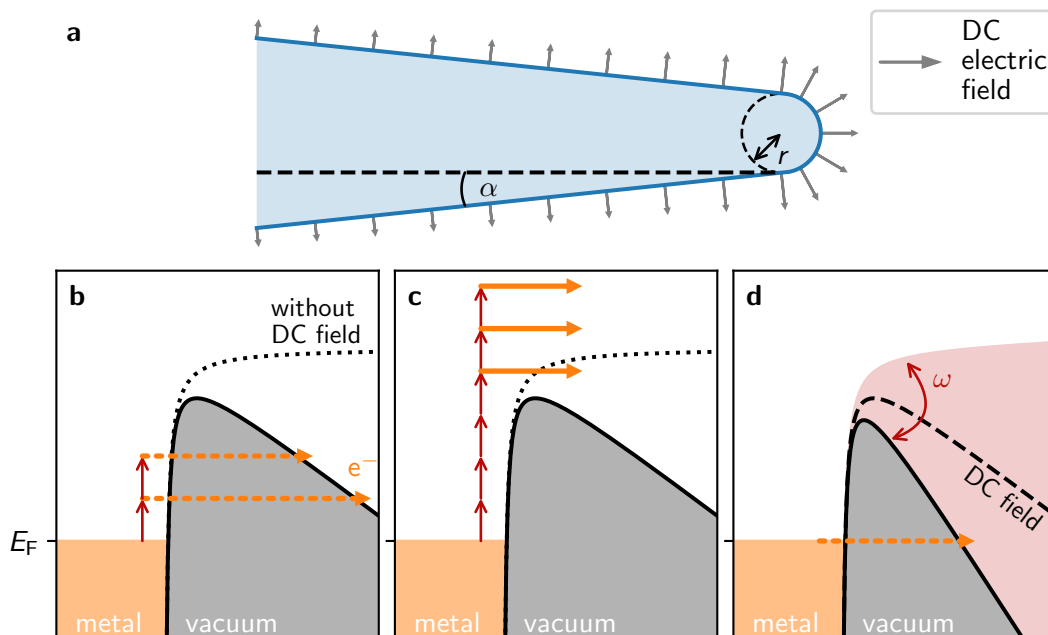


Figure 2.10: **a** A tip can be modeled by a sphere with radius r connected to a cone of opening angle α . For an applied voltage, the field is largest at the strongest curvature, as given by Eq. (2.74). **b-d** Dominant photoemission mechanisms from the Fermi level E_F for increasing light intensity: **b** photofield emission, **c** multiphoton photoemission, **d** optical field emission.

Note the similarity of the exponent with the Keldysh solution in Eq. (2.73). The correction factor v depends in general on the exact shape of the potential barrier. For the Schottky-Nordheim barrier, it can be well approximated by $v(f_h) \approx 1 - f_h + \ln(f_h)f_h/6$ [129]. This equation is derived for emission from flat surfaces. For strong curvatures $r < 20$ nm present in nanoscopic field-emitters, additional modifications have to be added [130].

Field enhancement at nanometric tips

When a nanometric tip is illuminated with light, the near-field at the tip can be significantly higher than in free space. There are two main reasons for this. First, the geometry causes a lightning rod effect, enhancing the field depending on the tip size and opening angle, as described by Eq. (2.74) and illustrated in Fig. 2.10 **a**. Second, electromagnetic waves on the surface between a dielectric (e.g. vacuum) and a metal, called surface plasmon polaritons, can confine the light energy, leading to an additional enhancement in plasmonic materials such as gold or silver [131–133]. For tungsten, the imaginary part of the complex permittivity is comparatively large, leading to a small damping time of these excitations of ~ 10 fs and thus a negligible plasmonic effect [126].

Regimes of photoemission at nanometric tips

The above concepts of static field emission and field enhancement can be used to understand photoemission from metallic tips. The geometry and, for some materials, the plasmonic properties of these tips allow high near-fields at the surface at intermediate

laser intensities. This enables nonlinear emission to be studied while avoiding sample damage even at high repetition rates. An additional DC field, which can become large at strong curvatures, lowers the binding potential, further facilitating emission. Similar to the atomic case, several emission regimes can be distinguished depending on intensity and the applied DC field [133]:

- Photofield emission or tunnel-assisted photoemission: The electrons are energetically lifted by one or more photons, leading to a nonthermal electron distribution above the Fermi level [134]. Subsequently, electrons from these states tunnel through a barrier that is suppressed by a DC field, as shown in Fig. 2.10 **b**.
- Multiphoton photoemission: Several photons are absorbed to lift electrons from the Fermi to the vacuum level, as depicted in Fig. 2.10 **c**. Additional photons can be absorbed analogous to ATI, resulting in above-threshold photoemission (ATP).
- Optical field emission or optically induced tunneling: The optical field bends the potential enough to allow electrons to tunnel directly out of the Fermi level, comparable to TI, as shown in Fig. 2.10 **d**. An additional DC field can facilitate the suppression of the barrier.

For the last two regimes, the Keldysh parameter can be defined analogously to the atomic case by replacing the ionization potential with the work function [135]. For photofield emission the Fowler-Nordheim Eq. (2.76) can be used with an effectively reduced work function $W - n\hbar\omega$ to estimate the emission rate. For the optical field emission, the same equation can be applied by summing the DC and the laser field $E = E_{\text{DC}} + E_{\text{laser}}$ [136]. Further theoretical approaches to calculate the emission in all regimes, along with experimental results and ongoing research in attosecond physics at nanometric tips, are extensively reviewed by Krüger *et al.* [137].

2.3.4 Electron diffraction in standing waves - The Kapitza-Dirac effect

The previous sections briefly summarized the concepts of electron liberation from bound atomic and solid-state systems in intense light fields. This section now focuses on the nonrelativistic interaction of light with free electrons.

In 1933 Peter Kapitza and Paul Dirac predicted the diffraction of electron matter waves by standing waves of light as stimulated Thomson scattering [54]. They estimated the size of the effect and came to the conclusion: "*We see, therefore, that the experiment could scarcely be made with ordinary continuous sources of light, and it seems to us that the only possibility would be to produce the illumination by using an intense spark discharge instead of a mercury arc.*" The idea to use a pulsed light source was very smart, but a spark discharge lamp was also not suited and it took nearly 30 years until the invention of the laser [2] provided this extraordinary light source needed and even more time to the first experimental realization. In 2001, the first coherent interference peaks were finally recorded with pulsed laser light [138].

The interpretation as stimulated Thomson or Compton scattering is called the particle picture and is illustrated in Fig. 2.11 **a**. The electron absorbs a photon with momentum $\hbar k_L$ from one side and gains an additional momentum shift by re-emitting it backwards, stimulated by the laser beam from the opposite side, resulting in a total momentum transfer of $2\hbar k_L$. This picture can be derived from the second quantization of the light field.

2 Theoretical background

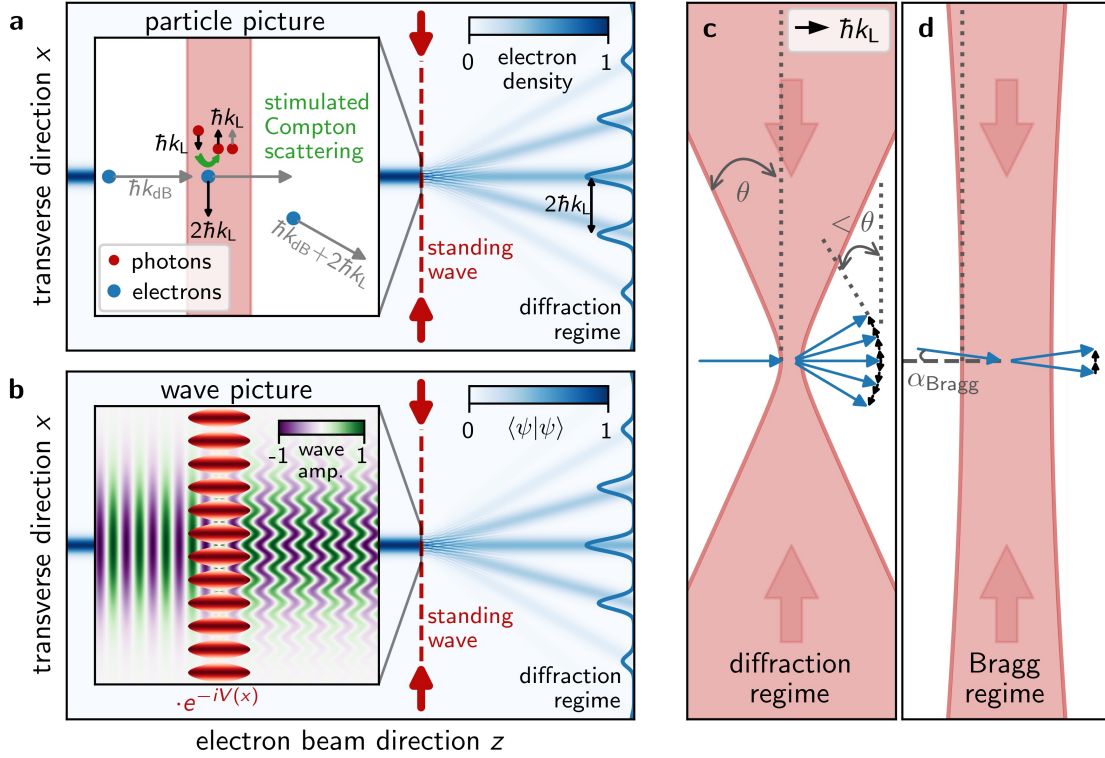


Figure 2.11: Different explanations and regimes of the Kapitza-Dirac effect. **a** In the particle picture, stimulated Compton scattering leads to diffraction peaks (blue colormap) separated by the transferred momentum $2\hbar k_L$. **b** In the wave picture, the electron matter wave is phase modulated by the periodic potential of the standing light wave, leading to the same diffraction peaks in the far field. The inset shows the periodic phase shifts at the standing wave. **c** The divergence angle θ of the focus determines if several diffraction peaks satisfy momentum conservation, or if **d** diffraction is only possible for the Bragg angle.

The same result can be obtained in the wave picture solving the Schrödinger equation. The electrons are treated as matter waves $|\psi\rangle$ with de-Broglie wavelength $\lambda_{\text{dB}} = h/p$, where p denotes the electron momentum and h is the Planck constant. The standing light field acts as a phase plate with the periodic potential $V(x, t)$, leading to a phase modulation of $|\psi\rangle(z, t) = |\psi_0\rangle \exp(-i/\hbar \int dt' V(x, t'))$. For potentials $V(x) \propto I(x) \propto \sin(2xk_L)$, the solution can be expanded in Bessel functions [139], leading to diffraction peaks separated by $2\hbar k_L$, as shown in Fig. 2.11 **b**. In the case of electrons, $V(x)$ is given by the ponderomotive potential $U_p \propto I$, defined in Eq. (2.66) as the average quiver energy of an electron in an oscillating field.

Several diffraction orders are only possible if the uncertainty of the photon momenta, related to the laser beam divergence θ , is large enough to fulfill momentum conservation. This is the so-called diffractive regime, also referred to as the Raman-Nath or thin lens regime, depicted in Fig. 2.11 **c**. In the Bragg (or thick lens) regime, the momentum spread of the photons is not large enough to generally satisfy momentum conservation. Only if the electrons pass the standing wave at the Bragg angle, given by $\sin(\alpha_{\text{Bragg}}) = k_L/k_{\text{dB}}$, diffraction is possible, as shown in Fig. 2.11 **d**. Refer to Batelaan [140], for an explana-

tion of these regimes exploiting the momentum-position uncertainty or the energy-time uncertainty.

Kapitza-Dirac diffraction of atoms and molecules

The term Kapitza-Dirac effect is also used for the diffraction of atoms or molecules by standing light fields. Given the polarizability α , the dipole αE , which is induced by the field E , leads for these larger systems to a potential $V = -1/2\alpha E^2 \propto I$ [139]. The first observation of the Kapitza-Dirac effect for atoms by Gould *et al.* [141] happened before the experimental realization with electrons. Even complex molecules can be diffracted [142], and the effect is nowadays used as a standard beam splitter in matter-wave interferometers [143, 144] or for calibration of optical lattices trapping ultracold atoms [145].

3 Publications

This chapter includes the main results in the form of four publications, formatted as they have been published, according to the rules for a cumulative thesis of the Department of Physics and Astronomy of the Heidelberg University. I am the second author of Publication 3.2 and the first author of the other three publications. Before each manuscript, a short description is provided, clarifying the background and the scientific goal of the publication.

First, Publication 3.1 starts with the smallest and fastest scales of this thesis. The recolliding electronic trajectories in helium atoms are studied dependent on the polarization of the driving laser. The second Publication 3.2 sets the stage for all following by introducing the experimental apparatus that allows intra-cavity multiphoton studies at 100 MHz repetition rate. The third Publication 3.3 investigates strong light-matter interaction on a nanometer scale by using the intrinsic nanometric structure of a standing wave to probe a metallic needle tip at the same scale. In the last Publication 3.4 standing waves are used to ionize xenon, demonstrating spatial selectivity in the 10s of micrometer.

3.1 Attosecond real-time observation of recolliding electron trajectories in helium at low laser intensities

Journal reference:

T. Heldt, J. Dubois, P. Birk, G. D. Borisova, G. M. Lando, C. Ott, and T. Pfeifer, Phys. Rev. Lett. **130**, 183201 (2023).

Digital object identifier (DOI): 10.1103/PhysRevLett.130.183201

Publication date: 5 May 2023

Author contribution:

I led the experimental measurements, data analysis, data visualization, TDSE simulations, and writing of the manuscript.

Supplementary material:

The accompanying supplementary material describes the experimental setup and details of the calculations.

Background:

The experimental part of this study was performed at an ATAS beamline, designed to investigate gaseous targets with NIR-XUV pump-probe experiments. Although this is an all-optical method, we have shown that it still allows conclusions to be drawn about electron trajectories. See [146] for more technical details on the setup, especially on an update that allows to measure an *in situ* reference of the XUV spectrum. This method was essential to detect broadband absorption features above the first ionization threshold of helium [147].

The reconstruction of the time-dependent dipole moment (see Eq. (2.16)) was initially introduced for resonant, narrow-band absorption lines [26] This raised the question of what insights can be gained from the reconstruction of broadband continuum features. They correspond to very low energy electron wave packets ionized by an attosecond XUV pulse. Since the ionization time is well defined, the wave packets can be considered to follow classical trajectories that a strong NIR field can modify, eventually driving them back to the ionic core, i.e. leading to a recollision. These electron trajectories are strongly affected by the polarization of the driving field. Increasing the ellipticity of the laser leads to an additional drift momentum of the electrons, which prevents a recollision, as can be seen from the strongly decreasing HHG yield [148]. Therefore, the objective of the study was to use the light polarization as a control parameter to resolve recollision features in the absorption spectrum of the ionizing XUV light. Surprisingly, the experiment revealed a parameter space with an increased recollision probability for circularly polarized light. In collaboration with the MPI for complex systems in Dresden, we developed a theory based on classical trajectories that explains this finding with the concepts of recolliding periodic orbits and envelope-driven recollisions.

Attosecond Real-Time Observation of Recolliding Electron Trajectories in Helium at Low Laser Intensities

Tobias Heldt^{1,*}, Jonathan Dubois², Paul Birk¹, Gergana D. Borisova¹, Gabriel M. Lando^{2,†},
Christian Ott¹ and Thomas Pfeifer^{1,‡}

¹Max-Planck-Institut für Kernphysik, Saupfercheckweg 1, 69117 Heidelberg, Germany

²Max-Planck-Institut für Physik komplexer Systeme, Nöthnitzer Straße 38, 01187 Dresden, Germany



(Received 30 September 2022; revised 20 February 2023; accepted 16 March 2023; published 5 May 2023)

Laser-driven recollision physics is typically accessible only at field intensities high enough for tunnel ionization. Using an extreme ultraviolet pulse for ionization and a near-infrared (NIR) pulse for driving of the electron wave packet lifts this limitation. This allows us to study recollisions for a broad range of NIR intensities with transient absorption spectroscopy, making use of the reconstruction of the time-dependent dipole moment. Comparing recollision dynamics with linear vs circular NIR polarization, we find a parameter space, where the latter favors recollisions, providing evidence for the so far only theoretically predicted recolliding periodic orbits.

DOI: 10.1103/PhysRevLett.130.183201

Strong few-cycle laser pulses have proven handy to get a deeper insight into ultrafast phenomena. The ability of this light to provoke an extreme nonlinear response makes it possible to study even subcycle regimes in time and space [1,2]. The most prominent example of such a strong-field interaction is high-harmonic generation (HHG) [3]. Not only does it render possible applications that make use of the resulting coherent, extreme ultraviolet (XUV) radiation such as attosecond transient absorption spectroscopy [4,5] or XUV frequency combs [6–8], but it allows us to learn about the ultrafast dynamics of matter itself in HHG spectroscopy [9–13]. The built-in mechanism behind HHG is recollision: The strong electric field of the generating radiation induces tunnel ionization of the electron and subsequently the classical trajectories of the electron wave packet go far away from the core and then come back and recollide. This is the popular three-step model for HHG [14,15].

By adding an attosecond XUV pulse, the first step of this model (tunnel ionization) is substituted by a single-photon ionization, which allows us to study recollision dynamics at arbitrary laser intensities and ionization times [16]. Using an attosecond pulse train, XUV-initiated HHG has been investigated with a focus on interference between discrete harmonics [17–20], achieving a chiral response measurement with interferometry between two polarization-controlled attosecond pulse trains [21].

Transmitting attosecond pulses through resonant media, it was found that changes of an isolated absorption line shape can be well explained through a time-domain picture of the system's dipole response [22,23]. The technique of reconstructing this time-dependent dipole moment directly from a measured absorption spectrum [24,25] paves the way for real-time investigations on atomic systems without the necessity of any delay sweeping. It has recently been applied to extract dynamics from a more complex absorption spectrum of a manifold of Rydberg states [26]. In this Letter, we open a new direction and demonstrate the reconstruction of recolliding continuum electron trajectories in real time, which is at the heart of strong-field-driven recollision physics. With the advantage of decoupling ionization and subsequent driving of the wave packet, we tune the near-infrared (NIR) intensity to a regime, where we can observe enhanced recollisions for circularly polarized (CP) fields, agreeing with theoretical predictions. Our approach thus provides a new view into ultrafast recollision dynamics of strong-field physics entering a new parameter regime of lower laser intensities and arbitrary laser polarization.

For a first demonstration, we study electron dynamics in helium, encoded in the time-dependent dipole moment. Figure 1(a) is a schematic of the mechanism. An XUV pulse excites a helium atom with an energy close to the first ionization threshold, leading to an excited electron wave packet $\Psi_1(0)$ with low kinetic energy, initially positioned on top of the electronic ground-state wave function Ψ_0 . A consecutive NIR pulse drives this wave packet in the vicinity of the ionic core back and forth. This leads to a modulation of the amplitude of the dipole moment $|d(t)|$, since it depends on the overlap of the excited wave packet

Published by the American Physical Society under the terms of the [Creative Commons Attribution 4.0 International license](https://creativecommons.org/licenses/by/4.0/). Further distribution of this work must maintain attribution to the author(s) and the published article's title, journal citation, and DOI. Open access publication funded by the Max Planck Society.

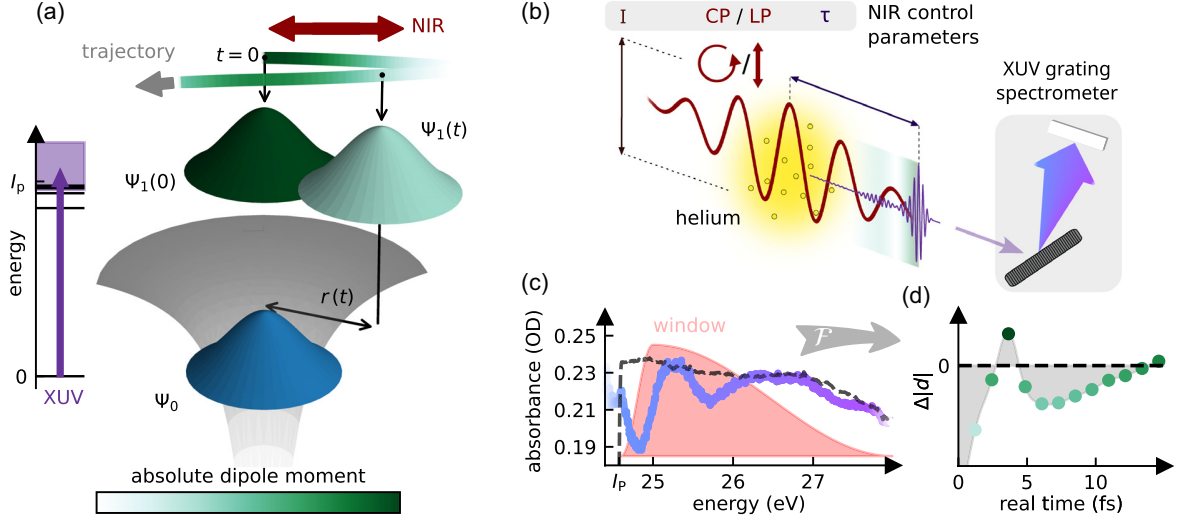


FIG. 1. Schematic of the measurement principle. (a) Illustration of the mechanism. The spatial representation of an electronic ground-state wave function (blue) is depicted in a Coulomb potential together with the XUV-produced excited wave packet (green) illustrated at two moments in time. The intensity of the green color scale along the NIR-driven trajectory illustrates the absolute dipole moment to the ground state. (b) Experimentally, an XUV (purple) and an NIR (red) pulse are focused into a helium gas target. The NIR pulse can be tuned in delay (τ) and intensity (I) with linear (LP) or circular polarization. The initial XUV field together with the dipole response of the system are analyzed in a grating spectrometer. The green shading illustrates the amplitude of the dipole response (not to scale). (c) The measured spectrum at the ionization edge is depicted in purple. The dashed curve is the spectrum without NIR interaction. By restricting to the relevant energy window (shown in pink), the amplitude modulation of the dipole moment shown in (d) is retrieved by a Fourier transform [Eq. (2)]. The dipole without NIR interaction is subtracted for better visibility.

and the ground state. On the one hand, if the former is moving away too far from the atomic core, the dipole moment vanishes. On the other hand, if the wave packet is driven back into spatial overlap with the ground state, i.e., it undergoes a recollision, the dipole moment revives and increases in amplitude. Therefore, the absolute dipole moment is modulated by the wave packet's trajectory, which is driven by the laser field. In the following, we present the measurement of this modulation and corresponding calculations based on semiclassical electron trajectories.

In our experimental apparatus, we focus an attosecond XUV and a strong few-cycle NIR pulse into a helium target as depicted in Fig. 1(b). The time delay between both pulses as well as the NIR intensity and NIR polarization can be controlled. The strong-field-driven dipole response $d(t)$ of the system interferes with the attosecond excitation pulse and the resulting spectrum is recorded by an XUV grating spectrometer. A diffraction grid for the XUV before the target (not shown) enables us to measure the absorption spectrum $I(\omega, \tau)$, with the interference signal imprinted, and the *in situ* reference spectrum $I_0(\omega)$ simultaneously in the spectrometer as described in [27]. This experimental procedure ensures the sensitivity to multi-eV broadband structures in the continuum XUV absorption spectrum. The absorbance follows the Lambert-Beer law

$$A(\omega, \tau) = -\log_{10} \left[\frac{I(\omega, \tau)}{I_0(\omega)} \right]. \quad (1)$$

Stoß *et al.* have shown in [24] that for such a measurement scheme $d(t)$ along the XUV polarization direction can be reconstructed by a Fourier transform operation. As the spectrum cannot be measured for all energies, only a limited spectral range given by the window function $w(\omega)$ is experimentally accessible with $d(t) \propto \mathcal{F}^{-1}[iw(\omega)A(\omega)]$ and more explicitly

$$d(t) \propto \frac{1}{2\pi} \int_{-\infty}^{\infty} iw(\omega)A(\omega) \exp(-i\omega t) d\omega, \quad (2)$$

for $t > 0$. In Fig. 1(c) this reconstruction process is illustrated. To focus on the continuum dynamics, we chose a window (shown in pink) that opens directly above the ionization potential. The reconstructed time-dependent dipole moment $d(t)$ is a complex quantity and contains amplitude and phase. In the presented analysis, only the amplitude is evaluated since it is directly connected to the overlap of the recolliding electron wave packet with the ground state. Figure 1(d) depicts the resulting reconstructed amplitude of the dipole moment after subtraction of the XUV-only dipole-moment amplitude. A clear local maximum can be seen at ~ 4 fs, the time where the NIR laser drives the XUV-ionized electron wave packet back to the residual ion. Note that absorption features above the first ionization threshold of helium for intensities $\leq 10^{13}$ W/cm² have also been interpreted in a dressed-state picture as so-called light-induced states [28–32]. Here, we do not follow

this approach, since we consider a significantly higher intensity regime. In the Supplemental Material [33] Fig. S2 we show the time-delay-dependent XUV absorption spectra which further confirms the breakdown of the dressed-state picture through the disappearance of sharp resonant features in the region of temporal overlap.

To verify the sensitivity of the dipole-moment amplitude to recollision dynamics, we solve the time-dependent Schrödinger equation (TDSE) on a 1D grid for the helium atom in single-active electron approximation (see Supplemental Material for details [33]). In this simulation, starting from the ground state $\psi_0(x)$, a wave packet is excited with an XUV pulse. The XUV excitation is followed by a strong NIR pulse (linearly polarized, electric field strength $E = 0.035$ a.u.), transform limited with a 5 fs FWHM Gaussian envelope at a center energy of $\omega_{\text{NIR}} = 1.7$ eV and at a time delay of 2 fs. Figure 2 shows the evolution of the wave packet corrected for the trivial action of single pulses as described in the following. The XUV pulse alone excites a dispersing wave packet $\psi_{\text{XUV}}(x, t)$, whereas the NIR pulse alone polarizes the ground state and leads to the wave packet $\psi_{\text{NIR}}(x, t)$. To reveal the XUV-initiated and subsequently NIR-driven dynamics, we subtract the changes that each pulse alone provokes from the changes that both pulses introduce together in the wave function amplitude

$$\Delta|\psi|(x, t) = (|\psi(x, t)| - |\psi_0(x)|) - (|\psi_{\text{NIR}}(x, t)| - |\psi_0(x)|) - (|\psi_{\text{XUV}}(x, t)| - |\psi_0(x)|). \quad (3)$$

After 3 fs the $\Delta|\psi|$ is mainly positive, thus the combined action of the XUV and NIR pulses increases the relative magnitude of the electron wave packet in the vicinity of the core, a first hint of recollision. The fast oscillations near the nucleus arise from bound states that were populated by the NIR pulse from the ionizing wave packet.

In order to further quantify the recollision dynamics, we calculate, in the joint field of Coulomb potential and NIR, a classical electron trajectory of an electron ionized by the XUV pulse. It is launched at $t = 0$ fs with initial kinetic energy set to 0.4 eV, which corresponds to the spectral intensity maximum of the XUV pulse of 25 eV [see Fig. 2(b)]. This trajectory is depicted with a white dashed line in Fig. 2(a), in close agreement with the local enhancement of the quantum calculation. It exhibits multiple crossings with the origin at $x = 0$ which confirms the presence of recollisions that agree between classical and quantum calculation.

The knowledge of the complete wave function $\psi(x, t)$ enables us to calculate directly the time-dependent dipole moment $d(t) = \langle \psi(t) | x | \psi(t) \rangle$ of the system. The left panel of Fig. 2(a) shows the absolute value of this dipole moment, filtered to the energy domain above the ionization threshold [the window is identical to the XUV spectrum given in purple in Fig. 2(b)]. The monotonically decreasing absolute

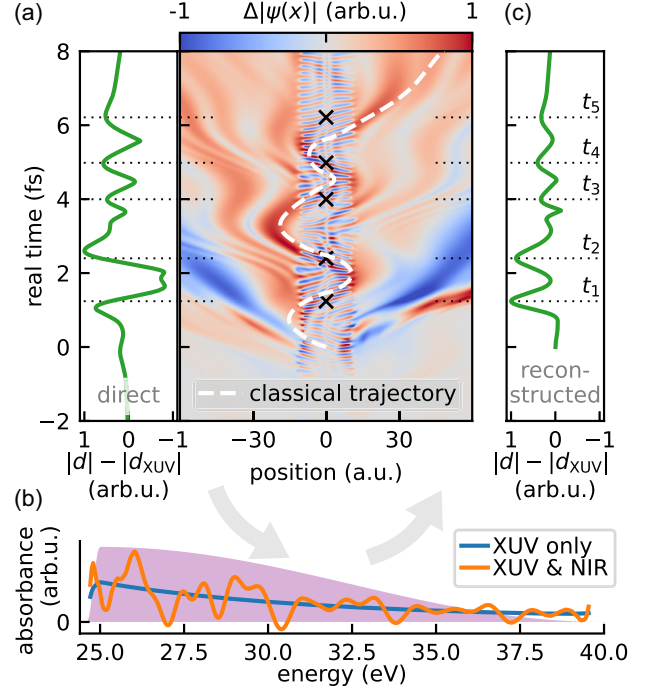


FIG. 2. 1D TDSE simulation results showing recollision features. (a) The time evolution of the NIR-introduced changes $\Delta|\psi|$ of a wave function triggered by an XUV pulse. The 5 fs FWHM NIR pulse with an intensity of 4.3×10^{13} W/cm² is delayed by 2 fs with respect to the XUV. The left panel shows the time-dependent dipole response difference between the NIR-driven and XUV-only case filtered by the window function. The white dashed line corresponds to a classical trajectory with 0.4 eV initial energy. It agrees with the local maxima of the electron probability distribution (dark red regions). (b) Absorbance spectra in the continuum calculated out of the dipole moment with and without the subsequent NIR pulse. The purple shaded area indicates the spectrum of the initial XUV pulse, which is identical with the window used for the dipole reconstruction. (c) The reconstructed absolute dipole moment calculated from the absorption spectrum according to Eq. (2). The times of local maxima t_i are marked with dotted black lines. They are also illustrated in panel (a), partly replaced by a cross at the origin for better visibility.

dipole moment $|d_{\text{XUV}}(t)|$ for the XUV-only case is also subtracted for clarity. It should be emphasized that the plotted quantity is experimentally inaccessible. The absorbance $A(\omega)$, originating from the interference of the dipole response with the initial XUV, could be measured in a transient absorption experiment and is given in Fig. 2(b). The spectrum shows broad features over the full range of XUV excitation without any distinct absorption lines, which makes it difficult to interpret. With Eq. (2), the dipole moment can be reconstructed from the absorption spectrum. The absolute value of the reconstructed dipole moment is displayed on Fig. 2(c). It can be directly compared to the original value in Fig. 2(a). The deviations are due to the fact that the XUV excitation was not delta-like, but with a finite pulse duration of 400 as FWHM. The times

t_i of the reconstructed dipole's local maxima [marked as dotted lines in Fig. 2(c), lines and crosses in Fig. 2(a)] agree well with their original positions. They also coincide near the zero crossings of the NIR-driven wave function of both the classical and the quantum calculation. This finding proves that the recolliding electron wave packet is encoded in the time-dependent absolute dipole moment, which one can reconstruct from the experimentally measured absorption spectrum.

In the following, we apply this reconstruction method to experimentally measured data and compare with classical trajectory Monte Carlo (CTMC) simulations in combined Coulomb plus laser field in three dimensions. To illuminate a large range of the relevant parameter space, the two control parameters NIR intensity and polarization are used. Both parameters have a strong impact on the resulting electron dynamics. Changing the intensity allows us to modify the ratio between light and ionic potential from a weakly perturbing to the strong-field regime. Changing the polarization of the NIR from linear to circular results in a completely different trajectory of the recolliding electron wave packet. Thus, to eliminate most background effects, we focus on the change of our observables while varying the control parameters NIR intensity and polarization. The resulting experimental observable is the difference between the time-dependent absolute dipole moments for circular and linear NIR polarization $|d_{CP}(t)| - |d_{LP}(t)|$. With classical mechanics and Monte Carlo techniques (see Supplemental Material for details [33]), we calculate accordingly the difference of the recollision probability of electron trajectories for the two NIR polarizations $P_{\text{recol},CP} - P_{\text{recol},LP}$ within the observable energy window.

Figure 3 depicts a comparison of our experimental (panel a) and simulated (panel b) results for a delay of 7 fs between XUV and NIR while tuning the NIR intensity. We note one main feature: For an intermediate intensity regime $I \sim [10^{12}, 10^{13}]$ W/cm², we observe a region of real times (blue “sea” area) in which circularly polarized light leads to less recollisions than for linear NIR polarization. On the contrary, for a higher intensity regime $I \sim [10^{13}, 10^{14}]$ W/cm², we observe a localized real-time range from 5 to 10 fs (red “island” area) in which recollision probability is enhanced for CP pulses. These characteristic structures are reproduced by theory. Differences between experiment and theory at early times might arise because initially bound states are not considered in the simulation. Recollision probabilities and HHG are generally known to be suppressed for increasing ellipticities of the NIR pulse due to an increase of the drift momentum which pushes the electron away from the core after tunnel ionization [15,39,40]. The blue sea in Fig. 3 is a consequence of this mechanism. In contrast, the red island of enhanced recollisions for CP pulses cannot be explained by this picture.

Theory predicts, for certain ionization times and laser intensities, the existence of recolliding periodic orbits [41]

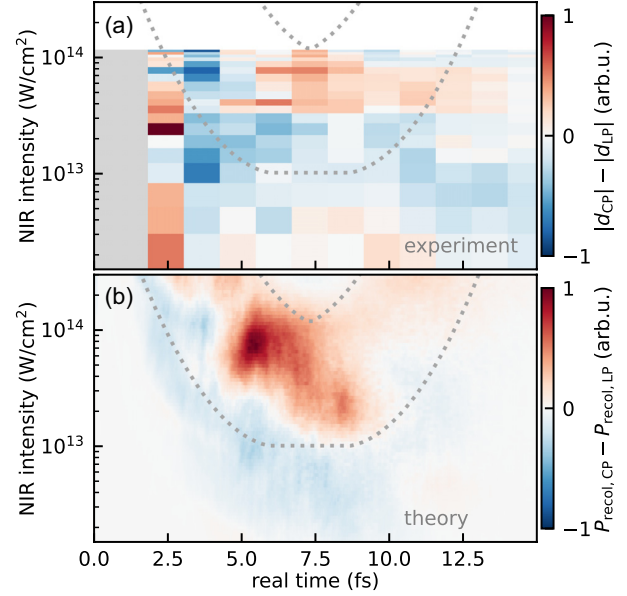


FIG. 3. (a) Difference between CP and LP of the time-dependent absolute dipole moment as a function of intensity from experiments. The first two experimental data points are grayed to account for the reconstruction error due to the finite XUV pulse duration. (b) Difference between CP and LP recollision probabilities as a function of recollision time and NIR intensity from CTMC simulations. The probabilities are weighted by the recollision angle $\cos^2 \alpha$, which takes into account that experimentally only the recollisions that happen in the same direction as the XUV polarization are observed. The time delay is $\tau = 7$ fs. Note the prominent red feature in both panels that is caused by enhanced recollisions for CP light. Between the gray dotted lines recolliding periodic orbits are predicted by theory for all considered recollision energies.

(RPOs), which drive recollisions in CP light. We calculate that the region for which relevant RPOs exist for all considered recollision energies lies between the dotted lines in Fig. 3. This region coincides with the observed red island. We thus conclude that we are able to populate the recollision channel structured by RPOs by decoupling ionization from the NIR field, which we achieve by using an XUV pulse. This can also be seen in spatial representation, where the recolliding trajectories mimic the shape of the RPOs, as illustrated in Fig. 4 for an exemplary set of recolliding trajectories. Altogether, our findings support the hypothesis, introduced in [41], that there exist RPOs which drive recollisions in CP light.

To conclude, by decoupling ionization and driving of an ultrafast electron wave packet, we were able to study XUV-initiated recollision dynamics for both linear and circular NIR polarization and a broad range of laser intensities. We have shown that the presence of recollisions is reflected in the absolute value of the time-dependent dipole moment, which can be reconstructed from experimentally measured absorption spectra in an attosecond-transient-absorption-geometry type experiment. Thus, real-time information

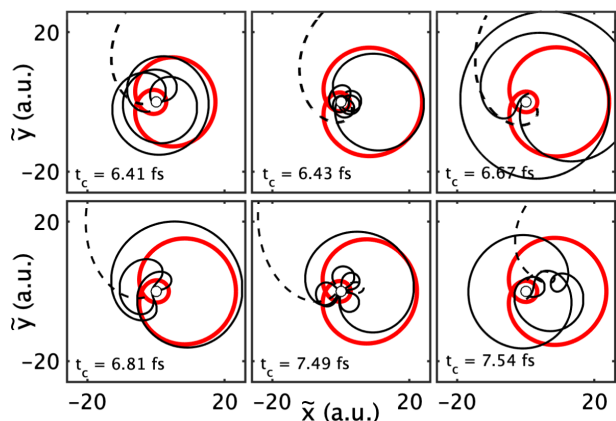


FIG. 4. Exemplary recolliding trajectories in the rotating frame for intensity $I = 10^{14}$ W/cm² and time delay $\tau = 7$ fs. Solid and dashed curves correspond to the trajectory before and after recollision, respectively. The red curves are RPOs associated with the respective recollision energy. The time of recollision t_c is indicated.

about laser-driven recollisions is accessible without delay sweeping. Both a quantum and a classical model capture well the recollision times that are encoded in the amplitude of the XUV-initiated dipole response. We find that at intermediate NIR laser intensities, recollisions are more likely for a circularly polarized laser pulse. This is a confirmation of previous theoretical studies, which proposed that the likelihood of recollisions for circular laser polarization in classical phase space is strongly connected to so-called recolliding periodic orbits.

In general, the new method described here opens a promising new direction for identifying laser-driven dynamics at arbitrary ellipticity in the continuum of complex XUV absorption spectra. For instance, for the emerging field of high-harmonic generation of solid-state systems, including topological and strongly correlated materials, the extraction of laser-driven dynamics offers new opportunities for understanding and laser controlling the electron dynamics at the natural femtosecond to attosecond time scale of electron motion. In addition, the method can be straightforwardly extended to molecules, providing a complementary experimental measure to laser-induced electron diffraction tomography, and can be applied to study reactive scattering processes in the continuum.

We acknowledge funding from the European Research Council (Grant No. X-MuSiC-616783).

*Corresponding author.
heldt@mpi-hd.mpg.de

†Present address: Center for Theoretical Physics of Complex Systems, Institute for Basic Science, Daejeon 34126, Korea.

‡Corresponding author.
thomas.pfeifer@mpi-hd.mpg.de

- [1] M. Kitzler, X. Xie, S. Roither, A. Scrinzi, and A. Baltuska, *New J. Phys.* **10**, 025029 (2008).
- [2] B. Piglosiewicz, S. Schmidt, D. J. Park, J. Vogelsang, P. Groß, C. Manzoni, P. Farinello, G. Cerullo, and C. Lienau, *Nat. Photonics* **8**, 37 (2014).
- [3] M. Lewenstein, P. Balcou, M. Y. Ivanov, A. L’Huillier, and P. B. Corkum, *Phys. Rev. A* **49**, 2117 (1994).
- [4] T. Pfeifer, M. J. Abel, P. M. Nagel, A. Jullien, Z.-H. Loh, M. Justine Bell, D. M. Neumark, and S. R. Leone, *Chem. Phys. Lett.* **463**, 11 (2008).
- [5] E. Goulielmakis, Z.-H. Loh, A. Wirth, R. Santra, N. Rohringer, V. S. Yakovlev, S. Zherebtsov, T. Pfeifer, A. M. Azzeer, M. F. Kling, S. R. Leone, and F. Krausz, *Nature (London)* **466**, 739 (2010).
- [6] C. Gohle, T. Udem, M. Herrmann, J. Rauschenberger, R. Holzwarth, H. A. Schuessler, F. Krausz, and T. W. Hänsch, *Nature (London)* **436**, 234 (2005).
- [7] R. J. Jones, K. D. Moll, M. J. Thorpe, and J. Ye, *Phys. Rev. Lett.* **94**, 193201 (2005).
- [8] J. Nauta, J.-H. Oelmann, A. Borodin, A. Ackermann, P. Knauer, I. S. Muhammad, R. Pappenberger, T. Pfeifer, and J. R. C. López-Urrutia, *Opt. Express* **29**, 2624 (2021).
- [9] J. Itatani, J. Levesque, D. Zeidler, H. Niikura, H. Pépin, J. C. Kieffer, P. B. Corkum, and D. M. Villeneuve, *Nature (London)* **432**, 867 (2004).
- [10] M. Lein, *Phys. Rev. Lett.* **94**, 053004 (2005).
- [11] S. Baker, J. S. Robinson, C. A. Haworth, H. Teng, R. A. Smith, C. C. Chirilă, M. Lein, J. W. G. Tisch, and J. P. Marangos, *Science* **312**, 424 (2006).
- [12] H. Soifer, P. Botheron, D. Shafir, A. Diner, O. Raz, B. D. Bruner, Y. Mairesse, B. Pons, and N. Dudovich, *Phys. Rev. Lett.* **105**, 143904 (2010).
- [13] P. Lan, M. Ruhmann, L. He, C. Zhai, F. Wang, X. Zhu, Q. Zhang, Y. Zhou, M. Li, M. Lein, and P. Lu, *Phys. Rev. Lett.* **119**, 033201 (2017).
- [14] K. J. Schafer, B. Yang, L. F. DiMauro, and K. C. Kulander, *Phys. Rev. Lett.* **70**, 1599 (1993).
- [15] P. B. Corkum, *Phys. Rev. Lett.* **71**, 1994 (1993).
- [16] Q. Liu, A. Piper, D. Kiesewetter, Y. Tang, P. Agostini, K. J. Schafer, and L. F. DiMauro, in *The International Conference on Ultrafast Phenomena (UP) 2022* (Optica Publishing Group, Washington, DC, 2022), p. Tu4A.37, 10.1364/UP.2022.Tu4A.37.
- [17] J. Biegert, A. Heinrich, C. P. Hauri, W. Kornelis, P. Schlup, M. P. Anscombe, M. B. Gaarde, K. J. Schafer, and U. Keller, *J. Mod. Opt.* **53**, 87 (2006).
- [18] G. Gademann, F. Kelkensberg, W. K. Siu, P. Johnsson, M. B. Gaarde, K. J. Schafer, and M. J. J. Vrakking, *New J. Phys.* **13**, 033002 (2011).
- [19] D. Azoury, M. Krüger, G. Orenstein, H. R. Larsson, S. Bauch, B. D. Bruner, and N. Dudovich, *Nat. Commun.* **8**, 1453 (2017).
- [20] M. Krüger, D. Azoury, B. D. Bruner, and N. Dudovich, *Appl. Sci.* **9**, 378 (2019).
- [21] D. Azoury, O. Kneller, M. Krüger, B. D. Bruner, O. Cohen, Y. Mairesse, and N. Dudovich, *Nat. Photonics* **13**, 198 (2019).
- [22] C. Ott, A. Kaldun, P. Raith, K. Meyer, M. Laux, J. Evers, C. H. Keitel, C. H. Greene, and T. Pfeifer, *Science* **340**, 716 (2013).

- [23] A. Blättermann, C. Ott, A. Kaldun, T. Ding, and T. Pfeifer, *J. Phys. B* **47**, 124008 (2014).
- [24] V. Stooß, S. M. Cavaletto, S. Donsa, A. Blättermann, P. Birk, C. H. Keitel, I. Březinová, J. Burgdörfer, C. Ott, and T. Pfeifer, *Phys. Rev. Lett.* **121**, 173005 (2018).
- [25] X. Wu, L. Zhang, S. Zhang, and D. Ye, *Phys. Rev. A* **104**, 063121 (2021).
- [26] V. Stooß, P. Birk, A. Blättermann, M. Hartmann, G. D. Borisova, C. Ott, and T. Pfeifer, *Phys. Rev. Res.* **2**, 032041(R) (2020).
- [27] V. Stooß, M. Hartmann, P. Birk, G. D. Borisova, T. Ding, A. Blättermann, C. Ott, and T. Pfeifer, *Rev. Sci. Instrum.* **90**, 053108 (2019).
- [28] T. Halfmann, L. P. Yatsenko, M. Shapiro, B. W. Shore, and K. Bergmann, *Phys. Rev. A* **58**, R46 (1998).
- [29] S. Chen, M. Wu, M. B. Gaarde, and K. J. Schafer, *Phys. Rev. A* **87**, 033408 (2013).
- [30] M. Chini, X. Wang, Y. Cheng, Y. Wu, D. Zhao, D. A. Telnov, S.-I. Chu, and Z. Chang, *Sci. Rep.* **3**, 1105 (2013).
- [31] M. Reduzzi, J. Hummert, A. Dubrouil, F. Calegari, M. Nisoli, F. Frassetto, L. Poletto, S. Chen, M. Wu, M. B. Gaarde, K. Schafer, and G. Sansone, *Phys. Rev. A* **92**, 033408 (2015).
- [32] P. Birk, V. Stooß, M. Hartmann, G. D. Borisova, A. Blättermann, T. Heldt, K. Bartschat, C. Ott, and T. Pfeifer, *J. Phys. B* **53**, 124002 (2020).
- [33] See Supplemental Material at <http://link.aps.org/supplemental/10.1103/PhysRevLett.130.183201> for experimental details and a description of the performed calculations, which includes Refs. [34–38].
- [34] L.-Y. Peng, W.-C. Jiang, J.-W. Geng, W.-H. Xiong, and Q. Gong, *Phys. Rep.* **575**, 1 (2015).
- [35] J. Javanainen, J. H. Eberly, and Q. Su, *Phys. Rev. A* **38**, 3430 (1988).
- [36] F. Mauger, A. D. Bandrauk, A. Kamor, T. Uzer, and C. Chandre, *J. Phys. B* **47**, 041001 (2014).
- [37] A. D. Bandrauk and H. Shen, *Chem. Phys. Lett.* **176**, 428 (1991).
- [38] M. B. Gaarde, C. Buth, J. L. Tate, and K. J. Schafer, *Phys. Rev. A* **83**, 013419 (2011).
- [39] P. Antoine, A. L’Huillier, M. Lewenstein, P. Salières, and B. Carré, *Phys. Rev. A* **53**, 1725 (1996).
- [40] M. Möller, Y. Cheng, S. D. Khan, B. Zhao, K. Zhao, M. Chini, G. G. Paulus, and Z. Chang, *Phys. Rev. A* **86**, 011401(R) (2012).
- [41] A. Kamor, F. Mauger, C. Chandre, and T. Uzer, *Phys. Rev. Lett.* **110**, 253002 (2013).

Supplementary Material: Attosecond real-time observation of recolliding electron trajectories in helium at low laser intensities

Tobias Heldt,^{1,*} Jonathan Dubois,² Paul Birk,¹ Gergana D. Borisova,¹
Gabriel M. Lando,^{2,†} Christian Ott,¹ and Thomas Pfeifer^{1,‡}

¹Max-Planck-Institut für Kernphysik, Saupfercheckweg 1, 69117 Heidelberg, Germany

²Max-Planck-Institut für Physik komplexer Systeme, Nöthnitzer Straße 38, 01187 Dresden, Germany

Experimental Setup

The experimental setup used for the presented data consists of a Ti:Sapphire based laser system (3 kHz repetition rate, 1 mJ pulse energy, 6 fs pulse duration at 760 nm central wavelength) and an ultra-high vacuum beamline. A 70:30 beamsplitter separates the NIR light. As illustrated in FIG. S1, the intense part produces an extreme ultraviolet pulse by means of high harmonic generation in xenon and is dumped afterwards. The smaller fraction of the NIR is time-delayed with a retroreflector on a stage, polarization and intensity controlled by a $\lambda/4$ waveplate and an iris, and focused in the helium gas cell together with the XUV. Hereby, the XUV is linearly polarized, parallel to the polarization direction of the NIR for the linear polarized case.

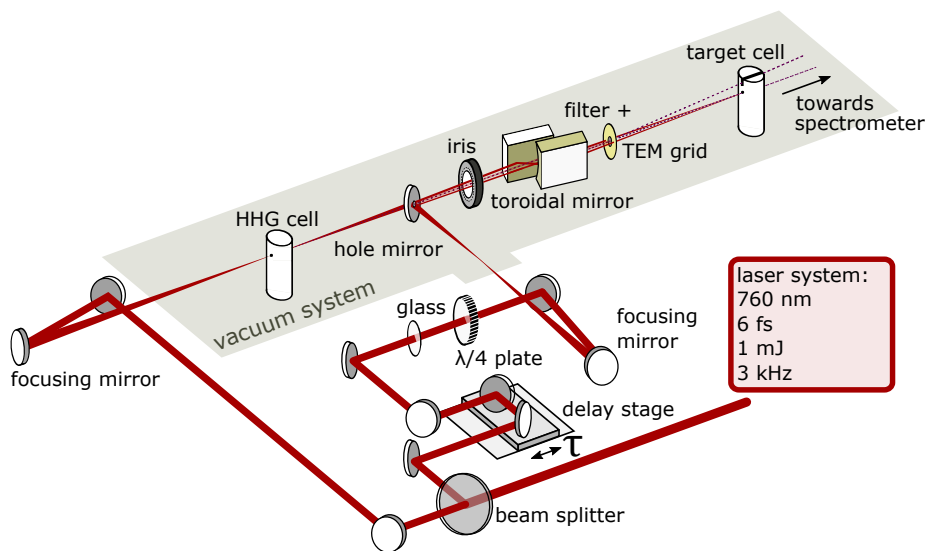


FIG. S1. Drawing of the experimental setup. The filter blocks the NIR that was used for XUV generation and the TEM (Transmission Electron Microscopy) grid diffracts the XUV. The fundamental diffraction order probes the helium and the first order is pictured unperturbed on the upper part of the spectrometer to obtain an *in situ* reference spectrum as described in [1]. All non-labelled elements are plane mirrors.

Experimental Parameters

NIR intensity calibration was determined with measured beam profiles in the focus, the measured pulse energy and pulse duration. To account for pedestal of the NIR pulse and imperfect alignment, maximal intensities were reduced by a factor of 2. The absolute time delay between XUV and NIR was determined by an independent data analysis and has an uncertainty of ~ 2 fs.

Data Acquisition

The integration time of a single absorption spectrum has been set to 3 s, i.e., accumulating 7000 single-shot spectra. The resulting dipole moments were averaged over 5 (7) time-delay and intensity scans for circular (linear) NIR polarization during a total measurement time of 10 h.

Time-Dependent Absorption Spectra

In Fig. S2 we present the time-delay-dependent absorption spectra of helium from -15 fs to 50 fs, in the vicinity of the first ionization threshold. At the given NIR intensity ($\sim 7 \cdot 10^{13} \text{ W/cm}^2$), we observe the discrete lines (corresponding to the 1snp bound states) to disappear within the region of temporal overlap (between 0 and $+10$ fs).

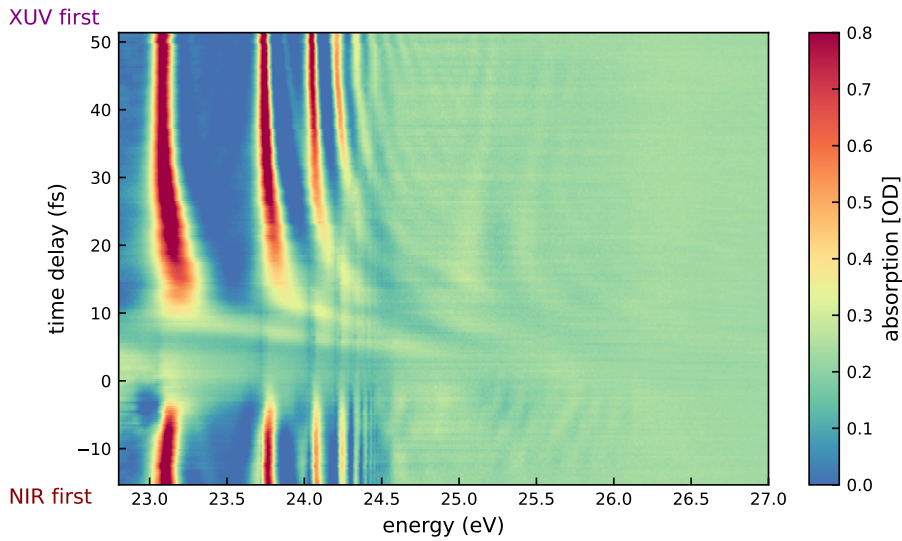


FIG. S2. Time-dependent absorption spectra of helium for linearly polarized NIR at an intensity of $\sim 7 \cdot 10^{13} \text{ W/cm}^2$. Note that in the temporal overlap of NIR and XUV the absorption lines of the 1snp bound states disappear due to the strong field.

Classical Simulations

For the calculation of the recolliding probabilities, we use classical trajectories whose dynamics are governed by the Hamiltonian in the dipole approximation [2]

$$H(\mathbf{r}, \mathbf{p}, t) = \frac{|\mathbf{p}|^2}{2} + V(\mathbf{r}) + \mathbf{r} \cdot \mathbf{F}(t), \quad (1)$$

where \mathbf{r} is the position and \mathbf{p} its canonically conjugate variable, $V(\mathbf{r}) = -(|\mathbf{r}|^2 + a^2)^{-1/2}$ is the soft-core potential [3] with softening parameter $a=0.26$ to model He [4]. The NIR pulse is

$$\mathbf{F}(t) = F \exp\left[-\frac{(t-\tau)^2}{2T^2}\right] \left(\mathbf{e}_x \cos(\omega t) + \xi \mathbf{e}_y \sin(\omega t) \right), \quad (2)$$

with τ the time delay between the XUV and the NIR pulses, $T=6$ fs the pulse duration, $\omega=0.0569$ a.u. its frequency (corresponding to a wavelength of $\lambda=800$ nm), ξ the polarization ($\xi=0$ LP, $\xi=1$ CP), $F^2=I/(\xi^2+1)$ the pulse amplitude and I its intensity with conversion $I [\text{W cm}^{-2}] = 3.5 \times 10^{16} I [\text{a.u.}]$. The recollision probability is detected when $|\mathbf{r}| < R$ (we have chosen $R=1$ a.u.) and the energy is $H(\mathbf{r}, \mathbf{p}, t) \in [0, 0.15]$ a.u. corresponding to the energy window of the experimental analysis.

The properties of the XUV pulse are in the initial conditions of the electron trajectories. The time delay of the laser is normally distributed with expectation value τ and standard deviation 1 fs. The electron trajectories are initialized at $t=0$: The initial position is randomly distributed in a unit circle and the initial momentum is along the XUV direction \mathbf{e}_x such that the initial energy $E = H(\mathbf{r}, \mathbf{p}, 0)$ is normally distributed with expectation value E_0 and standard deviation 2.7 eV (approximate spectral bandwidth of the XUV pulse). The expectation value is the most probable energy of the electron after ionization by the XUV pulse $E_0 = -I_p + \Omega$ with $I_p=0.89$ a.u. the ionization potential of He and $\Omega=0.9044$ a.u. the frequency of the XUV pulse.

The rotating frame is defined as the frame in which the NIR pulse is only along one direction. This is done by performing the time-dependent canonical change of coordinates $\tilde{\mathbf{r}}=\mathbb{R}(\omega t)\mathbf{r}$ and $\tilde{\mathbf{p}}=\mathbb{R}(\omega t)\mathbf{p}$ with

$$\mathbb{R}(\omega t) = \begin{bmatrix} \cos(\omega t) & \sin(\omega t) & 0 \\ -\sin(\omega t) & \cos(\omega t) & 0 \\ 0 & 0 & 1 \end{bmatrix}. \quad (3)$$

In this frame, the Hamiltonian governing the dynamics of the electron is [5]

$$\tilde{H}(\tilde{\mathbf{r}}, \tilde{\mathbf{p}}, t) = \frac{|\tilde{\mathbf{p}}|^2}{2} + V(\tilde{\mathbf{r}}) - \omega \tilde{\mathbf{r}} \times \tilde{\mathbf{p}} \cdot \mathbf{e}_z + \tilde{\mathbf{r}} \cdot \tilde{\mathbf{F}}(t), \quad (4)$$

with laser pulse

$$\tilde{\mathbf{F}}(t) = F \exp\left[-\frac{(t-\tau)^2}{2T^2}\right] \mathbf{e}_x. \quad (5)$$

As a result of this canonical change of coordinates, the Hamiltonian depends on the envelope of the laser pulse only, which varies on longer timescales than the timescales associated with its oscillations. This results in a time-independent dynamics on timescales shorter than the timescales of the laser envelope $f(t)$. The periodic orbits correspond to periodic solutions of (4). The energy of the electron in the LF and in the RF are related by $H(\mathbf{r}, \mathbf{p}, t) = \tilde{H}(\tilde{\mathbf{r}}, \tilde{\mathbf{p}}, t) + \omega L_z$ with the angular momentum orthogonal to the polarization plane $L_z = \tilde{\mathbf{r}} \times \tilde{\mathbf{p}} \cdot \mathbf{e}_z = \mathbf{r} \times \mathbf{p} \cdot \mathbf{e}_z$.

1D-TDSE Wave Function Simulations

We propagate the electronic wave function in one spatial dimension assuming a single active electron starting from the ground state. Calculations are carried out on a grid of $N=4096$ points corresponding to a position space of $x=[-511.75, 512.00]$ atomic units. The soft-core Coulomb potential [3] $V(\mathbf{r}) = -(|\mathbf{r}|^2 + a^2)^{-1/2}$ with $a=0.233$ is extended with an imaginary part, that leads to absorbing boundaries for $|x|>350$ a.u. to suppress reflections from the finite grid size. The time-dependent Schrödinger equation (TDSE) with the Hamiltonian of eq. (1) in one dimension, i.e. $H(x, p, t) = p^2/2 + V(x) + xF(t)$ with the electric field of the laser $F(t)$, is solved with a split-step algorithm [6] with a step size of $\delta t=0.05$ a.u.=1.2 as. Convergence has been checked with smaller time steps and results in velocity and length gauge differ negligibly. The absorbance spectra are calculated according to [7]

$$A(\omega) \propto \omega \operatorname{Im} \left[\frac{\mathcal{F}(d(t))}{\mathcal{F}(F(t))} \right], \quad (6)$$

with the dipole moment $d(t) = \langle \psi(t) | x | \psi(t) \rangle$.

* Corresponding author. heldt@mpi-hd.mpg.de

† Present address: Center for Theoretical Physics of Complex Systems, Institute for Basic Science, Daejeon 34126, Korea

‡ Corresponding author. thomas.pfeifer@mpi-hd.mpg.de

- [1] V. Stooß, M. Hartmann, P. Birk, G. D. Borisova, T. Ding, A. Blättermann, C. Ott, and T. Pfeifer, *Review of Scientific Instruments* **90**, 053108 (2019).
- [2] L.-Y. Peng, W.-C. Jiang, J.-W. Geng, W.-H. Xiong, and Q. Gong, *Physics Reports* **575**, 1 (2015).
- [3] J. Javanainen, J. H. Eberly, and Q. Su, *Phys. Rev. A* **38**, 3430 (1988).
- [4] F. Mauger, A. D. Bandrauk, A. Kamor, T. Uzer, and C. Chandre, *Journal of Physics B: Atomic, Molecular and Optical Physics* **47**, 041001 (2014).
- [5] A. Kamor, F. Mauger, C. Chandre, and T. Uzer, *Phys. Rev. Lett.* **110**, 253002 (2013).
- [6] A. D. Bandrauk and H. Shen, *Chemical Physics Letters* **176**, 428 (1991).
- [7] M. B. Gaarde, C. Buth, J. L. Tate, and K. J. Schafer, *Phys. Rev. A* **83**, 013419 (2011).

3.2 Photoelectron tomography with an intra-cavity velocity-map imaging spectrometer at 100 MHz repetition rate

Journal reference:

J.-H. Oelmann, T. Heldt, L. Guth, J. Nauta, N. Lackmann, V. Wössner, S. Kokh, T. Pfeifer, and J. R. Crespo López-Urrutia, *Rev. Sci. Instrum.* **93**, 123303 (2022).

Digital object identifier (DOI): 10.1063/5.0104679

Publication date: 7 December 2022

Author contribution:

I led the software development and contributed equally to the formal analysis, investigation, methodology, visualization, and reviewing and editing of the manuscript.

Background:

In this paper, we transition to a different experimental setup and methodology, shifting the focus from observing absorption spectra to ionized electrons, and from intra-cycle or few-femtosecond effects to a time scale of 200 fs, by using longer laser pulses.

In a previous work [39], we implemented velocity-map imaging (VMI) with multiphoton ionization (MPI) of xenon in an enhancement cavity designed for XUV frequency comb generation. This approach is promising due to the very high repetition rates and the absence of space charge effects, as only a single electron is emitted per laser pulse. However, the existing optical setup was not perfectly suited due to space and polarization restrictions.

In response, this publication describes the technical details of a new dedicated cavity equipped with a novel electron spectrometer, which allows to measure angularly resolved spectra of ATI at 100 MHz to observe processes with low cross sections. As an additional motivation, three-dimensional reconstruction of electron vortices has been demonstrated by Wollenhaupt *et al.* [149], and we aim to adapt the tomographic technique to higher-order MPI. In this study, we successfully apply tomography to photoelectron angular distributions of ionized xenon and identify atomic resonances.

Photoelectron tomography with an intra-cavity velocity-map imaging spectrometer at 100 MHz repetition rate

Cite as: Rev. Sci. Instrum. 93, 123303 (2022); doi: 10.1063/5.0104679

Submitted: 20 June 2022 • Accepted: 16 November 2022 •

Published Online: 7 December 2022



View Online



Export Citation



CrossMark

J.-H. Oelmann,^{1,2,a)} T. Heldt,^{1,2} L. Guth,¹ J. Nauta,^{1,2,b)} N. Lackmann,¹ V. Wössner,¹ S. Kokh,¹
T. Pfeifer,¹ and J. R. Crespo López-Urrutia¹

AFFILIATIONS

¹Max-Planck-Institut für Kernphysik, Saupfercheckweg 1, 69117 Heidelberg, Germany

²Heidelberg Graduate School for Physics, Im Neuenheimer Feld 226, 69120 Heidelberg, Germany

^{a)}Author to whom correspondence should be addressed: jan-hendrik.oelmann@mpi-hd.mpg.de

^{b)}Current address: Department of Physics, College of Science, Swansea University, Singleton Park, SA2, United Kingdom.

ABSTRACT

We present a compact velocity-map imaging (VMI) spectrometer for photoelectron imaging at 100 MHz repetition rate. Ultrashort pulses from a near-infrared frequency comb laser are amplified in a polarization-insensitive passive femtosecond enhancement cavity. In the focus, multi-photon ionization (MPI) of gas-phase atoms is studied tomographically by rotating the laser polarization. We demonstrate the functioning of the VMI spectrometer by reconstructing photoelectron angular momentum distributions from xenon MPI. Our intra-cavity VMI setup collects electron energy spectra at high rates, with the advantage of transferring the coherence of the cavity-stabilized femtosecond pulses to the electrons. In addition, the setup will allow studies of strong-field effects in nanometric tips.

© 2022 Author(s). All article content, except where otherwise noted, is licensed under a Creative Commons Attribution (CC BY) license (<http://creativecommons.org/licenses/by/4.0/>). <https://doi.org/10.1063/5.0104679>

I. INTRODUCTION

Velocity-map imaging (VMI) is an essential method to study charged particles.¹ It combines the advantage of 4π solid angle collection efficiency with the ability to simultaneously measure the kinetic energy and angular distribution of charged particles.^{2–6} This is possible by an inhomogeneous electric extraction field, which focuses the particles onto the detector. The VMI technique was introduced by Eppink and Parker³ as an improvement of the imaging technique from Chandler and Houston⁷ and is commonly utilized to study above-threshold ionization (ATI).⁸ It was originally developed to study gas-phase molecular reaction dynamics and is now a well-established method with a special emphasis on photofragmentation and inelastic scattering experiments.^{9–13} VMI has become a widely used tool in attosecond science^{14–17} and has been used to study ionization time delays by means of the attoclock technique.¹⁸ Recently, vortex-shaped photoelectron angular distributions (PADs) were produced by polarization-shaped ultrashort laser pulses and tomographically reconstructed utilizing

VMI.^{19–21} Compared to cold-target recoil-ion momentum spectroscopy (COLTRIMS)²² with reaction microscopes (REMI),²³ which allow coincidence measurements, it offers the benefits of reduced technical complexity, handling higher count rates, and insensitivity to the size of the ionization volume. It has been shown that coincidence measurements are also possible with modified VMI setups.^{24–28}

In a recent first demonstration of intra-cavity VMI at 100 MHz repetition rate,²⁹ we investigated multi-photon ionization (MPI) events even at very low intensities with count rates between kHz and MHz and resolved the angular structure of PADs.

In this paper, we present the design, construction, and operation of a new dedicated VMI spectrometer that is compact enough for intra-cavity use and incorporates many crucial improvements over our earlier proof-of-principle version. First, image deformations are avoided by shielding all nonconducting surfaces, and magnetic shielding is added around the flight path. In addition, without loss of compactness, the number of electrodes is greatly increased to allow for more versatile experiments, while still recording less than

a single ionization event per pulse to mitigate space-charge effects due to interacting electrons and ions. Finally, a new, polarization-insensitive cavity geometry is implemented, allowing for the first 3D reconstruction of PADs at 100 MHz with the accompanying advantage of short data acquisition times. In future experiments, the coherence of the cavity-enhanced frequency comb pulses could be utilized to measure electronic transitions and dynamics with unprecedented precision.

This paper is organized as follows: In Sec. II, a short overview of the newly developed polarization-insensitive optical setup is given, followed by a detailed description of the design, fabrication, and assembly of the new VMI spectrometer. After introducing the tomographic reconstruction method, we present a first xenon MPI experiment and demonstrate photoelectron tomography in Sec. III, before the concluding remarks in Sec. IV.

II. EXPERIMENTAL SETUP

A. Optical setup

In this work, we employ a commercial 100 MHz frequency comb laser (Menlo Systems, FC1000-250) with a 15 nm FWHM spectral bandwidth centered around 1039 nm as a seed laser for a homebuilt high-power fiber amplifier. Chirped pulses from

this laser with a duration of ~ 24 ps and 12 W average power are amplified in an 80 cm long Yb-doped photonic-crystal fiber rod (NKT photonics, aeroGAIN-ROD-MODULE-2.0), pumped by a 250 W continuous wave laser diode at 976 nm (DILAS, D4F2S22-976.3-250C-IS58.1). After amplification, the pulses are compressed to a pulse duration of 184 fs at 88 W of average power using a 1000 grooves/mm transmission grating (Gitterwerk GmbH, 1158-28 \times 18-6.35-H) with a total compressor efficiency of 95%. We measured the pulse duration by intensity frequency-resolved optical gating (FROG),³⁰ shown in Fig. 1(a). Pulses are fed into an *in vacuo* polarization-insensitive femtosecond enhancement cavity, where consecutive pulses interfere constructively. We use this laser system also for extreme-ultraviolet frequency comb generation in a second cavity inside the same vacuum chamber.³¹

The 3 m long bow-tie ring cavity consists of one cylindrical input coupler (IC) for astigmatism compensation and five highly reflective mirrors, two of which are concave focusing mirrors (CM1, CM2). One flat piezo-actuated mirror (PZT) is used to change the cavity length. High intensities in the range of 10^{13} W cm⁻² are reached in the cavity focus with a beam radius of 25 μ m [Fig. 1(b)] when the length of the cavity matches the repetition rate of the driving frequency comb. More details of the optical setup will be published separately.

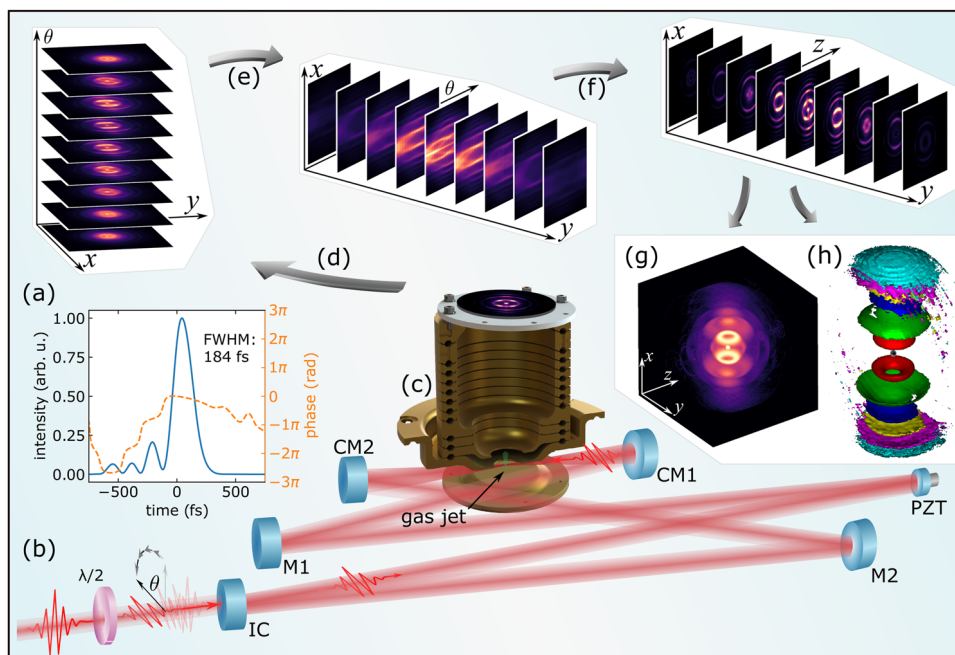


FIG. 1. Schematic overview of the experimental setup and the tomographic method. (a) Femtosecond pulses with a pulse duration of 184 fs, determined by a FROG measurement, (b) are fed into a resonant bow-tie cavity at a repetition rate of 100 MHz. To perform tomography, the polarization is rotated by θ between each acquisition step with a motorized half-wave plate ($\lambda/2$) before the input coupler (IC) mirror. The light is focused by two curved mirrors (CM1, CM2), and a piezo-actuated mirror (PZT) is used to adjust the cavity length. Two additional flat mirrors (M1, M2) are used to fold the cavity to reduce the outer dimensions of the ring cavity with a path length of 3 m. (c) Atoms from a gas jet are ionized by the laser pulses in the cavity focus and PADs are mapped on the MCP detector by the VMI spectrometer. (d) Detector images are recorded for each polarization angle θ and stacked together into a single array. (e) Slices of this array (the sinograms) are extracted for each y -pixel, (f) reconstructed by filtered back-projection one by one, and stacked to a 3D array, yielding the reconstructed 3D PAD. Visualization of the 3D PAD either as a (g) maximum intensity projection plot or an (h) isosurface plot. The individual ATI-shells are identified and highlighted in different colors (in rising order: gray, red, green, blue, yellow, purple, cyan). Note that, compared to (g), some details are lost due to the restriction of one iso-value per shell.

B. VMI design considerations

In a recently reported VMI design, a photoelectron kinetic energy resolution of $\Delta E/E \approx 0.53\%$ has been demonstrated experimentally.³² In that work, conventional plate electrodes held by spacers were used to focus the electrons through a 500 mm long double μ -metal shielded flight tube onto the MCP detector. Even though this design is desirable for VMI applications, the given small vertical dimension of our vacuum chamber and the fixed horizontal distance of the cavity focusing mirrors dictated strict space limitations. Thus, the development of a novel compact and shielded VMI setup for intra-cavity operation is required (see Fig. 2).

Electrostatic shielding is important because we aim to study low energy electrons, which are strongly influenced by electric potentials. Moreover, electromagnetic waves are a concern, if no shielding is applied. A main goal for the VMI design is a versatile spectrometer platform, which can be extended in the future. For that reason, we use a stack of 13 electrodes instead of only three electrodes and a flight tube. This enables precise control over the imaging capabilities of the setup by shaping the potential landscape inside the spectrometer, which has been shown to improve the resolution and maximum attainable energy.^{32–37}

For future upgrades and modifications, the platform should provide the option to exchange the standard electrodes with other components, such as an electrode with integrated gas injection³⁸ or a compact einzel-lens deflector.³⁹ Furthermore, the setup is designed to be able to accommodate a probe holder for specimens, such as nano-tips. To align the gas jet, or any other target, to the fixed cavity focus, the whole system has to be motorized in three translational degrees of freedom.

C. Electron optics

For intra-cavity VMI operation, the distance between the curved focusing mirrors poses a strict limit on the spectrometer dimensions, which in our case is 125 mm. Additionally, compact

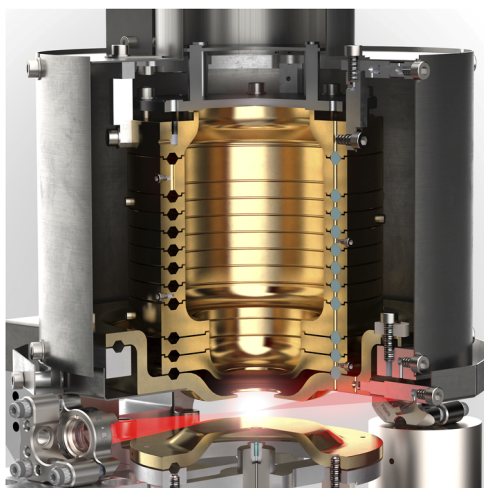


FIG. 2. Section through the VMI spectrometer showing the two concave cavity mirrors and the laser beam (red). A μ -metal (dark gray) shield surrounds the electrode stack (gold), shielding it from external electromagnetic fields.

XYZ-manipulators for ultra-high vacuum (UHV) conditions are limited to low loads. To achieve a low-weight setup, we designed a self-supporting electrode stack made from aluminum that is compact enough to fit between the cavity focusing mirrors.

The weight of the upper electrode stack, without connections, shielding, and detector is 0.65 kg; the weight of all moving parts is 2 kg and the weight of the whole assembly amounts to 3.5 kg. The maximum weight of the moving parts is limited by the 22 N load capacity of the vertical alignment actuator (Newport, 8301-UHV Picomotor). Linear translation stages (custom UHV compatible version of Newport 9062-COM-M) equipped with these actuators are integrated in the setup. Aluminum offers the advantage of a non-ferromagnetic, lightweight, and strong material, which is well machinable. The major disadvantage of aluminum is the formation of a nonconductive Al_2O_3 oxide layer, which leads to surface potentials.⁴⁰ This can be mitigated by gold plating the electrodes. For this, all electrodes are completely copper-electroplated with a thickness of 3 μm . Because of the high material price of gold, the electrodes are only silver- and gold-electroplated on the inside of the spectrometer with a layer thickness of 10 and 3.5 μm , respectively.

The inner diameter and height of the electrodes vary along the TOF axis, as shown in Figs. 2 and 3. The electrode dimensions of

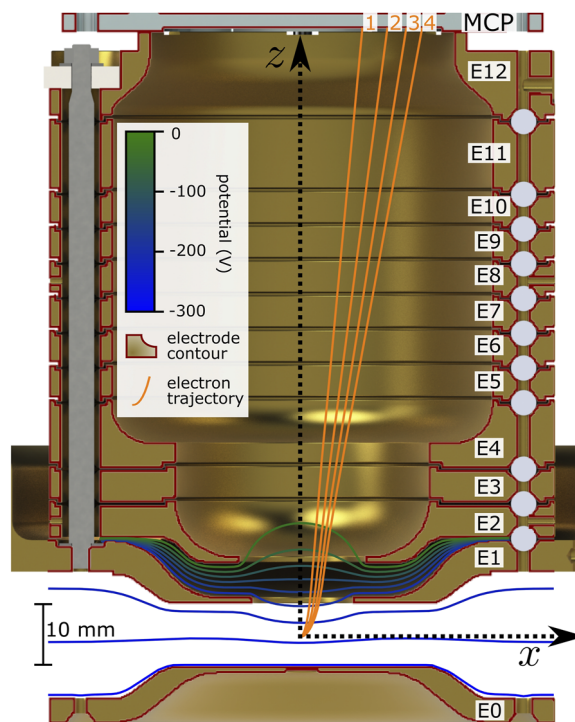


FIG. 3. Section view of the VMI electrode stack with overlaid exemplary electron trajectories. The electrode contours used in the simulations are drawn in dark red and trajectories of four electrons ionized in x direction with energies of 1, 2, 3, and 4 photon energies ($\hbar\omega \approx 1.2$ eV) are drawn in orange and labeled accordingly. Equipotential lines resulting from the applied voltages are indicated in green and blue color. The electrode number (E0 at -300 V, E1 at -221 V, and E2 to E12 at ground potential) and the MCP detector are labeled in black. The coordinate axes are drawn as dashed arrows with the interaction region as the origin.

the spectrometer are optimized with electron trajectory simulations. The repeller and extractor (E0 and E1) electrodes are spaced 10 mm apart to allow access for the focused, incoming and outgoing laser beams. The inner diameter of E1 is 16 mm, with a thickness of 1 mm and a distance of 6.5 mm to the ground electrode E2, which has an inner diameter of 20 mm, gradually increasing to 40 mm to match the size of E3 and E4. The inner diameter of E4 increases to 60 mm, which is the same as the inner diameter of E5 to E11. At E12, the inner diameter tapers to 48 mm, which is slightly larger than the 44 mm diameter of the active area of the MCP. The distance between E0 and the front plate of the MCP is 101 mm and the outer diameter of the electrode stack is 80 mm.

Ceramic spheres (Al_2O_3) are used to align and stack the electrodes, as visualized in Figs. 3 and 5(ii). V-shaped grooves are machined into the upper and lower surfaces of the electrodes on a lathe with high precision and reproducibility. Three spheres are inserted between two adjacent electrodes, touching on a point on both surfaces of the V-shaped grooves, thus defining the distance and orientation between the electrode pair. Alignment in angular direction is ensured by a hole drilled at each ball position. The holes are slightly oversized to allow for some play of the spheres in angular direction to avoid over-defining the assembly.

The electrode stack is held together by three titanium rods, which are screwed into the lower electrode (extractor electrode E1, as shown in Fig. 3). At the top, a ceramic insulator ensures that no electrical contact is made between the rod and the upper electrode (E12), while it is tensioned with a nut to press the whole electrode stack together. A creepage distance of 2.8 mm on the ball surface ensures a sufficient path length to allow for inter-electrode voltages of ~ 5 kV. Electrodes are shaped such that they overlap for shielding against stray electric fields. The nested structure of the cylindrical electrodes, with a minimum electrode–electrode distance of 0.5 mm, ensures that the line of sight from the inside of the spectrometer is shielded from the outside, the insulating balls, the tensioning rods, and the electrical connections. Simulations confirmed voltages outside the electrodes in the range of tens of kV do not influence the trajectories of low energy (≈ 1 eV) electrons significantly. All electrodes are connected by 1 mm diameter Kapton insulated copper wires, specified up to 10 kV, which are bundled and guided from the top of the assembly to SHV vacuum feedthroughs.

D. Electron trajectory simulations

The total experimentally realizable resolution of the system depends, besides the MCP pitch and pore size and the resolution of the data acquisition camera, on the geometry of the VMI setup itself. Non-ideal parallel projections inside the VMI spectrometer lead to larger spot sizes on the detector. We used SIMION (Version 8.1.3.9) to simulate electron trajectories during the design process of the VMI. The ionization region is set to be a sphere with variable radius. This sphere is centered on the spectrometer axis at half distance between the two lowest electrodes. The electrode contours used in the simulations as well as equipotential lines and exemplary electron trajectories are shown in Fig. 3. For these trajectories, we assume a maximum electron kinetic energy of four near-infrared photon energies (i.e., $E_{e, \text{max}} = 4.73$ eV; $v_{\text{max}} = 1290$ mm μs^{-1}) and a repeller voltage of $U_R = -300$ V. These are typical values for our MPI experiments.

For ideal parallel projections, all electrons with the same initial perpendicular velocity vector components v_x and v_y shall arrive at the same detector position irrespective of their parallel components v_z along the spectrometer axis. Therefore, the initial velocity distribution consists of 15 different groups with $N = 2000$ electrons each and discretely spaced v_x . We limit v_z to the maximum of $|v_x|$. It is sufficient to test the setup for a single value of $v_y = 0$, as the setup is rotationally symmetric around the spectrometer axis (i.e., $x = 0$, $y = 0$). This is a more realistic initial electron momentum distribution, shown in Fig. 4(b) in blue, compared to what was used in the early days of VMI,³ marked with red dots. It leads to a better estimation of the actual energy and momentum resolution of the VMI. At perfect focusing, we would expect 15 discrete spots for each group of v_x , but imperfections lead to scattering around the mean detector position $\langle x \rangle$, which is quantified by the standard deviation of the electron detector hit positions σ_x .

The repeller voltage U_R is selected such that the complete detector size is utilized for imaging. The optimal extractor to repeller voltage ratio is found to be $U_E/U_R = -221 \text{ V}/-300 \text{ V} = 0.738$, while variations of the voltage ratio of 1% result in a change of σ_x of only $1.5 \mu\text{m}$. We plot the detector image after propagation of the initial electron momentum distribution through the spectrometer in Fig. 4(a). The focus sizes in radial and azimuthal directions are quantified as σ_x and σ_y , respectively. The time of flight of the electron bunches from ionization until they hit the detector is 12.5 ns with a standard deviation of 0.4 ns. Figure 4(c) shows the resolution of the VMI as a function of the radial detector position. The radial spot size (in this case: σ_x) first increases for larger initial v_x , but then slowly decreases again, while the azimuthal spread (quantified by σ_y) is always better than the MCP resolution ($12 \mu\text{m}$ channel pitch). For the outermost bunch with maximum $|v_x|$, the spread of parallel components $|v_z|$ is minimal and thus, all particles arrive at the detector within a small spot.

To study the influence of the size of the interaction region on the VMI resolution, electron bunches starting with equal momentum but varying sizes of the spherical source are propagated. A source diameter of $50 \mu\text{m}$ is assumed for the results shown in Figs. 4(a)–4(c), which corresponds to twice the laser beam waist radius at the focus. Even though this is a reasonable estimate for the source size perpendicular to the laser beam propagation axis, it can be significantly larger along the axis. The energy resolution does not only depend on the source size but also on the radial detector position for a given U_R and U_E/U_R . This is taken into account for the determination of the relative energy resolution, shown in Fig. 4(d) for radial detector positions $r = 5, 10$, and 15 mm. For fixed electrode voltages, these positions correspond to energies of 1, 4, and 9 eV at a maximum detectable electron energy at the outer edge of the detector of ~ 20 eV, following the relation $r \propto \sqrt{E_e/U_R}$. We use the standard deviation σ_E to define the relative energy resolution σ_E/E , which is twice the value of the momentum resolution.

For our current laser parameters and assuming eleventh-order nonlinearities (I^{11}), the interaction volume can reach a length of up to ~ 1 mm. Under these conditions and without any assumption for the extent of the gas target, we expect an energy resolution of about $\sigma_E/E = 3\%$, limited mainly by the size along the laser beam propagation axis. The resolution could be significantly improved by shrinking the width of the gas jet (as discussed in Sec. II H) or by using counter-propagating pulses that collide at the focal point,

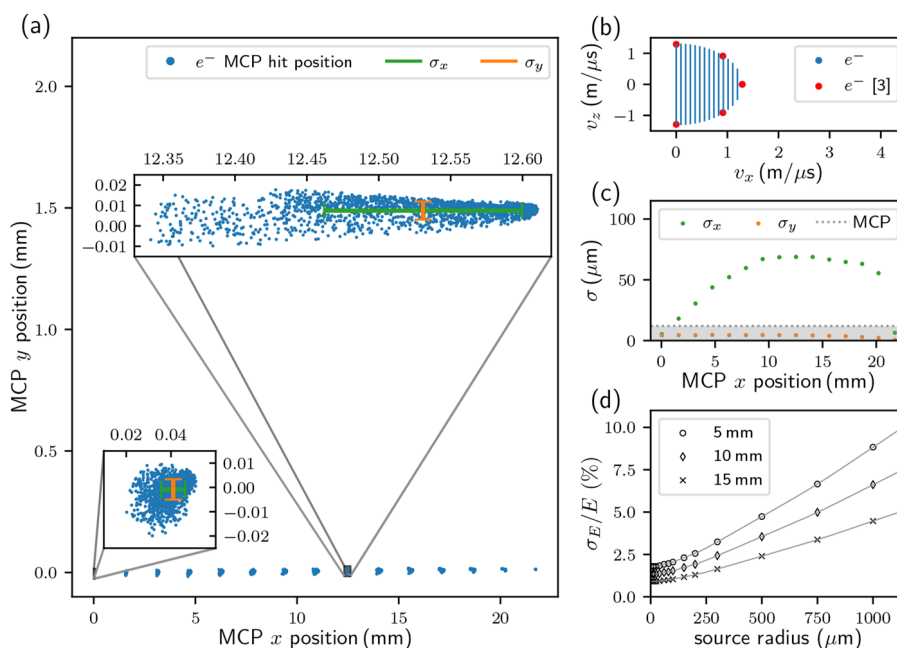


FIG. 4. SIMION performance simulations for the optimal voltage ratio of $U_E/U_R = 0.738$ of extractor and repeller electrode voltages to demonstrate the focusing capabilities of the VMI. (a) We characterize the focused size of the electrons on the MCP after propagation through the VMI by the standard deviations σ_x and σ_y . (b) Initial electron momentum distribution (blue) used for the simulations. In contrast to the first VMI design by Eppink and Parker,³ where discrete vertical velocities were used to determine the resolution, we utilized 15 groups with $v_y = 0$ and discretely spaced v_x , which are quasi-continuous in v_z . (c) The imaging quality of the VMI spectrometer is mainly determined by σ_x of the photoelectrons, while σ_y is always better than the MCP resolution, which is indicated by the gray shaded area. (d) The relative electron energy resolution σ_E/E depends on the source size and is shown for three radial detector positions. It is optimal for the outer parts of the detector and typically better than 2% for source radii below $100 \mu\text{m}$.

which would reduce the interaction volume to a sphere with a diameter of about $50 \mu\text{m}$ and improve the resolution to below 2%. A lower limit for the achievable resolution is the spectral bandwidth of the laser, which in our case is $\sim 1\%$. By increasing the repeller voltage to -5 kV at constant U_E/U_R , it is possible to image electrons with kinetic energies up to 105 eV without any noticeable change in (relative) energy resolution.

E. Magnetic shielding

For both providing magnetic and improving electrostatic shielding, a μ -metal (Aaronia MagnoShield DUR panel) shield with a thickness of 0.5 mm encloses the whole upper electrode stack. At the top, a cable guide and a tube surrounding the MCP detector both of which are made of μ -metal protrude into the vacuum chamber to keep magnetic fields away from the VMI interior. To restore the high permeability of the μ -metal shielding after machining and welding, all parts were annealed in vacuum at 1050°C for three hours and then slowly cooled down to room temperature over the course of ten hours. The magnetic shielding performance is experimentally evaluated by placing a strong permanent magnet in close vicinity to the setup and measuring the magnetic field at the center point of the assembly with and without the μ -metal enclosure. The annealed μ -metal shield reduced the magnetic field inside the VMI by a factor of ~ 270 . The annealing process improved the shielding by a factor of 15 compared to the shielding performance directly after machining.

F. Fabrication and preparation of the parts

All machined parts are fabricated in-house on CNC machining centers and most parts, including the electrodes, are within RZ 16 surface roughness tolerances. After electroplating (Drollinger Metall-veredelungswerke), the electrodes are cleaned in a heated ultrasonic bath in citric acid to remove the oxidation layer from the copper. Then, the electrodes are treated in an ultrasonic bath with another cleaning solution followed by de-ionized water and a final rinse with ethanol. After dry blowing them with nitrogen, they are heated in an oven to dry completely.

All other UHV components, except the translation stages and the detector, are prepared following a standard procedure in the ultrasonic bath with cleaning solution, a second rinse in de-ionized water, dry blowing, and baking at 200°C for a few hours before assembly.

G. Imaging electron and ion detector

An MCP detector in Chevron configuration (TOPAG, MCPD-50-C-P), equipped with a P43 phosphor screen, is used for electron/ion detection. The active area has a diameter of 44 mm with a channel diameter and pitch of 10 and $12 \mu\text{m}$, respectively. The front plate of the metallic detector frame is conductively mounted directly on the uppermost electrode. This avoids any non-conducting or high voltage parts in line of sight to the inside of the VMI setup causing image distortions. The fluorescent phosphor screen is imaged

through a vacuum window with an air-side camera (Allied Vision, Mako G-234B mono), and the raw images are stored on a computer for further analysis. A photograph of the assembled VMI spectrometer, before installing the electrical connections, the MCP detector and the shielding, is depicted in Fig. 5.

H. Gas target for VMI studies

The VMI spectrometer is mounted together with the cavity optics inside a large UHV chamber ($2.1 \times 0.6 \times 0.4 \text{ m}^3$). A 2100 L s^{-1}

magnetically levitated turbomolecular pump on the top of it generates a vacuum of $8 \times 10^{-8} \text{ mbar}$ without bake-out and $7 \times 10^{-6} \text{ mbar}$ during gas injection, which corresponds to the maximum pressure the MCP detector can be operated at without damage. The pressure is measured with a vacuum gauge located 0.5 m away from the pump inlet.

The repeller electrode (E0) has a hole with a diameter of $b = 100 \mu\text{m}$ drilled through in the center [see Fig. 5(i)]. A gas nozzle with an opening diameter of $50 \mu\text{m}$ is placed $d = 4 \text{ mm}$ below the electrode. Axial alignment of the nozzle is ensured up

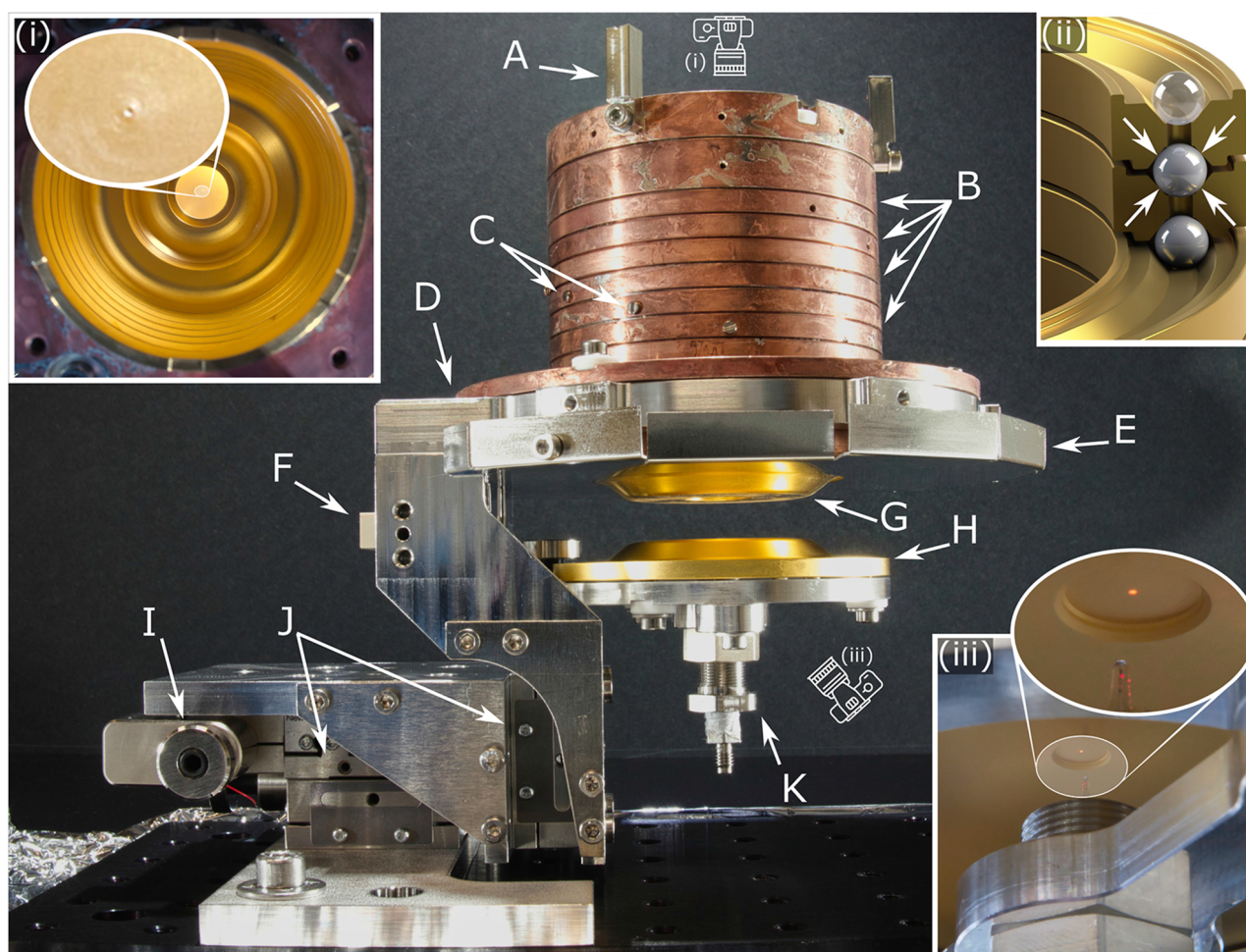


FIG. 5. Photograph of the VMI setup stripped of MCP, gas supply, electrical connections and the upper part of the μ -metal shielding, viewed in the direction of laser propagation. (A) holder for the μ -metal shielding, (B) electrode stack, (C) screws for electrical connection, (D) mounting brace of the electrode stack and upper part of extractor electrode E1, (E) lower part of μ -metal shielding attached to the extractor electrode, (F) PEEK mounting adapter for the nano-tip holder (not shown), (G) lower part of the extractor electrode, (H) repeller electrode E0, (I) piezo motor, (J) translation stages for XYZ-movement, and (K) nozzle holder with gas connector. (i) Top view with zoomed inset of the lowest electrode (repeller) with a $100 \mu\text{m}$ diameter hole, from where the gas, injected by a $50 \mu\text{m}$ diameter nozzle 4 mm below the electrode, enters the target region. (ii) Detailed view of the electrodes and ceramic spheres used as spacers. They rest on V-shaped grooves on the electrodes, as marked by the white arrows. Vertical bores restrain the motion of each of the three balls between each electrode pair but do not over-define the assembly. Overlapping of the electrodes enhances electrostatic shielding. The upper sphere is shown translucently for clarity. (iii) View from below the lowest electrode (repeller E0) with the gas nozzle pointing upward. A red laser pointer pointing downward along the spectrometer axis from above the electrode stack illuminates the nozzle tip during the alignment procedure. A zoomed inset shows the nozzle and the hole in more detail. For drilling the $100 \mu\text{m}$ hole, material was removed from the bottom side such that the residual electrode material is thin enough for the drill bit.

n assembly by a red laser pointing downward, illuminating the nozzle tip through the hole in the electrode, as shown in Fig. 5(iii). This procedure ensures that as much gas as possible from the vertical gas jet is passing through the hole in the electrode. The pressure in the chamber assures operation in the free molecular flow regime, implying that the small hole effectively serves as a skimmer to collimate the expanding gas cloud. The terminal velocity of the gas injected by the gas nozzle into the chamber can be calculated by⁴¹

$$v_{\infty} = \sqrt{\frac{2R}{W} \left(\frac{\gamma}{\gamma-1} \right) (T_0 - T)}, \quad (1)$$

where R is the molar gas constant, W is the atomic weight, and $\gamma = (f + 2)/f$, where f is the number of degrees of freedom of the molecular motion (i.e., $\gamma = 5/3$ for monoatomic gases). T_0 is the initial temperature before expansion and T is the temperature after expansion, in our case approximated by $T \approx 0$. For xenon gas expanding from room temperature, this corresponds to a maximum terminal velocity of $\sim 300 \text{ m s}^{-1}$. The Doppler width of a transition in a gas jet atom moving with velocity v is given by

$$\Delta\omega_{\text{D}}(\text{FWHM}) = 2\omega_0(v/c)\sqrt{\ln 2}, \quad (2)$$

for a transition angular center frequency ω_0 and the speed of light c . The collimation of the gas jet by the electrode hole leads to a reduction of Doppler broadening at our central wavelength of 1039 nm from ~ 500 to 6 MHz for xenon because the Doppler width scales according to the collimation factor⁴² $b/(2d) = 0.0125$. Provided that a sufficiently narrow transition of a gas jet atom is covered by our laser spectrum, we could resolve it by direct frequency comb spectroscopy⁴³ with a 100 MHz comb tooth spacing. However, we have not yet experimentally measured the target gas velocity and collimation. Even though we operate the whole system in the free molecular flow regime, a higher local pressure below the repeller electrode might lead to backscattering. To investigate if this is the case, we plan to assess the quality of the gas sample using ion spatial imaging.

It is possible to increase the target density at the cost of sacrificing the reduction in Doppler width, by exchanging the repeller electrode with an electrode with an integrated gas nozzle.³⁸

I. Detection of metastable states excited by multi-photon excitation of neutral atoms

In addition to ions and electrons, MCPs can also detect neutral metastable atoms.⁴⁴ For that, high voltages can be applied to VMI electrodes and the MCP front plate to push unwanted electrons and ions away from the MCP detector and let only neutral atoms pass. If these neutral metastable atoms collide with the surface of a solid, they can eject electrons if their energy is high enough to surpass the work function of the material.⁴⁵ The released electrons are then registered by the MCP.

J. Sample holder for nano-tips

A sample holder (see Fig. 6) can be moved into the focus of the cavity. In this way, we can use the local field enhancement of a nano-tip for studies of multi-photon electron emission⁴⁶ or use the tip as a laser field probe of standing waves in the cavity focus. In a first

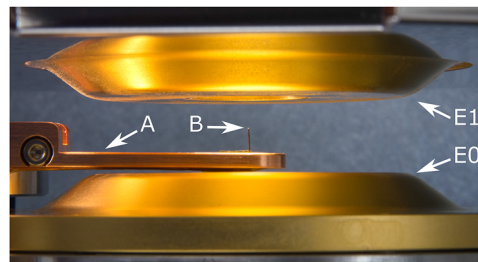


FIG. 6. Photograph of the VMI setup with a nano-tip inserted between the repeller (E0) and extractor (E1) electrode. Both the copper tip holder (A) and the tungsten nano-tip (B) can be biased independently.

test, photoelectron emission was detected for several hours without damaging the tip. Currently, we are upgrading the design in order to fulfill the VMI conditions.⁴⁷

K. Reconstruction of 3D PADs

When applying the VMI technique, the original 3D PADs are imaged on the 2D detector plane, mapping the initial particle velocity distribution to the arrival position. Reconstruction of the initial 3D distribution can be performed from the 2D data by Abel inversion if the 3D image possesses cylindrical symmetry with the symmetry axis aligned parallel to the detector plane.^{48–50} Thus, this method works well provided that the laser light is linearly polarized. For Abel inversion, we use the PyAbel Python software package.⁵¹

It has been demonstrated that it is also feasible to directly slice the photoion^{3,52} and photoelectron^{25,53} clouds by application of a short-time gate pulse to the detector, the camera, or even directly recording time-resolved images.^{27,54} Even though these methods are promising, they are not suited for high repetition rates. This is because the expansion of the photoelectron/ion sphere typically takes place within several hundred nanoseconds in these schemes, which is much longer than the 10 ns repetition time of our system.

Alternatively, tomographic reconstruction allows retrieval of 3D PADs from photoionization of atoms^{18,55,56} and molecules,^{57,58} also for non-cylindrically symmetric distributions. As a result, 3D free-electron wave-packet distributions generated by polarization-shaped ultrashort laser pulses can be retrieved regardless of any symmetry assumption.^{19,21} In our case, tomographic reconstruction of the 3D distributions from the projected 2D detector images by the filtered back-projection method is implemented based on the iradon Python package.⁵⁹ Even though this method is very reliable, it was recently demonstrated that more advanced tomographic reconstruction methods provide better performance.⁶⁰ In Fig. 1, the complete experimental cycle including data acquisition and tomographic reconstruction is illustrated schematically (with the data from Sec. III B).

The Nyquist–Shannon sampling theorem and earlier SIMION simulations suggest that the number of recorded angles should be similar to the number of x and y pixels.⁶¹ Experimentally, we rotate the polarization using an AR-coated zero-order half-wave plate (B. Halle Nachfl. GmbH) mounted in a motorized rotation mount (Thorlabs, PRM1/MZ8) in steps of 1° between 0° and 89° , which corresponds to a polarization rotation step size of $\theta = 2^\circ$. This is

sufficient because after a polarization change of 180° , the initial polarization is restored, and the electric field is essentially the same. It should be mentioned that this might not necessarily be the case for few-cycle pulses with stabilized carrier-envelope phase (CEP). In the case of electron photoemission from metallic nanostructures, CEP effects become important^{62,63} and require a 360° polarization rotation to restore the initial electric field. Even though we typically lock the CEP of our frequency comb to 20 MHz, these CEP effects are not a concern for the 50-cycle pulses of our laser.

III. A TEST CASE: MPI OF XENON

In a first experiment, we use our compact VMI system for intra-cavity photoionization of xenon to demonstrate the performance under real experimental conditions. For technical reasons, we had to operate the enhancement cavity in scan mode, which means the cavity length is scanned over the resonance, where maximum enhancement is achieved. Compared to continuous resonant operation, this reduces the time the cavity is actually resonant and photoelectrons are emitted. The cavity was scanned at a frequency of 460 Hz across the resonance, resulting in an effective duty cycle of 2.3%. This fraction of time corresponds to 99.6% of the total photoelectron yield. The maximum intra-cavity peak intensity in the focus region is calculated from the measured temporal pulse shape, the focus size, and the photodiode signal of the leakage through one of the cavity mirrors. At cavity resonance, xenon atoms are ionized above threshold in the cavity focus.

When xenon is ionized from the outer orbital, the generated Xe^+ can be either in the ground state $\text{Xe}^+(^2P_{3/2})$ with $I_p = 12.13$ eV or in the first excited state $\text{Xe}^+(^2P_{1/2})$ with $I_p = 13.44$ eV. Ionization to the latter is very unlikely for our laser wavelength.⁶⁴ The energy of the photoelectrons at a given laser intensity after absorption of n photons is given by $E_e = n\hbar\omega - (I_p + U_p)$, where I_p is the ionization potential of the atom and $U_p = e^2 E_0^2 / (4m_e \omega^2)$ is the ponderomotive energy shift induced by the electric field E_0 of the laser, with the electron charge e and mass m_e . In the short-pulse

regime, not only does the ionization threshold shift ponderomotively but—due to the AC Stark effect—also Rydberg states shift and can be resonantly excited. This results in features in the electron energy spectrum, known as Freeman resonances, often reflecting the characteristics of the intermediate states.^{65,66} In Fig. 8(c), energy levels of xenon, accessible from the $^1S_05p^6$ ground state, are depicted.⁶⁷ These Rydberg states shift approximately with the ponderomotive energy because they are close to the ionization threshold. The energies reachable by absorption of nine to twelve photons are indicated as red horizontal features with the thickness representing the spectral bandwidth. We assume a negligible influence of the laser field on the ground state.

A. Angular integrated photoelectron spectrum

Starting at relatively low intensities, the simultaneous absorption of 11 near-infrared photons is sufficient to overcome the ionization potential of xenon. At intensities above $1 \times 10^{13} \text{ W cm}^{-2}$, the combined energy of 11 photons is not sufficient anymore and 12 photons become necessary (channel switching/closing^{68–71}). MPI of xenon at a laser peak intensity of $\sim 1.5 \times 10^{13} \text{ W cm}^{-2}$ is shown in Fig. 7. At this intensity, 11 photons are resonant with the xenon $5p^5(^2P_{3/2})5g$ state and absorption of an additional photon leads to the first ATI ring. The laser polarization is set parallel to the detector and photoelectrons are imaged onto the MCP detector and recorded with the camera. 74 raw images with an exposure time of 5 s are dark-frame corrected and hot pixels are removed. Then, the images are overlaid with a vertically mirrored copy of themselves since the sensitivity of the MCP detector unfortunately changes from the upper to the lower half of the image, causing one-half of the raw images to appear darker. From the raw images, we estimate that the circularity differs from perfect circles only on the sub-percent level and no circularization or other more advanced image processing steps are needed. The sum of the dark-frame corrected original images as well as the central slice after Abel inversion are depicted in Fig. 7(a). A clear angular structure with five nodes is visible as well as sharp features in the radial direction.

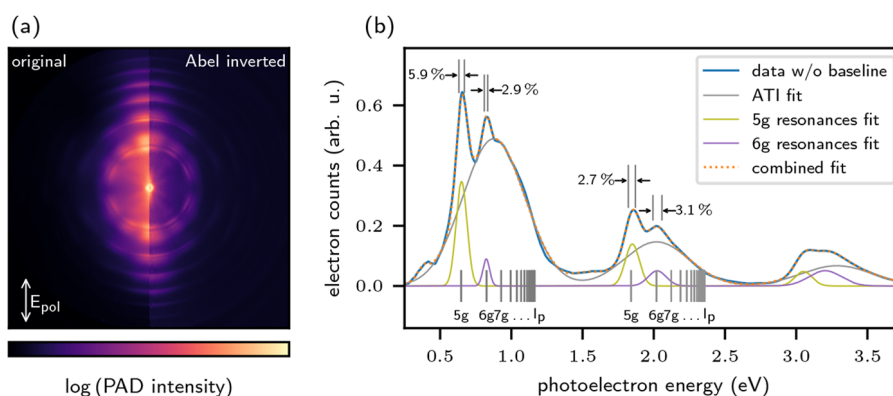


FIG. 7. (a) Detector image of the VMI spectrometer showing a 2D projection of photoelectrons from xenon MPI before (left half) and after (right half) Abel inversion. At a laser intensity of $\sim 1.5 \times 10^{13} \text{ W cm}^{-2}$, the $5p^5(^2P_{3/2})5g$ resonance can be reached by 11 photons and absorption of an additional photon leads to the first ATI ring. (b) Section of the photoelectron energy spectrum retrieved from the Abel-inverted image by angular integration. Resonances are fitted as described in the text. The most prominent features originating from the 5g and 6g resonances are drawn separately for illustration and their relative energy widths are given.

Angular integration of the Abel image yields the photoelectron momentum distribution. The detector is calibrated by fitting the ATI peak positions to a quadratic function assuming zero momentum in the center and an $\hbar\omega$ energy spacing of the rings, yielding the momentum and energy scale as a function of radial detector position. In Fig. 7(b), we show the photoelectron energy spectrum, corrected by an exponential baseline, as well as the expected $5p^5(^2P_{3/2})ng$ level positions for the first and second ATI peak. The electron spectrum is fitted with a model composed of Gaussians accounting for the well-resolved resonances added on top of larger Gaussians, which take the overall structure of the ATI peaks, consisting of poorly separated narrow features and nonresonant contributions, into account. The fits of the most prominent features originating from the $5g$ and $6g$ resonances are drawn separately for illustration. Faint peaks at ~ 0.4 and 1.6 eV are expected to come from the nine-photon resonant $5p^5(^2P_{3/2})5d$ -state at lower intensity levels and are included in the fit model. Standard deviations of the $5g$ and $6g$ resonances are extracted and their relative values σ_E/E are stated. These values are considered to be a reasonable estimate of the actual energy resolution reached in the experiment. It means that the relative energy resolution of the VMI spectrometer is in the range of about 3%. This value is in good agreement with the simulations presented in Sec. II D and represents a significant improvement in comparison to our previous

setup²⁹ for which we estimate an energy resolution of not better than 10%.

Note that in some other works, the relative energy resolution is given as the ratio of total energy and FWHM, while we use the standard deviation of the Gaussian distribution fit instead.^{3,32–34,37} Currently, the resolution of our compact spectrometer is about ten times lower than that of larger, established instruments.^{32,37} However, we can implement a well-collimated supersonic gas jet in the horizontal plane to shorten the length of the interaction region to improve it. We are also currently testing colliding-pulse operation, in which two counter-propagating beams meet at the cavity focus. Given the 184 fs pulse duration and the nonlinearity of the multi-photon processes, this reduces the effective target length in the propagation direction to a value similar to the beam waist.

B. Tomographic reconstruction of PADs at low laser intensity

To demonstrate the feasibility to perform photoelectron tomography even at relatively low intensities, we detect photoelectrons at an intra-cavity peak intensity of $7.7 \times 10^{12} \text{ W cm}^{-2}$. Photoelectrons are imaged on the MCP detector for each polarization angle θ , as described earlier and schematically shown in Fig. 1. Camera images are taken with an exposure time of 10 s and

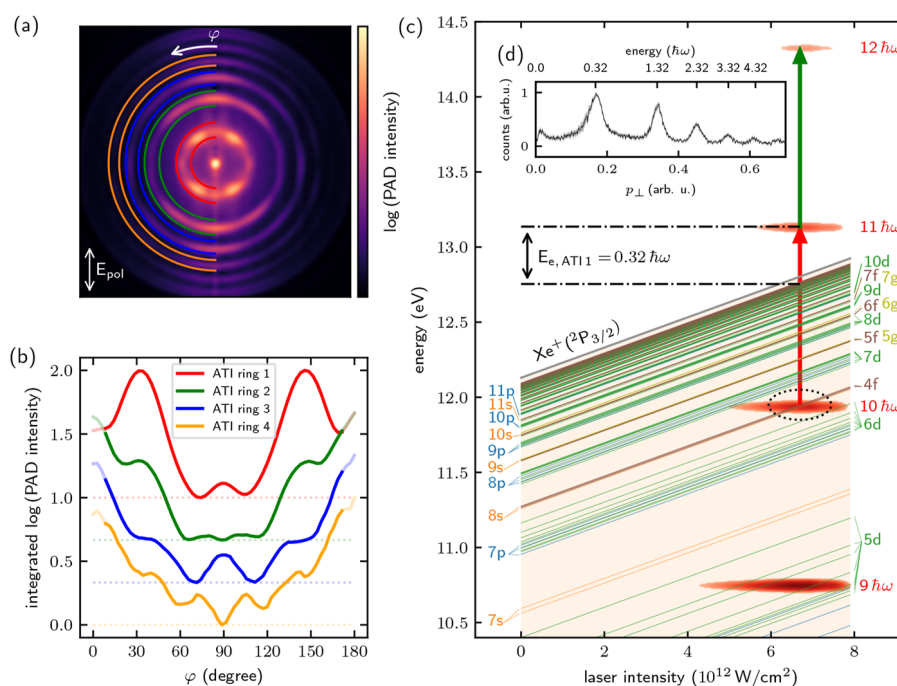


FIG. 8. (a) 2D projection of tomographically reconstructed 3D PADs from MPI of xenon, by azimuthal integration around the polarization symmetry axis (vertical). Integrated photoelectron yields of the first four of total six ATI rings found within the color-coded semicircles are shown in (b) as a function of the polar angle φ with an offset for clarity. (c) Rydberg states of xenon shift ponderomotively in the laser field and can become resonant by simultaneous absorption of n photons. Red features labeled with $n\hbar\omega$ illustrate the likelihood of an n -photon absorption process in a logarithmic colormap, using the laser intensity distribution and photon multiples of the fundamental spectrum, weighted by the photon number. The most likely resonant $5p^5(^2P_{3/2})4f$ state can be reached by ten photons and is marked by a dotted ellipse. From this state, photoionization by absorption of a photon (red arrow) leads to the first ATI ring and an additional photon (green arrow) causes the second ring and so on. From the photoelectron momentum distribution, shown in inset (d), the mean kinetic electron energy $E_{e,ATI1}$ of the first ATI ring is extracted and marked by dashed-dotted lines.

corrected as described before. These images are averaged for each angle and reduced in size to 128×128 pixel², the next higher power of two compared to the number of recorded polarization angles. Then, they are stacked together into a single array and slices of this array (the sinograms) are extracted for each y -pixel.

Tomographic reconstruction of each sinogram is performed using the filtered back-projection method. After reconstruction, the images are combined to a 3D array and the 3D PAD can be visualized in different ways, either as a maximum intensity projection plot, as shown in Fig. 1(g), or as an isosurface plot, as shown in Fig. 1(h). In both representations, ATI rings (i.e., 3D shells) are clearly visible and in the latter, an isosurface for each shell is identified and drawn in a different color (in rising order: gray, red, green, blue, yellow, purple, cyan). Note that some details of the angular structure are lost due to the isosurface representation, but the overall structure with the shells spaced by the photon energy is clearly visualized.

Azimuthal integration of the reconstructed PAD around the polarization symmetry axis [vertical axis in Fig. 8(a)] yields a single half-image. This half-image is mirrored horizontally, which gives a result similar to the central slice after Abel inversion but retrieved by tomography instead. To indicate the ranges used for radial integration, colored semicircles are drawn on top of the left side of the image in Fig. 8(a), with the same color code of the ATI rings as before. These angular distributions of the inner rings are plotted with a vertical offset for clarity as a function of the polar angle φ in Fig. 8(b), disregarding the outer 10° due to the vertical artifact in the center of the retrieved image.

A clear angular structure is visible in the angular distribution and the signal is not mainly oriented in the laser polarization direction, which hints toward resonant ionization.⁷² From the maxima and minima of the PADs, it is noticeable that the total angular momentum change Δl switches between odd and even values for consecutive rings. The first ATI ring (red) shows four nodes, indicating contributions of partial waves of $l = 4$, suggesting that the electrons originate from an f state, most likely from $5p^5(^2P_{3/2})4f$, from where absorption of a single photon [indicated by the red arrow in Fig. 8(c)] is sufficient to overcome the ionization potential of $\text{Xe}^+(^2P_{3/2})$. This resonance can be reached by absorbing ten photons from the $5p^6$ ground state at an intensity of 6.8×10^{12} W cm⁻² with a total angular momentum change of ($\Delta l = 2$). Even though the $5p^5(^2P_{3/2})8s$ state would be resonant at the same intensity, the required $\Delta l = 1$ cannot be reached by an even number of photons. At lower intensities ($\sim 4.5 \times 10^{12}$ W cm⁻²), the resonances $5p^5(^2P_{3/2})7d$ and $8p$ are excluded due to a mismatch of the measured photoelectron energy of $0.32\hbar\omega$. It is obtained by angular integration of all Abel-inverted raw images, where the polarization is parallel to the detector and shown in Fig. 8(d). The nine-photon resonance $5p^5(^2P_{3/2})5d$ could also be excited at slightly higher or lower intensity levels. The second ring (green) exhibits five nodes ($l = 5$) pointing toward ionization with two photons from the same state. As the first ring, the third ATI ring (blue) shows four nodes, indicating ionization with three photons from the same $5p^5(^2P_{3/2})4f$ state but with the Δl of the two additional photons canceling each other. The fourth ring (orange) has an additional node compared to the third ring as expected. The resonant $4f$ state mentioned in the discussion above is marked by a dotted ellipse in Fig. 8(c). Since the xenon exhibits many resonances at the tenth harmonic of our laser

frequency, contributions of other (non)resonant ionization pathways cannot be fully excluded.

Due to the operation in scan mode, intensities from zero up to the maximum intensity contribute to the ionization process and the recorded images average over all of these electrons. Therefore, it can be indeed possible to record photoelectrons on the inner rings that also come from ionization at rather low intensities. For the outer rings, these low-intensity pathways are more strongly suppressed because of the higher photon number. At lower laser intensities, higher-lying Rydberg states shift into resonance, but ionization is much less probable, because the ionization rate scales with I^n , with n being the number of required photons. We account for this highly nonlinear intensity scaling in the graphic representation of Fig. 8(c) by weighting the laser spectrum of each photon multiple with the measured laser intensity distribution to the power of the respective photon number. For better clarity, it is drawn in a logarithmic colormap.

Even with the limitation of operating the cavity in scan mode, the electron count rate is in the range of a few kHz and the recording of the complete dataset for tomography took about 12 h. In the future, we will lock the cavity length to the repetition rate of the driving frequency comb for continuous high intensity operation.

Additionally, a repeller electrode with an integrated gas nozzle would increase the target density, and thus the count rate, by orders of magnitude as described before in Sec. II H. As already demonstrated in our previous work,²⁹ we would then expect count rates in the range of a few MHz and exposure times of single images well below 1 s.

IV. CONCLUSION

We have demonstrated a compact velocity-map imaging spectrometer for intra-cavity multi-photon ionization studies with tomographic reconstruction of 3D PADs. The tomographic measurements are analyzed using an algorithm that does not require an inverse Abel or other transformation, which allows reconstruction of non-cylindrically symmetric distributions. We demonstrated the functionality of the setup with multi-photon ionization of xenon and obtained a relative energy resolution of $\sim 3\%$ by resolving sharp resonance features from Abel-inverted images.

The present setup uses a lightweight, self-supporting structure of nested, individually addressable gold-coated aluminum electrodes isolated and aligned by ceramic balls. It can optionally accommodate a holder for a nano-tip to study strong-field nano-optics. We plan to utilize the local field enhancement to excite the ^{229m}Th nuclear isomeric state of thorium atoms deposited on a tip by multi-photon-generated plasmons. This transition is promising for future highly accurate nuclear clock operation.^{73–75} To cover the current uncertainty range of the thorium transition, we will broaden the laser spectrum nonlinearly in a multi-pass cell.⁷⁶

At the high repetition rate of 100 MHz, our setup enables MPI studies at low intensities that are out of reach for conventional laser systems. In addition, the coherence of the near-infrared frequency comb is imprinted on the photoelectrons by virtue of the resonant enhancement cavity and the setup thus serves as a coherent electron source. Currently, we are working on a setup to feed pulses into both propagation directions of the ring cavity to generate standing waves from counter-propagating pulses colliding in the focus.

ACKNOWLEDGMENTS

We thank the MPIK engineering design office headed by Frank Müller and the MPIK mechanical workshops under the direction of Thorsten Spranz for their expertise and fabrication of numerous parts. Additionally, we want to highlight the help of Yannick Steinhauser during the design process and thank him for his support with image rendering. This work was funded by the Max-Planck-Gesellschaft, the Max-Planck-RIKEN-PTB-Center for Time, Constants and Fundamental Symmetries and the Collaborative Research Center SFB 1225 (Isoquant). This work has been funded by the “European Metrology Program for Innovation and Research” (EMPIR) project 20FUN01 TSCAC. This project has received funding from the EMPIR programme co-financed by the participating states and from the European Union’s Horizon 2020 research and innovation programme.

AUTHOR DECLARATIONS

Conflict of Interest

The authors have no conflicts to disclose.

Author Contributions

J.-H. Oelmann: Conceptualization (lead); Formal analysis (lead); Investigation (lead); Methodology (lead); Project administration (lead); Software (equal); Supervision (lead); Visualization (lead); Writing – original draft (lead); Writing – review & editing (lead). **T. Heldt:** Formal analysis (equal); Investigation (equal); Methodology (equal); Software (lead); Visualization (equal); Writing – review & editing (equal). **L. Guth:** Investigation (supporting); Software (supporting); Writing – review & editing (equal). **J. Nauta:** Conceptualization (supporting); Investigation (supporting); Methodology (equal); Software (equal); Visualization (equal); Writing – review & editing (equal). **N. Lackmann:** Investigation (supporting); Writing – review & editing (supporting). **V. Wössner:** Formal analysis (supporting); Investigation (supporting); Methodology (equal); Software (equal); Visualization (equal); Writing – review & editing (supporting). **S. Kokh:** Formal analysis (supporting); Software (equal); Writing – review & editing (supporting). **T. Pfeifer:** Conceptualization (lead); Funding acquisition (lead); Project administration (equal); Supervision (equal); Writing – review & editing (equal). **J. R. Crespo López-Urrutia:** Conceptualization (lead); Funding acquisition (equal); Project administration (equal); Supervision (lead); Writing – review & editing (equal).

DATA AVAILABILITY

The data that support the findings of this study are available from the corresponding author upon reasonable request.

REFERENCES

- 1 B. J. Whitaker, *Imaging in Molecular Dynamics: Technology and Applications* (Cambridge University Press, 2003).
- 2 D. Townsend, M. P. Minitti, and A. G. Suits, *Rev. Sci. Instrum.* **74**, 2530 (2003).
- 3 A. T. J. B. Eppink and D. H. Parker, *Rev. Sci. Instrum.* **68**, 3477 (1997).
- 4 D. A. Horke, G. M. Roberts, J. Lecointre, and J. R. R. Verlet, *Rev. Sci. Instrum.* **83**, 063101 (2012).
- 5 Y. Huisman, A. Rouzee, A. Gijbbersen, J. H. Jungmann, A. S. Smolkowska, P. S. W. M. Logman, F. Lepine, C. Cauchy, S. Zamith, T. Marchenko, J. M. Bakker, G. Berden, B. Redlich, A. F. G. van der Meer, H. G. Muller, W. Vermin, K. J. Schafer, M. Spanner, M. Y. Ivanov, O. Smirnova, D. Bauer, S. V. Popruzhenko, and M. J. J. Vrakking, *Science* **331**, 61 (2010).
- 6 S. Zherebtsov, T. Fennel, J. Plenge, E. Antonsson, I. Znakovskaya, A. Wirth, O. Herrwerth, F. Süßmann, C. Peltz, I. Ahmad, S. A. Trushin, V. Pervak, S. Karsch, M. J. J. Vrakking, B. Langer, C. Graf, M. I. Stockman, F. Krausz, E. Rühl, and M. F. Kling, *Nat. Phys.* **7**, 656 (2011).
- 7 D. W. Chandler and P. L. Houston, *J. Chem. Phys.* **87**, 1445 (1987).
- 8 P. Agostini, F. Fabre, G. Mainfray, G. Petite, and N. K. Rahman, *Phys. Rev. Lett.* **42**, 1127 (1979).
- 9 D. H. Parker and A. T. J. B. Eppink, *J. Chem. Phys.* **107**, 2357 (1997).
- 10 M. N. R. Ashfold, N. H. Nahler, A. J. Orr-Ewing, O. P. J. Vieuxmaire, R. L. Toomes, T. N. Kitsopoulos, I. A. Garcia, D. A. Chestakov, S.-M. Wu, and D. H. Parker, *Phys. Chem. Chem. Phys.* **8**, 26 (2006).
- 11 K. T. Lorenz, D. W. Chandler, J. W. Barr, W. Chen, G. L. Barnes, and J. I. Cline, *Science* **293**, 2063 (2001).
- 12 D. M. Neumark, *J. Phys. Chem. A* **112**, 13287 (2008).
- 13 M. Nisoli, P. Decleva, F. Calegari, A. Palacios, and F. Martín, *Chem. Rev.* **117**, 10760 (2017).
- 14 T. Remetter, P. Johnsson, J. Mauritsson, K. Varjú, Y. Ni, F. Lépine, E. Gustafsson, M. Kling, J. Khan, R. López-Martens, K. J. Schafer, M. J. J. Vrakking, and A. L’Huillier, *Nat. Phys.* **2**, 323 (2006).
- 15 J. Mauritsson, P. Johnsson, E. Mansten, M. Swoboda, T. Ruchon, A. L’Huillier, and K. J. Schafer, *Phys. Rev. Lett.* **100**, 073003 (2008).
- 16 G. Sansone, F. Kelkensberg, J. F. Pérez-Torres, F. Morales, M. F. Kling, W. Siu, O. Ghafur, P. Johnsson, M. Swoboda, E. Benedetti, F. Ferrari, F. Lépine, J. L. Sanz-Vicario, S. Zherebtsov, I. Znakovskaya, A. L’Huillier, M. Y. Ivanov, M. Nisoli, F. Martín, and M. J. J. Vrakking, *Nature* **465**, 763 (2010).
- 17 D. M. Villeneuve, P. Peng, and H. Niikura, *Phys. Rev. A* **104**, 053526 (2021).
- 18 M. Weger, J. Maurer, A. Ludwig, L. Gallmann, and U. Keller, *Opt. Express* **21**, 21981 (2013).
- 19 D. Pengel, S. Kerbstadt, L. Englert, T. Bayer, and M. Wollenhaupt, *Phys. Rev. A* **96**, 043426 (2017).
- 20 D. Pengel, S. Kerbstadt, D. Johannmeyer, L. Englert, T. Bayer, and M. Wollenhaupt, *Phys. Rev. Lett.* **118**, 053003 (2017).
- 21 S. Kerbstadt, K. Eickhoff, T. Bayer, and M. Wollenhaupt, *Nat. Commun.* **10**, 658 (2019).
- 22 R. Dörner, V. Mergel, O. Jagutzki, L. Spielberger, J. Ullrich, R. Moshhammer, and H. Schmidt-Böcking, *Phys. Rep.* **330**, 95 (2000).
- 23 J. Ullrich, R. Moshhammer, A. Dorn, R. Dörner, L. P. H. Schmidt, and H. Schmidt-Böcking, *Rep. Prog. Phys.* **66**, 1463 (2003).
- 24 D. Rolles, Z. D. Pešić, M. Perri, R. C. Bilodeau, G. D. Ackerman, B. S. Rude, A. L. D. Kilcoyne, J. D. Bozek, and N. Berrah, *Nucl. Instrum. Methods Phys. Res., Sect. B* **261**, 170 (2007).
- 25 A. Vredenborg, W. G. Roeterdink, and M. H. M. Janssen, *Rev. Sci. Instrum.* **79**, 063108 (2008).
- 26 C. S. Lehmann, N. B. Ram, and M. H. M. Janssen, *Rev. Sci. Instrum.* **83**, 093103 (2012).
- 27 A. Zhao, M. van Beuzekom, B. Bouwens, D. Byelov, I. Chakaberia, C. Cheng, E. Maddox, A. Nomerotski, P. Svirha, J. Visser, V. Vrba, and T. Weinacht, *Rev. Sci. Instrum.* **88**, 113104 (2017).
- 28 A. Zhao, P. Sándor, and T. Weinacht, *J. Chem. Phys.* **147**, 013922 (2017).
- 29 J. Nauta, J.-H. Oelmann, A. Ackermann, P. Knauer, R. Pappenberger, A. Borodin, I. S. Muhammad, H. Ledwa, T. Pfeifer, and J. R. C. López-Urrutia, *Opt. Lett.* **45**, 2156 (2020).
- 30 R. Trebino, R. Jafari, S. A. Akturk, P. Bowlan, Z. Guang, P. Zhu, E. Escoto, and G. Steinmeyer, *J. Appl. Phys.* **128**, 171103 (2020).
- 31 J. Nauta, J.-H. Oelmann, A. Borodin, A. Ackermann, P. Knauer, I. S. Muhammad, R. Pappenberger, T. Pfeifer, and J. R. C. López-Urrutia, *Opt. Express* **29**, 2624 (2021).

- ³²I. León, Z. Yang, H.-T. Liu, and L.-S. Wang, *Rev. Sci. Instrum.* **85**, 083106 (2014).
- ³³G. A. García, L. Nahon, C. J. Harding, E. A. Mikajlo, and I. Powis, *Rev. Sci. Instrum.* **76**, 053302 (2005).
- ³⁴D. M. P. Holland and D. A. Shaw, *Chem. Phys.* **409**, 11 (2012).
- ³⁵N. G. Kling, D. Paul, A. Gura, G. Laurent, S. De, H. Li, Z. Wang, B. Ahn, C. H. Kim, T. K. Kim, I. V. Litvinyuk, C. L. Cocke, I. Ben-Itzhak, D. Kim, and M. F. Kling, *J. Instrum.* **9**, P05005 (2014).
- ³⁶M. L. Weichman, J. A. DeVine, D. S. Levine, J. B. Kim, and D. M. Neumark, *Proc. Natl. Acad. Sci.* **113**, 1698 (2016).
- ³⁷S. J. Kregel, G. K. Thurston, J. Zhou, and E. Garand, *J. Chem. Phys.* **147**, 094201 (2017).
- ³⁸O. Ghafur, W. Siu, P. Johnsson, M. F. Kling, M. Drescher, and M. J. J. Vrakking, *Rev. Sci. Instrum.* **80**, 033110 (2009).
- ³⁹P. Mandal, G. Sikler, and M. Mukherjee, *J. Instrum.* **6**, P02004 (2011).
- ⁴⁰J. B. Camp, T. W. Darling, and R. E. Brown, *J. Appl. Phys.* **69**, 7126 (1991).
- ⁴¹D. R. Miller, in *Atomic and Molecular Beam Methods*, edited by G. Scoles *et al.* (Oxford University Press, 1988), Vol. 1, p. 14.
- ⁴²W. Demtröder, *Laser Spectroscopy* (Springer, Berlin, Heidelberg, 1996).
- ⁴³N. Picqué and T. W. Hänsch, *Nat. Photonics* **13**, 146 (2019).
- ⁴⁴M. Weyland, X. Ren, T. Pflüger, W. Y. Baek, K. Bartschat, O. Zatsarinny, D. V. Fursa, I. Bray, H. Rabus, and A. Dorn, *EPJ Tech. Instrum.* **1**, 6 (2014).
- ⁴⁵W. Vassen, C. Cohen-Tannoudji, M. Leduc, D. Boiron, C. I. Westbrook, A. Truscott, K. Baldwin, G. Birkel, P. Cancio, and M. Trippenbach, *Rev. Mod. Phys.* **84**, 175 (2012).
- ⁴⁶P. Dombi, Z. Pápa, J. Vogelsang, S. V. Yalunin, M. Sivis, G. Herink, S. Schäfer, P. Groß, C. Ropers, and C. Lienau, *Rev. Mod. Phys.* **92**, 025003 (2020).
- ⁴⁷A. R. Bainbridge and W. A. Bryan, *New J. Phys.* **16**, 103031 (2014).
- ⁴⁸N. H. Abel, *J. Reine Angew. Math.* **1826**, 153.
- ⁴⁹M. J. J. Vrakking, *Rev. Sci. Instrum.* **72**, 4084 (2001).
- ⁵⁰V. Dribinski, A. Ossadtchi, V. A. Mandelshtam, and H. Reisler, *Rev. Sci. Instrum.* **73**, 2634 (2002).
- ⁵¹D. D. Hickstein, S. T. Gibson, R. Yurchak, D. D. Das, and M. Ryazanov, *Rev. Sci. Instrum.* **90**, 065115 (2019).
- ⁵²C. R. Gebhardt, T. P. Rakitzis, P. C. Samartzis, V. Ladopoulos, and T. N. Kitsopoulos, *Rev. Sci. Instrum.* **72**, 3848 (2001).
- ⁵³S. K. Lee, Y. F. Lin, S. Lingenfelter, L. Fan, A. H. Winney, and W. Li, *J. Chem. Phys.* **141**, 221101 (2014).
- ⁵⁴C. Cheng, G. Moğol, T. Weinacht, A. Nomerotski, and C. Trallero-Herrero, *Rev. Sci. Instrum.* **93**, 013003 (2022).
- ⁵⁵M. Wollenhaupt, M. Krug, J. Köhler, T. Bayer, C. Sarpe-Tudoran, and T. Baumert, *Appl. Phys. B* **95**, 647 (2009).
- ⁵⁶C. Smeenk, L. Arissian, A. Staudte, D. M. Villeneuve, and P. B. Corkum, *J. Phys. B: At., Mol. Opt. Phys.* **42**, 185402 (2009).
- ⁵⁷P. Hockett, M. Staniforth, and K. L. Reid, *Mol. Phys.* **108**, 1045 (2010).
- ⁵⁸J. Maurer, D. Dimitrovski, L. Christensen, L. B. Madsen, and H. Stapelfeldt, *Phys. Rev. Lett.* **109**, 123001 (2012).
- ⁵⁹S. van der Walt, J. L. Schönberger, J. Nunez-Iglesias, F. Boulogne, J. D. Warner, N. Yager, E. Guillard, and T. Yu, *PeerJ* **2**, e453 (2014).
- ⁶⁰C. Sparling and D. Townsend, *J. Chem. Phys.* **157**, 114201 (2022).
- ⁶¹V. Wössner, "Tomographische rekonstruktion dreidimensionaler photoelektronenverteilungen mittels intra-cavity velocity map imaging," B.Sc. thesis, Ruprecht-Karls-Universität, Heidelberg, 2020.
- ⁶²M. Krüger, M. Schenk, and P. Hommelhoff, *Nature* **475**, 78 (2011).
- ⁶³B. Piglosiewicz, S. Schmidt, D. J. Park, J. Vogelsang, P. Groß, C. Manzoni, P. Farinello, G. Cerullo, and C. Lienau, *Nat. Photonics* **8**, 37 (2013).
- ⁶⁴L. Zhang, Z. Miao, W. Zheng, X. Zhong, and C. Wu, *Chem. Phys.* **523**, 52 (2019).
- ⁶⁵R. R. Freeman, P. H. Bucksbaum, H. Milchberg, S. Darack, D. Schumacher, and M. E. Geusic, *Phys. Rev. Lett.* **59**, 1092 (1987).
- ⁶⁶H. Helm, N. Bjerre, M. J. Dyer, D. L. Huestis, and M. Saeed, *Phys. Rev. Lett.* **70**, 3221 (1993).
- ⁶⁷J. E. Hansen and W. Persson, *Phys. Scr.* **36**, 602 (1987).
- ⁶⁸P. Kruit, J. Kimman, H. G. Muller, and M. J. van der Wiel, *Phys. Rev. A* **28**, 248 (1983).
- ⁶⁹H. G. Muller, A. Tip, and M. J. van der Wiel, *J. Phys. B: At. Mol. Phys.* **16**, L679 (1983).
- ⁷⁰P. Hansch, M. A. Walker, and L. D. Van Woerkom, *Phys. Rev. A* **57**, R709 (1998).
- ⁷¹V. Schyja, T. Lang, and H. Helm, *Phys. Rev. A* **57**, 3692 (1998).
- ⁷²M. Goto and K. Hansen, *Phys. Scr.* **86**, 035303 (2012).
- ⁷³L. von der Wense, B. Seiferle, S. Stellmer, J. Weitenberg, G. Kazakov, A. Pálffy, and P. G. Thirolf, *Phys. Rev. Lett.* **119**, 132503 (2017).
- ⁷⁴B. Seiferle, L. von der Wense, P. V. Bilous, I. Amersdorffer, C. Lemell, F. Libisch, S. Stellmer, T. Schumm, C. E. Düllmann, A. Pálffy, and P. G. Thirolf, *Nature* **573**, 243 (2019).
- ⁷⁵K. Beeks, T. Sikorsky, T. Schumm, J. Thielking, M. V. Okhapkin, and E. Peik, *Nat. Rev. Phys.* **3**, 238 (2021).
- ⁷⁶A.-L. Viotti, M. Seidel, E. Escoto, S. Rajhans, W. P. Leemans, I. Hartl, and C. M. Heyl, *Optica* **9**, 197 (2022).

3.3 Nanometric probing with a femtosecond, intra-cavity standing wave

Journal reference:

T. Heldt, J.-H. Oelmann, L. Guth, N. Lackmann, L. Matt, T. Pfeifer, and J. R. Crespo López-Urrutia, *Nanophotonics*, **13**, 25, 4639-4646 (2024).

Digital object identifier (DOI): 10.1515/nanoph-2024-0332

Publication date: 28 November 2024

Author contribution:

I led the experimental measurements, data analysis, data visualization, simulations, and writing of the manuscript.

Supplementary material:

Two supplementary movies are available online showing the full experimental data set and additional simulation data.

Background:

In the previous publication, an electron spectrometer was introduced that investigates MPI of gases at a high repetition rate. The following work focuses on a special feature of this setup, namely that it is capable of generating highly intense standing waves. These standing waves with their nodes and antinodes exhibit an intrinsic nanometric structure on the wavelength scale (see Subsec. 2.1.1).

In this study, we aim to investigate the interaction of these standing waves with a nanotip, chosen for its comparable size and simplicity of geometry. The nanotip, modeled as a hemisphere with a small radius $r \ll \lambda/2$, is ideal for probing due to its controllable position and singular interaction point. When the standing waves interact with the tip, they generate strong near-fields that cause electron emission, which can be detected. The primary scientific question we address is how to control these local near-fields and what information about the crystal structure of the nanotip can be derived from the detected electron patterns.

Research Article

Tobias Heldt*, Jan-Hendrik Oelmann, Lennart Guth, Nick Lackmann, Lukas Matt, Thomas Pfeifer and José R. Crespo López-Urrutia

Nanometric probing with a femtosecond, intra-cavity standing wave

<https://doi.org/10.1515/nanoph-2024-0332>

Received June 24, 2024; accepted November 19, 2024;

published online November 28, 2024

Keywords: nanotip; strong-field; electron emission; ultrafast; standing wave; cavity

Abstract: Optical standing waves are intrinsically nanometric, spatially fixed interference-field patterns. At a commensurate scale, metallic nanotips serve as coherent, atom-sized electron sources. Here, we explore the localized photofield emission from a tungsten nanotip with a transient standing wave. It is generated within an optical cavity with counter-propagating femtosecond pulses from a near-infrared, 100-MHz frequency comb. Shifting the phase of the standing wave at the tip reveals its nodes and antinodes through a strong periodic modulation of the emission current. We find the emission angles to be distinct from those of a traveling wave, and attribute this to the ensuing localization of emission from different crystallographic planes. Supported by a simulation, we find that the angle of maximum field enhancement is controlled by the phase of the standing wave. Intra-cavity nanotip interaction not only provides higher intensities than in free-space propagation, but also allows for structuring the light field even in the transverse direction by selection of high-order cavity modes.

1 Introduction

Controlling electrons on the natural femtosecond time scale of light has many promising applications [1], [2]. Strong optical fields induce nonlinear emission processes confined to this or even shorter time scales [3]. Their spatial localization by nanometric structures can cause both geometric as well as plasmonic field enhancements [4]–[6] making field emission much stronger. A sharp metallic tip features up to one order of magnitude higher field strength [7] with a corresponding increase of coherent electron emission from its apex [8]. Detailed studies of this process have elucidated both a multiphoton and a strong-field regime by combining optical near-field measurements with electron spectrometry [9]–[17]. Using few-cycle lasers, such electron pulses reached into the attosecond regime [18]–[25]. Recently, both ultrafast scanning and transmission electron microscopes have achieved simultaneous nanometric spatial and femtosecond temporal resolution by steadily improving control of the free-electron phase [26]–[37]. Phase measurements on slow, tip-emitted electrons for studying optical near-fields can be performed, e.g., in point-projection electron microscopes [38]–[44]. Such applications require good understanding of the coherence properties of the electrons and nanoscopic localization of their source. One example is when several electrons are emitted per pulse leading to correlated electron-number states due to their Coulomb interaction [45], [46]. Another one is work on tungsten tips demonstrating how apex crystallography and the angle of illumination govern the emission position [47], [48].

Here, we show how combining a standing light wave, i.e. light with a nanometric optical field distribution, with a nanotip allows us to probe the electron-emission sites on a sub-wavelength scale. Our finite-difference time-domain (FDTD) simulations strongly support that tuning the phase of the standing wave, and thus the near-field at the tip, even controls the crystallographic emission locus.

*Corresponding author: Tobias Heldt, Max-Planck-Institut für Kernphysik, Saupfercheckweg 1, 69117 Heidelberg, Germany; and Heidelberg Graduate School for Physics, Ruprecht-Karls-Universität Heidelberg, Im Neuenheimer Feld 226, 69120 Heidelberg, Germany, E-mail: heldt@mpi-hd.mpg.de. <https://orcid.org/0000-0001-8156-3793>

Jan-Hendrik Oelmann, Nick Lackmann, Lukas Matt, Thomas Pfeifer and José R. Crespo López-Urrutia, Max-Planck-Institut für Kernphysik, Saupfercheckweg 1, 69117 Heidelberg, Germany, E-mail: crespojr@mpi-hd.mpg.de (J.R.C. López-Urrutia). <https://orcid.org/0000-0003-2270-8539> (J.-H. Oelmann). <https://orcid.org/0000-0001-6080-0155> (N. Lackmann). <https://orcid.org/0000-0002-5312-3747> (T. Pfeifer). <https://orcid.org/0000-0002-2937-8037> (J.-H. Oelmann)

Lennart Guth, Max-Planck-Institut für Kernphysik, Saupfercheckweg 1, 69117 Heidelberg, Germany; and Heidelberg Graduate School for Physics, Ruprecht-Karls-Universität Heidelberg, Im Neuenheimer Feld 226, 69120 Heidelberg, Germany. <https://orcid.org/0000-0002-1683-6967>

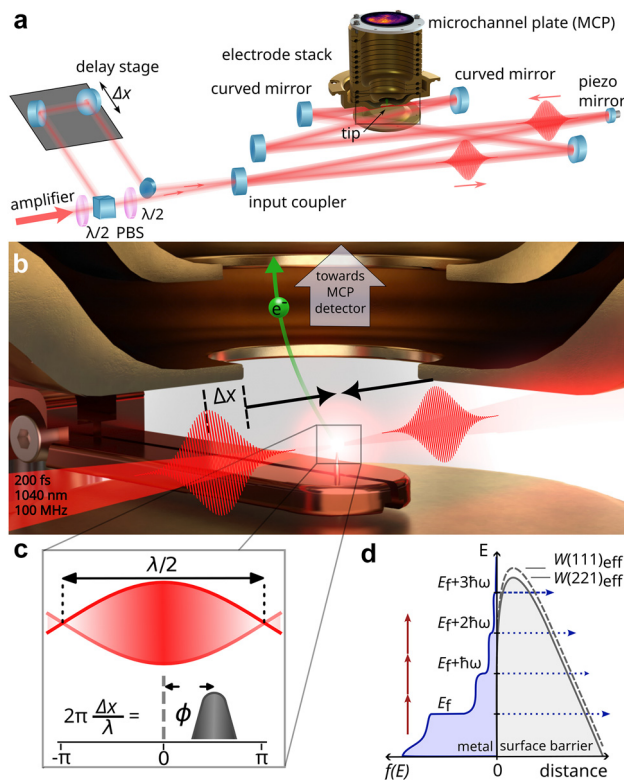


Figure 1: Principle of the experiment. (a) An amplified frequency comb is split into two branches resulting in two coherent NIR pulses counter-propagating in a cavity. (b) In the focus the pulses interfere with a relative delay of Δx above a nanometric tungsten tip. Electrons emitted there are guided by a velocity-map imaging system to a microchannel-plate detector. (c) The relative delay determines the distance between the tip apex and the next anti-node of the standing wave. (d) Multiphoton absorption results in a nonequilibrium electron distribution $f(E)$ in the tungsten tip out of which electrons can tunnel through the surface barrier. The barrier height depends on the work function of the crystallographic plane.

Figure 1a shows the optical setup and Figure 1b depicts the focal region, where two counterpropagating near-infrared (NIR) laser pulses sharing the same cavity mode interfere to form the standing wave. Its phase ϕ relative to the nanotip apex with radius $r < 50$ nm is controlled by the delay Δx between the laser pulses.

2 Results

We position a nanometric tungsten tip into the standing wave, as illustrated in Figure 1c. First, we adjusted the intensity ratio of the two counterpropagating pulses until the electron-emission pattern on the detector becomes independent of the relative delay Δx . This implied that for the given settings only one emission site was active on the tip. By changing Δx , we shift the nodes and anti-nodes

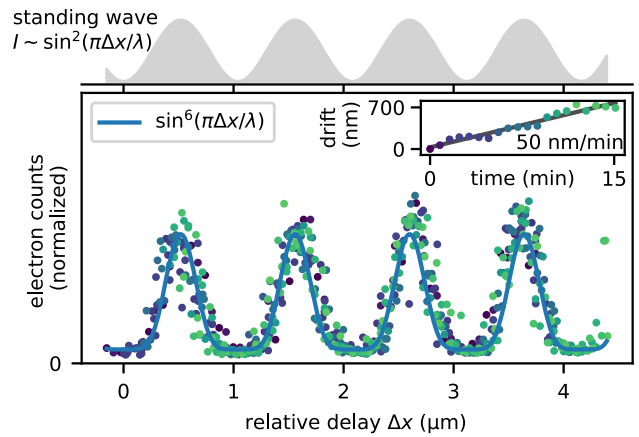


Figure 2: Measured electron yield from a tip near a standing light wave versus delay between the two interfering laser pulses. (Upper panel) Gray shaded area: laser-intensity at the tip. (Lower panel) Electron counts in 20 consecutive scans after correction for a phase drift (see inset) and amplitude normalization. Blue curve: approximation of an assumed effective third-order power dependence on the laser intensity.

with respect to the tip position while counting the emitted electrons. As shown in Figure 2, the respective electron yield exhibits a strong periodic modulation, vanishing at the nodes. The electrons have to overcome a potential barrier $W_{\text{eff}} = W - \sqrt{e^3 F (4\pi\epsilon_0)^{-1}}$, given by the work function of tungsten W reduced by the applied electric field F because of the Schottky effect [49]. Under the present conditions, multiphoton absorption raises electrons to states above the Fermi level, from which they can tunnel through a reduced potential barrier [47]. Figure 1d illustrates this emission process for two exemplary crystal planes with the corresponding nonequilibrium electron distribution [48], [50]. Due to the exponential suppression of the tunneling step, emission from the highest electronic states and from planes with the lowest work function are strongly favored. The multiphoton absorption necessary to populate these states is nonlinearly dependent on the local electric field, which is in the present study determined by the phase of the standing wave at the tip. Additionally, we observe a nearly linear drift of ~ 50 nm/min on successive measurements, which we attribute to thermal effects on the > 2 m-long, separate beam branches from the beam splitter separating the two pulses until the first cavity mirror.

In the following, we show that the standing wave can also be used to investigate the electron emission sites at the tip. We set the intensity ratio of the two counterpropagating pulses so that their electron yields (separately measured by blocking either of the two) are equally strong. Figure 3a shows the detected emission patterns resembling crescents oriented in the respective direction of laser propagation. This agrees with previous studies showing that for traveling

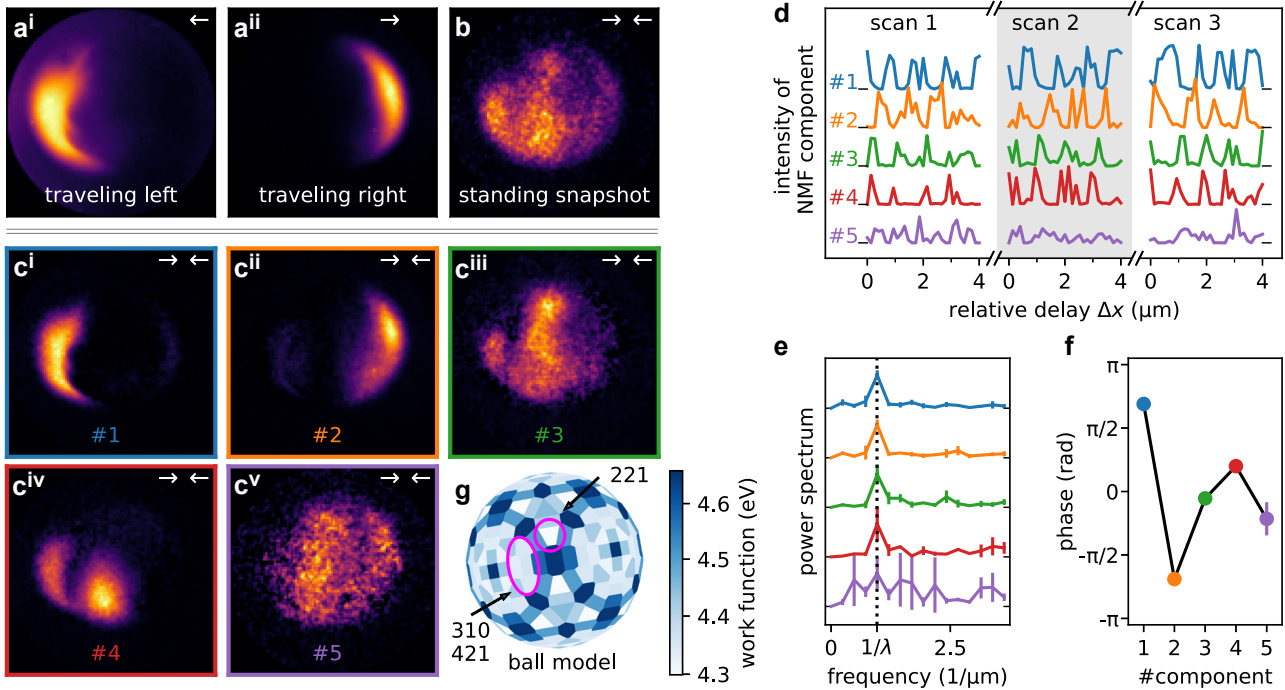


Figure 3: Spatial electron emission characteristics of the nanotip. (a) Observed emission pattern of a traveling wave propagating as the arrows show. (b) Example of pattern of electron emission induced by a standing wave. (c) Main components of a nonnegative matrix factorization (NMF) of all images recorded during three consecutive 4 μm delay scans. See main text for details. (d) Intensity evolution of the calculated components. (e) Power spectrum of each component averaged over all three scans, recovering the optical period at the dotted line. (f) Phase of each component at the scan frequency. Error bars indicate the standard deviation of the three scans. (g) Work-function map (measured in Ref. [52]) of a tungsten-tip apex with symmetry (110). Relevant crystallographic emission planes are circled in magenta.

waves the maximum near-field strength appears slightly behind the apex [48]. The emission pattern in our standing wave seems more complex; an example is given in Figure 3b. It strongly depends on the delay Δx , which we scan three times in a row over four light periods. We apply nonnegative matrix factorization (NMF) [51] on the complete dataset of 93 images to extract a suitable basis set for them. This method enables the separation of distinguishable features, also known as components, that constitute each image. Essential characteristics can often be derived from a small number of components, significantly reducing the dimensionality of the data. Compared to simple averaging, NMF is more robust against residual noise of the delay. Figure 3c shows the five strongest NMF components of the electron-emission dataset. The first two excellently match the patterns for traveling waves. In contrast, Figure 3cⁱⁱⁱ and c^{iv} show two distinct components with strong emission in the upper and lower center, respectively. The fifth one is already very noisy, which is why we ignore higher orders. Figure 3d depicts the contributions of the individual components for the delay-scan images. A Fourier transform clearly reveals the expected oscillation with the light period in the first four components (see Figure 3e). Figure 3f shows the

phase of the oscillation for the different components. The first two components differ in phase by more than π , and the phases of the others appear in between.

We attribute these phenomena to emission sites attached to crystallographic surfaces of the tungsten tip apex, which we approximate in Figure 3g with a sphere model with its apex oriented along the (110) direction. The work function of this plane $W_{110} = 5.32(10)$ eV is higher than those of all other planes, especially (221) and (310) with $W_{221} = 4.30(4)$ eV and $W_{310} = 4.34(4)$ eV [52]. According to the Fowler–Nordheim equation [53] with constants K_i , the tunnel current

$$j(F, W) = K_1 \frac{|F|^2}{W} \exp(-K_2 W^{3/2} / |F|) \quad (1)$$

is strongly suppressed by a high work function. Photofield emission is thus dominated by those crystal planes with a low one. This points to four different crystal sites with low work functions as the cause of the first four NMF components, each having a strength depending on the phase of the standing wave.

To explain these observations, we model with FDTD simulations the electric field at the tip in a standing wave. Figure 4a and b show the field amplitude at the peak

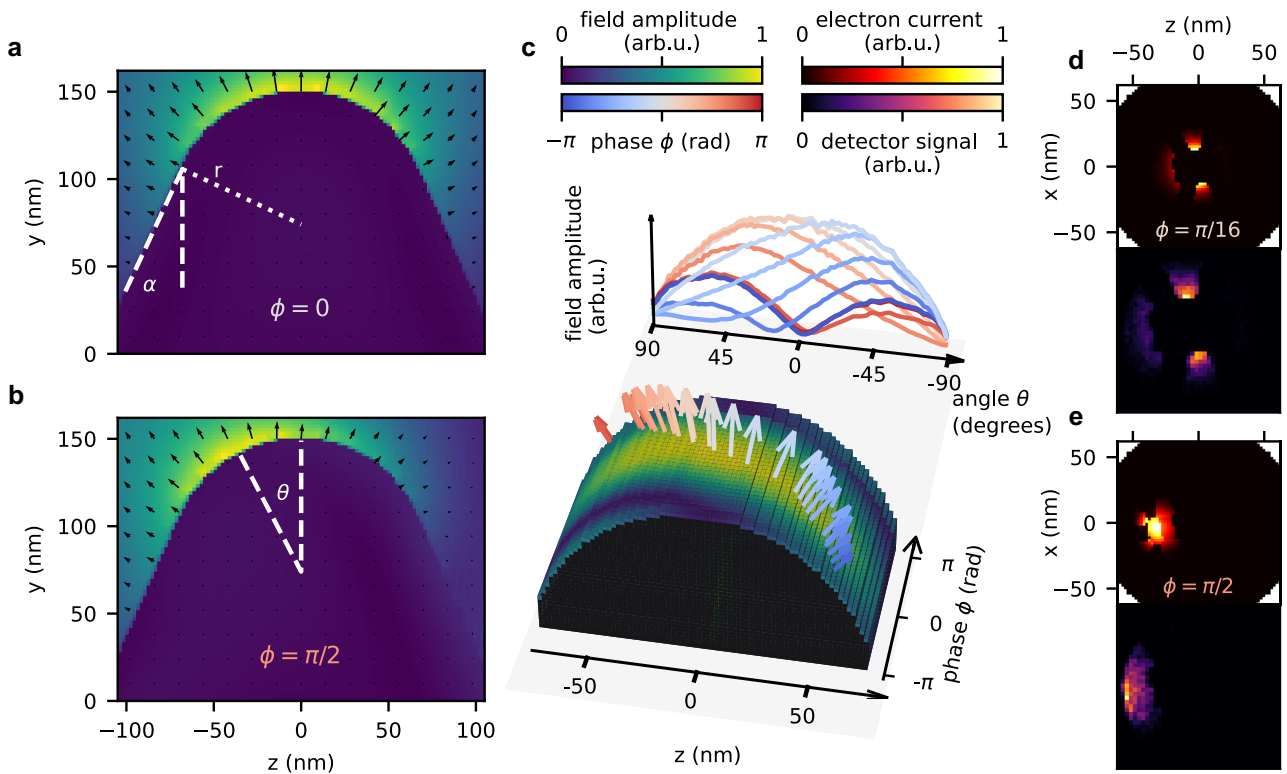


Figure 4: Simulated electric fields and resulting electron emission at the tip versus phase ϕ of the standing wave. (a, b) Peak-field distributions at the symmetry plane for a fixed phase, with tip radius r , opening angle α and electron-emission angle θ . Laser propagation along z with polarization axis y . (c) Full phase scan. Lower part: projection of the central slice on the tip surface as a function of the phase. Arrows mark the position and angle of the peak-field amplitude. Upper part: field amplitude for a subset of phases projected on the electron-emission angle. (d, e) Upper panels: electron emission at two different phases ϕ simulated with the different work functions of the ball model (see Figure 3g). Lower panels: simulated detector image after propagation through the electrode assembly. Note the similarity to the NMF components Figure 3cⁱ and c^{iv}.

absolute field for the central plane of the tip. At $\phi = 0$, the anti-node is centered at the apex, while positive values shift it toward negative z -values. The peak field shifts from the centered apex to the side as the phase changes, as displayed in Figure 4c, where the slices for different phases are stacked and the integrated field of the first 10 nm is projected onto the surface. The peak field shown as an arrow moves continuously across the tip. This indicates nanometer-scale control of the near-field by the phase of the standing wave. Considering the spatial structure of the maximal field across the tip $F_{\max}(x, z)$ and the different work functions of the sphere model $W(x, z)$ an estimate of the local electron current $j(x, z)$ can be calculated from Eq. (1). This quantity, given in Figure 4d and e together with the simulated signal, shows that the phase of the standing wave determines the location of electron emission on a nanometric crystallographic scale; our observations shown in Figure 3 are described well by this model.

3 Conclusion and outlook

We demonstrated control of electron-photofield emission from a tungsten nanotip by intra-cavity counterpropagating laser pulses forming a standing wave. The nodes and anti-nodes of this transient, spatially standing wave are reflected in a strong modulation of electron emission correlated with the local electric field strength. The emission patterns for different phases of the standing wave were analyzed using nonnegative matrix factorization. Supported by an FDTD simulation, we identify the main NMF components as the emission patterns from localized emission sites on the tungsten tip.

Based on these results, we propose the use of enhancement cavities for laser-assisted electron emission, which offer an intensity boost of a few orders of magnitude at the tip. With intensities of up to $I > 10^{13}$ W/cm², we enter a regime where we expect new applications of the Kapitza–Dirac effect [54]–[57] in the context of MHz-rate pulsed

electron sources. Furthermore, high-order Hermite–Gaussian cavity modes selected by alignment of the driving laser in-coupling would yield very pure structured light that can be used for electron emission and scattering studies [58]. Using cavity-enhanced nonclassical light is another fascinating prospect, since it imprints its statistical and coherence properties on the emitted electrons [59].

Our demonstration points to future uses of frequency-comb-locked, standing waves strongly confined in three dimensions for controlling nanometric structures. The non-linearity of electron emission could also allow for studying more complex metasurfaces. Moreover, an improved understanding of electron emission in complex field configurations and manipulation of both electron amplitude and phase with light would be beneficial for applications such as electron microscopy, electron holography, and coherent electron control.

4 Methods

4.1 Experimental setup

We use a bow-tie resonator consisting of five mirrors with a dielectric coating optimized for high damage threshold and reflectivity $R_{\text{HR}} = 0.99995$. An input coupler with lower reflectivity $R_{\text{IC}} = 0.993$ closes the cavity. Two of the mirrors are concave with a focal length of $f = 125$ mm to focus to a waist radius of $w_0 = 25$ μm ; the others are plane. One of them is glued to a piezoelectric element which allows to change the cavity length for locking it on resonance by the Pound–Drever–Hall technique [60]. The cavity enhances the intra-cavity circulating power by a factor of ~ 200 .

We use a commercial NIR frequency comb (Menlo Systems, FC1000-250) operating at a repetition rate of 100 MHz centered at 1,040 nm, a home-built rod-type amplifier to increase the average power to 13 W, and a grating compressor to reduce the pulse duration to ≤ 200 fs. These pulses pass a beam splitter of selectable intensity ratio. After it, one beam branch is delayed (Δx) by a motorized retro-reflector. After mode matching, both branches are coupled into the enhancement cavity in a counter-propagating fashion such that the pulses collide at the focus, as explained in Ref. [61].

The focus is positioned at the source point of a velocity-map imaging (VMI) spectrometer mostly used for above-threshold ionization of gaseous targets [62]. For the present study, an additional copper electrode holds a tungsten nanotip pointing toward the VMI detector. We use commercial STM probes (Bruker) made from a polycrystalline tungsten wire etched to form a tip of radius $r < 50$ nm. This treatment is known to let a (110) surface appear at the apex [63], [64].

The tip is positioned 50–100 μm below the laser focus to keep the cavity mode unblocked. For alignment, the VMI electrode assembly can be moved around the cavity focus in all three directions as a whole. We apply a bias of $-1,000$ V to the tip and appropriate voltages to the other electrodes to image the emitted electrons on a microchannel-plate detector (MCP) equipped with a phosphor screen. An air-side CCD camera records through a window the image of the electron distribution on the MCP. The cavity, the tip, the electrodes, and the detector are installed in a 2-m long ultra-high vacuum chamber at a pressure of $\approx 10^{-8}$ mbar. Two stages of air suspension decouple the whole laser setup and the chamber from vibrations.

4.2 Data evaluation

The total electron count rate is defined as the integrated CCD camera signal. Consecutive scans are normalized to the mean value of all the cycle maxima. To analyze the electron emission patterns, NMF is employed to reduce the high dimensionality of the camera images. All images are downsampled from 978×978 pixels to 100×100 ($=10,000$) pixels to eliminate pixel noise. The 93 images in the dataset are organized into a matrix \mathbf{X} of size $93 \times 10,000$. Using a coordinate-descent solver with ‘nonnegative double singular value decomposition’ (NNDSVD) initialization, the data is factorized into 12 components. This results in the best approximation of the data being separated into a coefficient matrix \mathbf{W} (93×12) and a feature matrix \mathbf{H} ($12 \times 10,000$), such that $\mathbf{WH} \approx \mathbf{X}$. The coefficients of the components in the original images are normalized. For a phase analysis at the scan frequency, a drift between scans is corrected, and an offset is chosen so that the phases of the first two components are symmetric with respect to zero.

4.3 Simulation methods

To calculate the field evolution at the tip for different phases of the standing wave, we solve the discretized Maxwell equations in a three-dimensional FDTD simulation using an open-source package [65] on a 175 (propagation direction) $\times 135$ (tip and polarization direction) $\times 151$ grid with 2 nm spacing. We use 20 nm thick perfectly matched layers as absorbing boundaries. The tip is modeled as a hemisphere with radius $r = 75$ nm and a conical shaft with half-angle $\alpha = 25^\circ$; the relative permittivity of tungsten is taken as $\epsilon = -4.03 + 22.4i$ [66]. We approximate the light field as two plane waves with a phase difference ϕ , since both the laser waist and its Rayleigh length are much larger than the simulation box. For stable numerical propagation according to the Courant–Friedrichs–Lewy condition [67], a

time step of $\Delta t = 3.8$ as is chosen for 3,000 propagation steps corresponding to three full light periods. We determine the time of maximum field for each phase separately, and use a median filter with the size of three pixels to account for discretization errors of the field amplitude. For estimating the emission probability, the sizes of the median filters in the xz -dimensions were extended to nine pixels. At each position on the tip surface, we approximate the emission by the contribution of the maximum field amplitude obtained during the laser cycle. We smooth the map of maximum field amplitudes by a Gaussian kernel with a size of three pixels, scale the maximum field to 1 GV/m corresponding to an intensity of 2.7×10^{11} W/cm² and use it as the input field $|F|$ in Eq. (1). In this way, for each of the central 64×64 pixels a measure for the emission probability is calculated dependent on the local work function. For the spatial structure of the different crystallographic planes on a hemisphere, we use the software VESTA [68]. The orientation of the crystal facets was rotated by 10° to match the experimental results. The respective work functions of all planes, which are used for the calculation, are given in Table 1.

A total of 10,000 electron emission sites were sampled for each phase of the standing wave, representing the spatially dependent Fowler–Nordheim emission currents. It was assumed that electrons move perpendicularly to the surface for the first 0.6 mm, after which they were propagated in an electrostatic model of the electrode assembly (grid size 0.2 mm) towards the detector using the software SIMION [69].

Table 1: Work functions of tungsten for the modeling of the emission probabilities. Taken from Ref. [52].

Crystal plane	Work function (eV)
(110)	5.32 ± 0.10
(211)	5.12 ± 0.07
(100)	4.93 ± 0.06
(320)	4.58 ± 0.06
(321)	4.50 ± 0.06
(111)	4.45 ± 0.05
(610)	4.43 ± 0.04
(411)	4.42 ± 0.05
(332)	4.41 ± 0.05
(210)	4.36 ± 0.04
(421)	4.35 ± 0.05
(310)	4.34 ± 0.04
(611)	4.32 ± 0.04
(221)	4.30 ± 0.04

Acknowledgment: We thank the fine-mechanics workshop at MPIK lead by Thorsten Spranz for the excellent manufacturing of our experimental apparatus, the divisional mechanical workshop lead by Christian Kaiser for prompt support at the laboratory, and our engineering-design office headed by Frank Müller for their help.

Research funding: This work was funded by the Max-Planck-Gesellschaft, the Max-Planck-RIKEN-PTB-Center for Time, Constants and Fundamental Symmetries. This work has been funded by the “European Metrology Programme for Innovation and Research” (EMPIR) projects 20FUN01 TSCAC and 23FUN03 HIOC. This project has received funding from the EMPIR programme co-financed by the participating states and from the European Union’s Horizon 2020 research and innovation programme.

Author contributions: All authors have accepted responsibility for the entire content of this manuscript and approved its submission.

Conflict of interest: Authors state no conflict of interest.

Data availability: The datasets generated during and analyzed during the current study are available from the corresponding author on reasonable request.

References

- [1] W. E. King, *et al.*, “Ultrafast electron microscopy in materials science, biology, and chemistry,” *J. Appl. Phys.*, vol. 97, no. 11, p. 111101, 2005.
- [2] M. Borsch, M. Meierhofer, R. Huber, and M. Kira, “Lightwave electronics in condensed matter,” *Nat. Rev. Mater.*, vol. 8, no. 10, pp. 668–687, 2023.
- [3] F. Krausz and M. Ivanov, “Attosecond physics,” *Rev. Mod. Phys.*, vol. 81, no. 1, pp. 163–234, 2009.
- [4] P. Dombi, *et al.*, “Ultrafast strong-field photoemission from plasmonic nanoparticles,” *Nano Lett.*, vol. 13, no. 2, pp. 674–678, 2013.
- [5] P. Dombi, *et al.*, “Strong-field nano-optics,” *Rev. Mod. Phys.*, vol. 92, no. 2, p. 025003, 2020.
- [6] J. Heimerl, T. Higuchi, M. Ammon, M. A. Schneider, and P. Hommelhoff, “Gap-size dependence of optical near fields in a variable nanoscale two-tip junction,” *Phys. Rev. B*, vol. 101, no. 12, p. 125403, 2020.
- [7] S. Thomas, G. Wachter, C. Lemell, J. Burgdörfer, and P. Hommelhoff, “Large optical field enhancement for nanotips with large opening angles,” *New J. Phys.*, vol. 17, no. 6, p. 063010, 2015.
- [8] B. Cho, T. Ichimura, R. Shimizu, and C. Oshima, “Quantitative evaluation of spatial coherence of the electron beam from low temperature field emitters,” *Phys. Rev. Lett.*, vol. 92, no. 24, p. 246103, 2004.
- [9] P. Hommelhoff, Y. Sortais, A. Aghajani-Talesh, and M. A. Kasevich, “Field emission tip as a nanometer source of free electron femtosecond pulses,” *Phys. Rev. Lett.*, vol. 96, no. 7, p. 077401, 2006.

- [10] C. Ropers, D. R. Solli, C. P. Schulz, C. Lienau, and T. Elsaesser, “Localized multiphoton emission of femtosecond electron pulses from metal nanotips,” *Phys. Rev. Lett.*, vol. 98, no. 4, p. 043907, 2007.
- [11] M. Schenk, M. Krüger, and P. Hommelhoff, “Strong-field above-threshold photoemission from sharp metal tips,” *Phys. Rev. Lett.*, vol. 105, no. 25, p. 257601, 2010.
- [12] R. Bormann, M. Gulde, A. Weismann, S. V. Yalunin, and C. Ropers, “Tip-enhanced strong-field photoemission,” *Phys. Rev. Lett.*, vol. 105, no. 14, p. 147601, 2010.
- [13] H. Yanagisawa, *et al.*, “Energy distribution curves of ultrafast laser-induced field emission and their implications for electron dynamics,” *Phys. Rev. Lett.*, vol. 107, no. 8, p. 087601, 2011.
- [14] M. Krüger, M. Schenk, P. Hommelhoff, G. Wachter, C. Lemell, and J. Burgdörfer, “Interaction of ultrashort laser pulses with metal nanotips: a model system for strong-field phenomena,” *New J. Phys.*, vol. 14, no. 8, p. 085019, 2012.
- [15] G. Wachter, C. Lemell, J. Burgdörfer, M. Schenk, M. Krüger, and P. Hommelhoff, “Electron rescattering at metal nanotips induced by ultrashort laser pulses,” *Phys. Rev. B*, vol. 86, no. 3, 2012. <https://doi.org/10.1103/physrevb.86.035402>.
- [16] M. Krüger, S. Thomas, M. Förster, and P. Hommelhoff, “Self-probing of metal nanotips by rescattered electrons reveals the nano-optical near-field,” *J. Phys. B: At. Mol. Opt. Phys.*, vol. 47, no. 12, p. 124022, 2014.
- [17] J. Schötz, *et al.*, “Onset of charge interaction in strong-field photoemission from nanometric needle tips,” *Nanophotonics*, vol. 10, no. 14, pp. 3769–3775, 2021.
- [18] M. Krüger, M. Schenk, and P. Hommelhoff, “Attosecond control of electrons emitted from a nanoscale metal tip,” *Nature*, vol. 475, no. 7354, pp. 78–81, 2011.
- [19] M. Krüger, M. Schenk, M. Förster, and P. Hommelhoff, “Attosecond physics in photoemission from a metal nanotip,” *J. Phys. B: At. Mol. Opt. Phys.*, vol. 45, no. 7, p. 074006, 2012.
- [20] K. E. Echternkamp, G. Herink, S. V. Yalunin, K. Rademann, S. Schäfer, and C. Ropers, “Strong-field photoemission in nanotip near-fields: from quiver to sub-cycle electron dynamics,” *Appl. Phys. B*, vol. 122, no. 4, p. 80, 2016.
- [21] M. Krüger, C. Lemell, G. Wachter, J. Burgdörfer, and P. Hommelhoff, “Attosecond physics phenomena at nanometric tips,” *J. Phys. B: At. Mol. Opt. Phys.*, vol. 51, no. 17, p. 172001, 2018.
- [22] P. D. Keathley, *et al.*, “Vanishing carrier-envelope-phase-sensitive response in optical-field photoemission from plasmonic nanoantennas,” *Nat. Phys.*, vol. 15, no. 11, pp. 1128–1133, 2019.
- [23] M. Eldar, S. Abo-Toame, and M. Krüger, “Sub-optical-cycle electron pulse trains from metal nanotips,” *J. Phys. B: At. Mol. Opt. Phys.*, vol. 55, no. 7, p. 074001, 2022.
- [24] P. Dienstbier, *et al.*, “Tracing attosecond electron emission from a nanometric metal tip,” *Nature*, vol. 616, no. 7958, pp. 702–706, 2023.
- [25] H. Y. Kim, M. Garg, S. Mandal, L. Seiffert, T. Fennel, and E. Goulielmakis, “Attosecond field emission,” *Nature*, vol. 613, no. 7945, pp. 662–666, 2023.
- [26] L. Piazza, *et al.*, “Simultaneous observation of the quantization and the interference pattern of a plasmonic near-field,” *Nat. Commun.*, vol. 6, no. 1, p. 6407, 2015.
- [27] A. Feist, K. E. Echternkamp, J. Schauss, S. V. Yalunin, S. Schäfer, and C. Ropers, “Quantum coherent optical phase modulation in an ultrafast transmission electron microscope,” *Nature*, vol. 521, no. 7551, pp. 200–203, 2015.
- [28] K. E. Priebe, *et al.*, “Attosecond electron pulse trains and quantum state reconstruction in ultrafast transmission electron microscopy,” *Nat. Photonics*, vol. 11, no. 12, pp. 793–797, 2017.
- [29] K. E. Echternkamp, A. Feist, S. Schäfer, and C. Ropers, “Ramsey-type phase control of free-electron beams,” *Nat. Phys.*, vol. 12, no. 11, pp. 1000–1004, 2016.
- [30] Y. Morimoto and P. Baum, “Diffraction and microscopy with attosecond electron pulse trains,” *Nat. Phys.*, vol. 14, no. 3, pp. 252–256, 2018.
- [31] Y. Morimoto and P. Baum, “Attosecond control of electron beams at dielectric and absorbing membranes,” *Phys. Rev. A*, vol. 97, no. 3, p. 033815, 2018.
- [32] Y. Morimoto and P. Baum, “Single-cycle optical control of beam electrons,” *Phys. Rev. Lett.*, vol. 125, no. 19, p. 193202, 2020.
- [33] A. Feist, S. V. Yalunin, S. Schäfer, and C. Ropers, “High-purity free-electron momentum states prepared by three-dimensional optical phase modulation,” *Phys. Rev. Res.*, vol. 2, no. 4, p. 043227, 2020.
- [34] Y. Kurman, *et al.*, “Spatiotemporal imaging of 2d polariton wave packet dynamics using free electrons,” *Science*, vol. 372, no. 6547, pp. 1181–1186, 2021.
- [35] R. Shiloh, T. Chlouba, and P. Hommelhoff, “Quantum-coherent light-electron interaction in a scanning electron microscope,” *Phys. Rev. Lett.*, vol. 128, no. 23, p. 235301, 2022.
- [36] J. H. Gaida, *et al.*, “Lorentz microscopy of optical fields,” *Nat. Commun.*, vol. 14, no. 1, p. 6545, 2023.
- [37] J. H. Gaida, *et al.*, “Attosecond electron microscopy by free-electron homodyne detection,” *Nat. Photonics*, vol. 18, no. 5, pp. 509–515, 2024.
- [38] M. Müller, A. Paarmann, and R. Ernstorfer, “Femtosecond electrons probing currents and atomic structure in nanomaterials,” *Nat. Commun.*, vol. 5, no. 1, p. 5292, 2014.
- [39] M. Müller, V. Kravtsov, A. Paarmann, M. B. Raschke, and R. Ernstorfer, “Nanofocused plasmon-driven sub-10 fs electron point source,” *ACS Photonics*, vol. 3, no. 4, pp. 611–619, 2016.
- [40] J. Vogelsang, G. Hergert, D. Wang, P. Groß, and C. Lienau, “Observing charge separation in nanoantennas via ultrafast point-projection electron microscopy,” *Light: Sci. Appl.*, vol. 7, no. 1, p. 55, 2018.
- [41] J. Vogelsang, *et al.*, “Plasmonic-nanofocusing-based electron holography,” *ACS Photonics*, vol. 5, no. 9, pp. 3584–3593, 2018.
- [42] G. Hergert, *et al.*, “Probing transient localized electromagnetic fields using low-energy point-projection electron microscopy,” *ACS Photonics*, vol. 8, no. 9, pp. 2573–2580, 2021.
- [43] A. Wöste, *et al.*, “Ultrafast coupling of optical near fields to low-energy electrons probed in a point-projection microscope,” *Nano Lett.*, vol. 23, no. 12, pp. 5528–5534, 2023.
- [44] F. Chahshouri and N. Talebi, “Numerical investigation of sequential phase-locked optical gating of free electrons,” *Sci. Rep.*, vol. 13, no. 1, p. 18949, 2023.
- [45] R. Haindl, K. Köster, J. H. Gaida, M. Franz, A. Feist, and C. Ropers, “Femtosecond tunable-wavelength photoassisted cold field emission,” *Appl. Phys. B*, vol. 129, no. 3, p. 40, 2023.
- [46] S. Meier, J. Heimerl, and P. Hommelhoff, “Few-electron correlations after ultrafast photoemission from nanometric needle tips,” *Nat. Phys.*, vol. 19, no. 10, pp. 1402–1409, 2023.

- [47] H. Yanagisawa, *et al.*, “Optical control of field-emission sites by femtosecond laser pulses,” *Phys. Rev. Lett.*, vol. 103, no. 25, p. 257603, 2009.
- [48] H. Yanagisawa, *et al.*, “Laser-induced field emission from a tungsten tip: optical control of emission sites and the emission process,” *Phys. Rev. B*, vol. 81, no. 11, p. 115429, 2010.
- [49] W. Schottky, “Über den einfluss von strukturwirkungen, besonders der thomsonschen bildkraft, auf die elektronenemission der metalle,” *Phys. Z.*, vol. 15, pp. 872–878, 1914.
- [50] L. Wu and L. K. Ang, “Nonequilibrium model of ultrafast laser-induced electron photofield emission from a dc-biased metallic surface,” *Phys. Rev. B*, vol. 78, no. 22, p. 224112, 2008.
- [51] A. Cichocki and A.-H. Phan, “Fast local algorithms for large scale nonnegative matrix and tensor factorizations,” *IEICE Trans. Fund. Electron. Commun. Comput. Sci.*, vol. E92.A, no. 3, pp. 708–721, 2009.
- [52] S. Hellwig and J. H. Block, “Messung der Austrittsarbeit des Wolframs mit Hilfe der Feldemission,” *Z. Phys. Chem.*, vol. 83, nos. 5–6, pp. 269–286, 1973.
- [53] R. H. Fowler and L. Nordheim, “Electron emission in intense electric fields,” *Proc. R. Soc. Lond. — Ser. A Contain. Pap. Math. Phys. Character.*, vol. 119, no. 781, pp. 173–181, 1928.
- [54] P. L. Kapitza and P. A. M. Dirac, “The reflection of electrons from standing light waves,” *Math. Proc. Camb. Phil. Soc.*, vol. 29, no. 2, pp. 297–300, 1933.
- [55] N. Talebi and C. Lienau, “Interference between quantum paths in coherent Kapitza–Dirac effect,” *New J. Phys.*, vol. 21, no. 9, p. 093016, 2019.
- [56] P. H. Bucksbaum, D. W. Schumacher, and M. Bashkansky, “High-intensity Kapitza–Dirac effect,” *Phys. Rev. Lett.*, vol. 61, no. 10, pp. 1182–1185, 1988.
- [57] K. Lin, *et al.*, “Ultrafast Kapitza–Dirac effect,” *Science*, vol. 383, no. 6690, pp. 1467–1470, 2024.
- [58] S. Ebel and N. Talebi, “Inelastic electron scattering at a single-beam structured light wave,” *Commun. Phys.*, vol. 6, no. 1, pp. 1–8, 2023.
- [59] J. Heimerl, *et al.*, “Multiphoton electron emission with non-classical light,” *Nat. Phys.*, vol. 20, no. 6, pp. 945–950, 2024.
- [60] R. W. P. Drever, *et al.*, “Laser phase and frequency stabilization using an optical resonator,” *Appl. Phys. B*, vol. 31, no. 2, pp. 97–105, 1983.
- [61] J.-H. Oelmann, *Highly Nonlinear Light-Matter Interaction Using Cavity-Enhanced Frequency Combs*, Ph.D. thesis, Heidelberg University, Heidelberg, Germany, 2023.
- [62] J.-H. Oelmann, *et al.*, “Photoelectron tomography with an intra-cavity velocity-map imaging spectrometer at 100MHz repetition rate,” *Rev. Sci. Instrum.*, vol. 93, no. 12, p. 123303, 2022.
- [63] T. Irisawa, T. K. Yamada, and T. Mizoguchi, “Spin polarization vectors of field emitted electrons from Fe/W tips,” *New J. Phys.*, vol. 11, no. 11, p. 113031, 2009.
- [64] T. K. Yamada, T. Abe, N. M. K. Nazriq, and T. Irisawa, “Electron-bombarded <110>-oriented tungsten tips for stable tunneling electron emission,” *Rev. Sci. Instrum.*, vol. 87, no. 3, p. 033703, 2016.
- [65] F. Laporte, “fdtd python package,” Version 0.3.6. (2023), Available at: <https://github.com/flaport/fdtd>
- [66] M. A. Ordal, R. J. Bell, R. W. Alexander, L. A. Newquist, and M. R. Query, “Optical properties of al, fe, ti, ta, w, and mo at submillimeter wavelengths,” *Appl. Opt.*, vol. 27, no. 6, pp. 1203–1209, 1988.
- [67] R. Courant, K. Friedrichs, and H. Lewy, “Über die partiellen differenzgleichungen der mathematischen physik,” *Math. Ann.*, vol. 100, no. 1, pp. 32–74, 1928.
- [68] K. Momma and F. Izumi, “VESTA 3 for three-dimensional visualization of crystal, volumetric and morphology data,” *J. Appl. Crystallogr.*, vol. 44, no. 6, pp. 1272–1276, 2011.
- [69] D. A. Dahl, “Simion for the personal computer in reflection,” *Int. J. Mass Spectrom.*, vol. 200, no. 1, pp. 3–25, 2000.

Supplementary Material: This article contains supplementary material (<https://doi.org/10.1515/nanoph-2024-0332>).

3.4 Velocity-map imaging with counter-propagating laser pulses

Journal reference:

T. Heldt, J.-H. Oelmann, L. Guth, N. Lackmann, T. Pfeifer, and J. R. Crespo López-Urrutia, *Optics Letters* **49**, 23, 6825-6828 (2024).

Digital object identifier (DOI): 10.1364/OL.540612

Publication date: 25 November 2024

Author contribution:

I led the experimental measurements, data analysis, data visualization, simulations, and writing of the manuscript.

Background:

The last work presented in this thesis uses the same setup as the previous two publications. We are still interested in the light-matter interaction of intense standing waves, but we switch from a nanometric solid-state target to xenon noble gas atoms. Xenon is delivered to the interaction region as a diffusive jet, so there is no intrinsic structure in the target. The relevant length scale here is therefore not the wavelength of the light, but the size of the pulse envelope, which is about 60 μm . We investigate how the ATI electron spectra of xenon change when we use standing waves instead of traveling waves for ionization.

The observed effects result from the reduced interaction volume and the constructive interference in the antinodes, which leads to a doubling of the maximum intensity.



Optics Letters

Velocity-map imaging with counter-propagating laser pulses

TOBIAS HELDT,^{1,2,*}  JAN-HENDRIK OELMANN,¹ LENNART GUTH,^{1,2} NICK LACKMANN,¹ THOMAS PFEIFER,¹  AND JOSÉ R. CRESPO LÓPEZ-URRUTIA¹

¹Max-Planck-Institut für Kernphysik, Saupfercheckweg 1, Heidelberg 69117, Germany

²Heidelberg Graduate School for Physics, Ruprecht-Karls-Universität Heidelberg, Im Neuenheimer Feld 226, Heidelberg 69120, Germany

*heldt@mpi-hd.mpg.de

Received 9 September 2024; revised 26 October 2024; accepted 27 October 2024; posted 29 October 2024; published 25 November 2024

Velocity-map imaging (VMI) is a key tool for studying outgoing electrons or ions following optical strong-field interactions of atoms and molecules and provides good momentum resolution even if the source volume of the fragments extends along a laser beam path. Here, we demonstrate within an enhancement cavity how, independently of the focal Rayleigh length, counter-propagating pulses longitudinally compress the ionization volume down to few tens of micrometers. We observe nonlinear above-threshold ionization (ATI) processes confined to the spatial overlap of femtosecond pulses, whereas the shortened ionization volume makes an electrostatic lens unnecessary for VMI.

© 2024 Optica Publishing Group under the terms of the [Optica Open Access Publishing Agreement](#)

<https://doi.org/10.1364/OL.540612>

Strong-field laser studies of the highly nonlinear light–matter interaction in the regimes of multiphoton ionization (MPI) and tunnel ionization offer insight to the dynamics of the electronic response in matter even within an oscillation period of the optical field. An essential technique for such attosecond-resolution investigations is high-harmonic generation (HHG) because it can produce extreme ultraviolet (XUV) light [1–5], leading to optical methods such as transient absorption [6,7] or HHG spectroscopy [8–10]. Other observables of the light–matter interplay are charged fragments resulting from an ionization or dissociation. A variety of techniques exists to measure the energies and angular distributions of these particles [11]. Velocity-map imaging (VMI) [12] has many advantages over the previous main method, ion imaging with grids [13], and has therefore become a workhorse for the community [14–23]. VMI combines a 4π detection solid angle with angular resolution; by tomographic [24,25] or slicing techniques [26,27], it even extends the 2D mapping of momenta to the third dimension, and it can operate at higher repetition rates and with less technical complexity than coincidence detection schemes such as cold target recoil ion momentum spectrometry [28–30].

The high nonlinearity of MPI or tunnel ionization requires intensities that only femtosecond laser pulses focused to a small beam-waist radius w_0 can produce. The achievable size of the

focus is constrained by experimental factors, including geometric limitations and potential space-charge effects. The interaction volume along the laser axis extends either to the Rayleigh length $z_R = \pi w_0^2 \lambda^{-1}$ or to the millimeter-scale diameter of a target-gas jet or cell. The blurring of the momentum image of electrons and ions caused by this elongation is solved in the VMI technique by introducing an Einzel electrostatic lens generating sharp momentum images independently of the source size [31].

In this study of the above-threshold ionization (ATI) of xenon [32], we show how two counter-propagating femtosecond pulses increase the maximum intensity at the focus and shorten the interaction volume, rendering the electrostatic lens unnecessary for high resolution of the electron momenta.

We implement our VMI system within an enhancement cavity coherently driven by an amplified infrared frequency comb. This allows us to reach the intensities required for ATI at a 100 MHz repetition rate, and reduces the number of electrons emitted per pulse to less than one, suppressing space-charge distortions while ensuring high overall count rates. A commercial near-infrared (NIR) frequency comb (Menlo Systems, FC1000-250) centered at 1039 nm is amplified to an average power of up to 80 W, compressed to a ≤ 200 fs pulse duration and subsequently sent to the passive enhancement cavity. The bow-tie resonator comprises five highly reflective dielectric mirrors optimized for high damage threshold and low dispersion and an input coupler with a reflectivity of $R_{IC} = 0.993$. Two of the mirrors are concave with radii of curvature of 125 mm to focus both of the counter-propagating pulses to a common point with a waist radius of $w_0 = 25 \mu\text{m}$. The remaining mirrors are planar. One of them is glued to a piezoelectric element, which enables locking of the resonator to the frequency comb using the Pound–Drever–Hall technique [33], thereby enhancing the circulating power by a factor of ~ 200 . This is measured in both propagation directions by photodiodes monitoring the residual mirror-transmitted light. Prior to the cavity, we separate the pulses into two branches with selectable intensity ratio by introducing a half-wave plate and a polarizing beam splitter in the optical path (for details, see [34]). A motorized retro-reflector controls the delay of one branch by Δx . Following optical mode matching, the polarization of both branches is aligned to each other, and both beams are coupled into the enhancement cavity in a counter-propagating manner. The delay is set to allow the pulses to coincide at the cavity

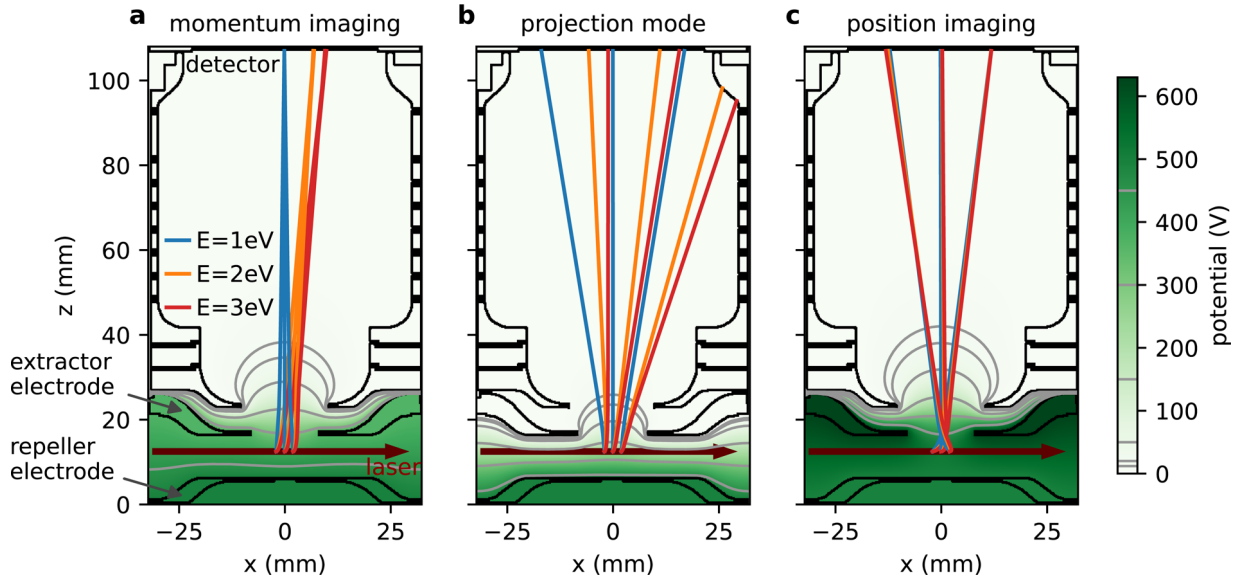


Fig. 1. Different configurations of our electrode stack with simulated electron trajectories. The electrodes are outlined in black and the electric potential as a green colormap with gray contour lines. Nine exemplary electron trajectories are displayed in blue, orange, and red for 1, 2, and 3 eV initial kinetic energy, respectively. Their ionization locations along the laser-propagation axis are separated by 2 mm, with the initial momenta set along the x direction. Details on the electrode settings (a)–(c) are given in the main text.

focus, where they interfere to form a transient standing wave. The cavity also ensures perfect transversal alignment for both propagation directions, since they share the same transversal TEM_{00} mode of the resonator.

The cavity focus is the source point of an electron VMI spectrometer consisting of a set of 13 electrodes [35]. For alignment, this assembly can be moved in all three directions as a whole. An effusive beam of xenon atoms enters the VMI through an aperture of 0.6 mm diameter in the repeller electrode at the bottom. All components are installed in an ultrahigh vacuum chamber at a pressure level of 10^{-8} mbar, which raises during the operation of the xenon beam to 4×10^{-6} mbar. Electrons emitted by ATI are guided by the spectrometer to a microchannel-plate detector (MCP) equipped with a phosphor screen, which is imaged by an air-side CCD camera. The recorded images are mirrored about the horizontal and vertical axes for symmetrization, excluding a quadrant with a defect in the detector from analysis.

We simulated the electron trajectories for different voltage settings of the VMI spectrometer using the software SIMION [36]. The program solves the Laplace equation for a gridded model of the assembly (resolution of 0.2 mm) and propagates electrons with defined initial conditions accordingly. Figure 1 illustrates the three different electrode configurations that we have studied here. They solely differ in the voltage (U_{extr}) applied to the extractor electrode, since the repeller electrode is always set at $U_{\text{rep}} = -500$ V, and all other electrodes are at ground potential.

In the *momentum-imaging mode* depicted in Fig. 1(a), we set $U_{\text{extr}} = -370$ V to achieve VMI conditions. Electrons with different initial momenta hit the detector at radial and angular positions dependent on those. In the case displayed in Fig. 1(b), the extractor electrode is also at ground potential, and only the repeller is biased. We refer to this configuration as the *projection mode*. In this case, the detected positions depend on both the initial position and momentum, i.e., neither momentum nor position is mapped by the detector. While this is in principle not desirable, the mode serves as a model system for experimental conditions where there is only limited control over the extraction

fields. The third case, illustrated in Fig. 1(c), is referred to as the *position-imaging mode*. By setting $U_{\text{extr}} = -630$ V, the electrons are imaged onto the detector regardless of their initial momentum, and a magnified image of the source volume is recorded.

Figure 2 displays the recorded ATI rings for excitation with a single pulse or with two counter-propagating pulses. The maximum intensity if the laser is only focused from one side is $I_0 = (4.0 \pm 0.5) \times 10^{12}$ W/cm². We denote the corresponding electric field as E_0 . Splitting the pulse into two of equal power results in $I_{\text{split}} = I_0/2$ and $E_{\text{split}} = E_0/\sqrt{2}$, respectively. Both pulses overlap and interfere at the focus to a transient standing wave. Therefore, the field reaches in the antinodes of this standing wave a maximum value of $E_{\text{antinode}} = 2E_{\text{split}} = \sqrt{2}E_0$. Thus, the maximum intensity $I_{\text{antinode}} = 2I_0$ is doubled compared to the single pulse operation, even though the total power of the two pulses stays constant. This is apparent in the recorded images in the *momentum-imaging mode* shown in Fig. 2(a)–2(c). The higher peak intensity of the counter-propagating pulses leads to the appearance of higher-order ATI rings. The observed shrinking of the diameter of the inner ring is due to its inverse dependence on the ponderomotive potential:

$$U_p = \frac{e^2}{8m_e\pi^2\epsilon_0c^3}I\lambda^2, \quad (1)$$

with ϵ_0 the vacuum permittivity and the electron mass and charge denoted as m_e and e , respectively. The ponderomotive energy is proportional to the intensity and effectively increases the ionization potential I_p , such as the energy of the released electrons E_e for an n -photon process reduces to $E_e = nE_{\text{photon}} - I_p - U_p$. Due to the AC Stark effect, the higher-lying Rydberg states shift also approximately with the ponderomotive energy.

Using counter-propagating pulses, the state $5p^5(^2P_{3/2})4f$ becomes resonant with a ten photon excitation from the ground state at an intensity of 6.7×10^{12} W cm⁻² [22]. This Freeman resonance [37] dominates the signal in Fig. 2(b), whereas for single

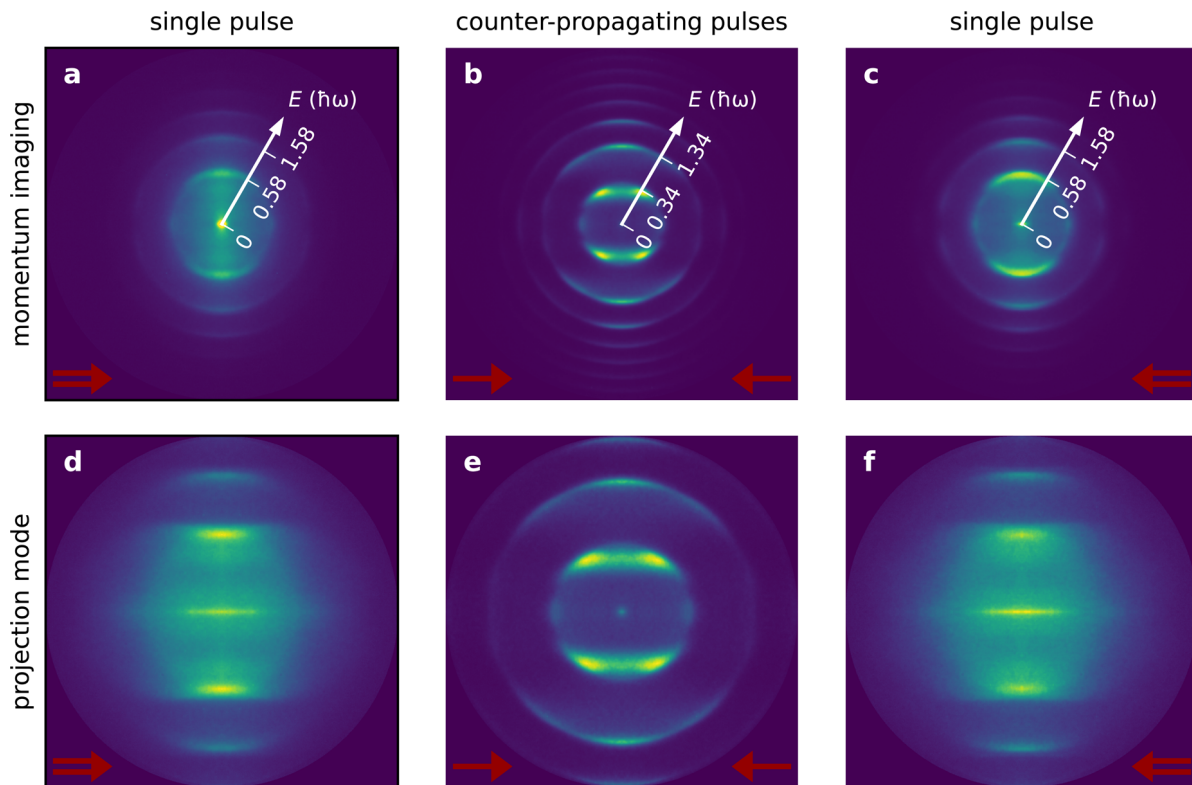


Fig. 2. (a)–(c) Detector images of ATI rings for classical VMI and (d)–(f) VMI without an electrostatic lens. Red arrows indicate the propagation direction of the light. Notice the blurring of the images along this direction for one-sided illumination in (d) and (f) the *projection mode*.

pulses, the intensity is not sufficient to reach the resonance. To show the consistency of this assignment, we use Eq. (1) to convert the difference in energy of the first ATI rings to a difference of intensity during ionization. For single pulses, the energy of the electrons of the first ring is $0.58 \hbar\omega$, and for counter-propagating light, the electrons have $0.34 \hbar\omega$. The difference of $(0.58 - 0.34) \hbar\omega = 0.29 \text{ eV}$ in the ponderomotive potential corresponds to $2.8 \times 10^{12} \text{ W cm}^{-2}$, which is exactly the difference between I_0 and the intensity at which the $4f$ state becomes resonant. It is possible to neglect focal averaging because in the absence of a suitable resonance, the emission predominantly occurs at the position of the maximum intensity, due to the high nonlinearity of MPI.

For pulses traveling only in one direction, the electrostatic lens is essential to obtain a sharp momentum image. In contrast, the images in the *projection mode* shown in Figs. 2(d) and 2(f) are distorted along the propagation axis. The electron position at the detector depends not only on its momentum upon ionization but also on the position where it took place. Since the laser intensity along the propagation direction only drops by a factor of $\sqrt{2}$ within the Rayleigh length $z_R = 1.9 \text{ mm}$, the images smear out. However, using two counter-propagating pulses, the detected electrons still form sharp rings corresponding to a momentum map in Fig. 2(e). We explain this finding with a strongly reduced length of the ionization volume.

To measure the length of the ionization volume, we employ the *position-imaging mode* of the detector as shown in Fig. 3. For single pulses, we measure an extended line with a length of 1.45 mm . This is in good agreement with the expected value of $2z_R/\sqrt{n} = 1.2 \text{ mm}$ for an $n = 10$ photon process, given the uncertainty on the focus waist size. For counter-propagating

pulses, the ionization volume becomes much shorter because the nonlinearity of the multiphoton process will confine ATI to the antinodes of the standing wave during the spatiotemporal overlap of the two pulses. The pulse duration of $\text{FWHM} = 200 \text{ fs}$ corresponds to $60 \mu\text{m}$ in space, which is comparable to the FWHM beam diameter ($\sqrt{2 \log 2} w_0 \approx 30 \mu\text{m}$) at the focus. Since this is smaller than the recorded size of the spot, we conclude that the resolution of the electron *position-imaging mode* is not sufficient to resolve these scales.

Figure 3(d) shows how the delay between the two pulses controls the position of the overlap region along the optical axis. By shifting it from the focal point, one can tune the beam radius and thus the effective maximum intensity at the pulse overlap.

In conclusion, we performed VMI experiments on strong-field ionized xenon with intra-cavity femtosecond pulses from an NIR frequency comb in two modes, using traveling as well as standing waves. The latter doubles the maximum intensity and shortens the source volume by more than one order of magnitude, namely, to the spatiotemporal overlap of the two pulses. This volume reduction makes it possible to image the momenta of the emitted electrons with a simple projection field, without the additional electrostatic lens that is customary in VMI. This can be helpful to simplify experiments or allow them to fit in tight spaces. A smaller ionization region also reduces the ionization time, with potential benefits for time resolution. With a different detector technology, e.g., a delay-line readout, single-shot imaging at high repetition rates might also become feasible. Furthermore, intense standing waves demonstrated in the present setup can lead to diffraction of electrons by the Kapitza–Dirac effect [38,39], a potential pathway for coherent control over electron wave packets.

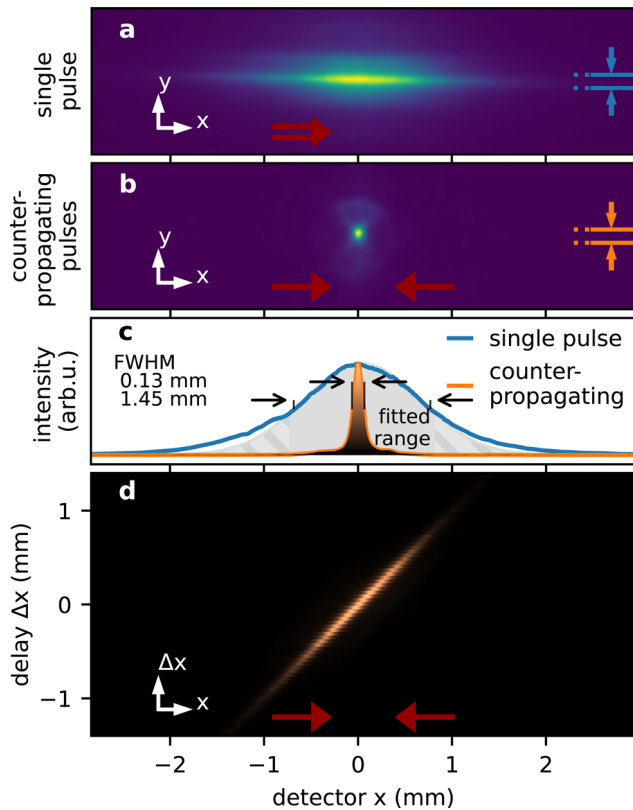


Fig. 3. Electron-detector images of (a) a single pulse and (b) counter-propagating pulses using the *position-imaging* electrode settings. Dark red arrows indicate the light propagation directions and blue (orange) lines show the integration region. (c) Summed counts of the two illumination geometries shown in (a) and (b). Arrows show the full width at half maximum (FWHM) of the Gaussian fits to the peaks. (d) Summed counts for different delays introduced in one optical arm.

Funding. European Metrology Programme for Innovation and Research (20FUN01 TSCAC, 23FUN03 HIOC); Max-Planck-RIKEN-PTB-Center for Time, Constants and Fundamental Symmetries; Max-Planck-Gesellschaft.

Acknowledgment. We thank the fine-mechanics workshop at MPIK led by Thorsten Spranz for the excellent manufacturing of our experimental apparatus, the divisional mechanical workshop led by Christian Kaiser for the prompt support at the laboratory, and our engineering-design office headed by Frank Müller for their help.

Disclosures. The authors declare no conflicts of interest.

Data availability. Data underlying the results presented in this paper can be obtained from the authors upon reasonable request.

REFERENCES

- M. Ferray, A. L'Huillier, X. F. Li, *et al.*, *J. Phys. B: At., Mol. Opt. Phys.* **21**, L31 (1988).
- X. F. Li, A. L'Huillier, M. Ferray, *et al.*, *Phys. Rev. A* **39**, 5751 (1989).
- A. L'Huillier and P. Balcou, *Phys. Rev. Lett.* **70**, 774 (1993).
- P. B. Corkum, *Phys. Rev. Lett.* **71**, 1994 (1993).
- M. Lewenstein, P. Balcou, M. Y. Ivanov, *et al.*, *Phys. Rev. A* **49**, 2117 (1994).
- T. Pfeifer, M. J. Abel, P. M. Nagel, *et al.*, *Chem. Phys. Lett.* **463**, 11 (2008).
- E. Goulielmakis, Z.-H. Loh, A. Wirth, *et al.*, *Nature* **466**, 739 (2010).
- J. Itatani, J. Levesque, D. Zeidler, *et al.*, *Nature* **432**, 867 (2004).
- M. Lein, *Phys. Rev. Lett.* **94**, 053004 (2005).
- S. Baker, J. S. Robinson, C. A. Haworth, *et al.*, *Science* **312**, 424 (2006).
- B. J. Whitaker, *Imaging in Molecular Dynamics: Technology and Applications* (Cambridge University Press, 2003).
- D. H. Parker and A. T. J. B. Eppink, *J. Chem. Phys.* **107**, 2357 (1997).
- D. W. Chandler and P. L. Houston, *J. Chem. Phys.* **87**, 1445 (1987).
- T. Remetter, P. Johnsson, J. Mauritsson, *et al.*, *Nat. Phys.* **2**, 323 (2006).
- J. Mauritsson, P. Johnsson, E. Mansten, *et al.*, *Phys. Rev. Lett.* **100**, 073003 (2008).
- Y. Huismans, A. Rouzee, A. Gijsbertsen, *et al.*, *Science* **331**, 61 (2010).
- G. Sansone, F. Kelkensberg, J. F. Pérez-Torres, *et al.*, *Nature* **465**, 763 (2010).
- S. Zherebtsov, T. Fennel, J. Plenge, *et al.*, *Nat. Phys.* **7**, 656 (2011).
- D. A. Horke, G. M. Roberts, J. Lecointre, *et al.*, *Rev. Sci. Instrum.* **83**, 063101 (2012).
- D. Pengel, S. Kerbstadt, D. Johannmeyer, *et al.*, *Phys. Rev. Lett.* **118**, 053003 (2017).
- S. Kerbstadt, K. Eickhoff, T. Bayer, *et al.*, *Nat. Commun.* **10**, 658 (2019).
- J. Nauta, J.-H. Oelmann, A. Ackermann, *et al.*, *Opt. Lett.* **45**, 2156 (2020).
- D. M. Villeneuve, P. Peng, and H. Niikura, *Phys. Rev. A* **104**, 053526 (2021).
- M. Wollenhaupt, M. Krug, J. Köhler, *et al.*, *Appl. Phys. B* **95**, 647 (2009).
- M. Weger, J. Maurer, A. Ludwig, *et al.*, *Opt. Express* **21**, 21981 (2013).
- D. Townsend, M. P. Minitti, and A. G. Suits, *Rev. Sci. Instrum.* **74**, 2530 (2003).
- J. J. Lin, J. Zhou, W. Shiu, *et al.*, *Rev. Sci. Instrum.* **74**, 2495 (2003).
- J. Ullrich, R. Moshhammer, R. Dörner, *et al.*, *J. Phys. B: At., Mol. Opt. Phys.* **30**, 2917 (1997).
- R. Dörner, V. Mergel, O. Jagutzki, *et al.*, *Phys. Rep.* **330**, 95 (2000).
- A. Vredenborg, C. S. Lehmann, D. Irimia, *et al.*, *ChemPhysChem* **12**, 1459 (2011).
- A. T. J. B. Eppink and D. H. Parker, *Rev. Sci. Instrum.* **68**, 3477 (1997).
- P. Agostini, F. Fabre, G. Mainfray, *et al.*, *Phys. Rev. Lett.* **42**, 1127 (1979).
- R. W. P. Drever, J. L. Hall, F. V. Kowalski, *et al.*, *Appl. Phys. B* **31**, 97 (1983).
- J.-H. Oelmann, "Highly nonlinear light-matter interaction using cavity-enhanced frequency combs," Ph.D. thesis, Heidelberg University, Heidelberg, Germany (2023).
- J.-H. Oelmann, T. Heldt, L. Guth, *et al.*, *Rev. Sci. Instrum.* **93**, 123303 (2022).
- D. A. Dahl, *Int. J. Mass Spectrom* **200**, 3 (2000).
- R. R. Freeman, P. H. Bucksbaum, H. Milchberg, *et al.*, *Phys. Rev. Lett.* **59**, 1092 (1987).
- P. L. Kapitza and P. A. M. Dirac, *Math. Proc. Cambridge Philos. Soc.* **29**, 297 (1933).
- K. Lin, S. Eckart, H. Liang, *et al.*, *Science* **383**, 1467 (2024).

4 Prospects of strong standing waves for Kapitza-Dirac experiments

The last Publication 3.4 described ATI of xenon in a standing wave. This special kind of light does not only alter the intensity distribution in the focal volume but it also influences the electrons after ionization. The electrons are diffracted from the light grating, a phenomenon called the Kapitza-Dirac effect. This chapter will highlight the potential of the experiment to study this effect with yet unpublished experimental observations.

4.1 High-intensity Kapitza-Dirac effect in the literature

There was a very interesting experiment in 1988 by Bucksbaum *et al.* [150] which is similar to the setup in Publication 3.4. Electrons are ionized from xenon atoms in a standing wave formed by two 100 ps laser pulses as depicted in Fig. 4.1 a. After ionization, the photoelectrons diffract from the ponderomotive potential of the standing wave, resulting in two distinct peaks, as can be seen in Fig. 4.1 c. Due to the intensities of 80 TW/cm^2 the peaks are separated by ~ 1000 photon recoils, which is the reason why the authors called their work the "High-intensity Kapitza-Dirac effect". The observation could be reproduced by theory, calculating classical electron trajectories, as shown in Fig. 4.1 d. The electrons are ionized at the points of highest field intensity and then oscillate in the ponderomotive potential between the antinodes until they can escape transversely from the focus. Comparable effects have been observed in the diffraction of atoms with strong light fields, which was termed channeling [151]. Classically, the phenomenon can also be understood as rainbow-scattering [139].

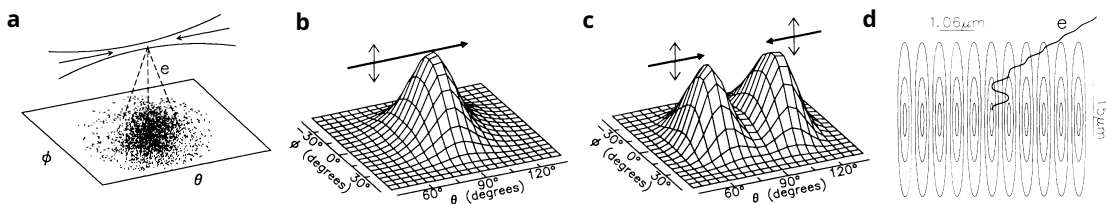


Figure 4.1: Pioneering experiment by Bucksbaum *et al.* measuring MPI of xenon in a 100-ps standing wave [150]. a Experimental setup in which photoelectrons resulting from a standing wave are detected on a screen. b Electron angular distribution for electrons with final energies between 9 eV to 12 eV for a single pulse with a peak intensity of $I_{\text{max}} \sim \text{TW/cm}^2$. c The distribution for a standing wave, showing the Kapitza-Dirac effect. d Calculated classical trajectory showing an oscillation until the electron drifts out of the focus. Reprinted figure with permission from [P. H. Bucksbaum, D. W. Schumacher, and M. Bashkansky, *Physical Review Letters*, 61, 1182, 1988]. Copyright (1988) by the American Physical Society.

In a recent work by Lin *et al.* [62] with a similar setup as Bucksbaum *et al.*, but with two pairs of ultrashort pulses, the authors were able to study the time-resolved Kapitza-Dirac effect, further opening the way to control the electron phase for interferometry.

4.2 State-resolved high-intensity Kapitza-Dirac effect

Reproducing the results of Bucksbaum *et al.* [150] with a 200-fs laser is not trivial, since pulse are too short for the electrons to reach the neighboring antinode. Strongly chirped pulses do not have the necessary intensity for ionization in the 100-MHz setup. As a workaround, a misaligned grating compressor is used that compresses the main pulse to 200 fs for ionization, but leaves a long residual fraction that results in a pedestal pulse in the picosecond range to deflect the electrons.

Figure 4.2 shows the VMI images of xenon MPI in a standing wave with a pedestal pulse present. For the highest recorded intensity of $I_{\max} = 29 \text{ TW/cm}^2$ two distinct vertical lines are visible, breaking the cylindrical symmetry of the electron distribution. As a consequence, the three-dimensional photoelectron angular distribution (PAD) can no longer be obtained from the projection by an inverse Abel transformation. To assign these two vertical lines, similar to the observation in [150], to the standing wave, a traveling wave image is depicted in Fig. 4.2 **c**. Due to the absence of the interference effect explained in the Publication 3.4, the maximum intensity is halved for the same total power. A VMI image with reduced laser power in the counter-propagating pulses is shown in Fig. 4.2 **b**, allowing for a direct comparison between standing and traveling waves at approximately the same intensity. At this intensity, the vertical lines remain visible with reduced contrast for ionization in a standing wave, but they are absent for ionization in a traveling wave. Intermediate states, also known as Freeman resonances, play a significant role in ionization at this intensity [109, 110, 152]. The central region of the energy-calibrated PAD, displayed in Fig. 4.2 **d**, and **e** shows several resonances in four ATI rings. The main resonances correspond to the 5g, 6g and 7g states similar to Fig. 7 of Publication 3.2. The intensities at which these states become resonant due to the AC Stark effect are shown in Fig. 4.2 **f**.

The Freeman resonances allow an intrinsic intensity calibration of the observed double splitting from the high-intensity Kapitza-Dirac effect. The yellow line indicating the splitting in Fig. 4.2 **d** reproduces the ATI rings and shows that the splitting is strongly energy dependent. At the 5g resonance the signal peaks at a longitudinal momentum of about $130 m_e \text{ km/s}$, while the electrons originating from the 6g and 7g resonances have less momentum. This resolves the intensity dependence of the effect, since the intensity to reach the 5g resonance is the highest. The smallest momentum splitting of $\sim 100 m_e \text{ km/s}$ is observed for electrons with a multiple of the photon energy. These electrons originate from the channel closing [153] at 10 TW/cm^2 . At this intensity, the ponderomotively shifted ionization threshold of xenon is equal to the energy of 11 photons. This appears to be the lowest intensity with substantial ionization yield in this measurement. Remarkably, the electrons from the channel closing do not produce a visible signal in the integrated counts. However, the splitting reveals their existence. In this sense, the Kapitza-Dirac effect can be used as a tool to study ionization dynamics, as it provides a measure of the local intensity at the moment of ionization.

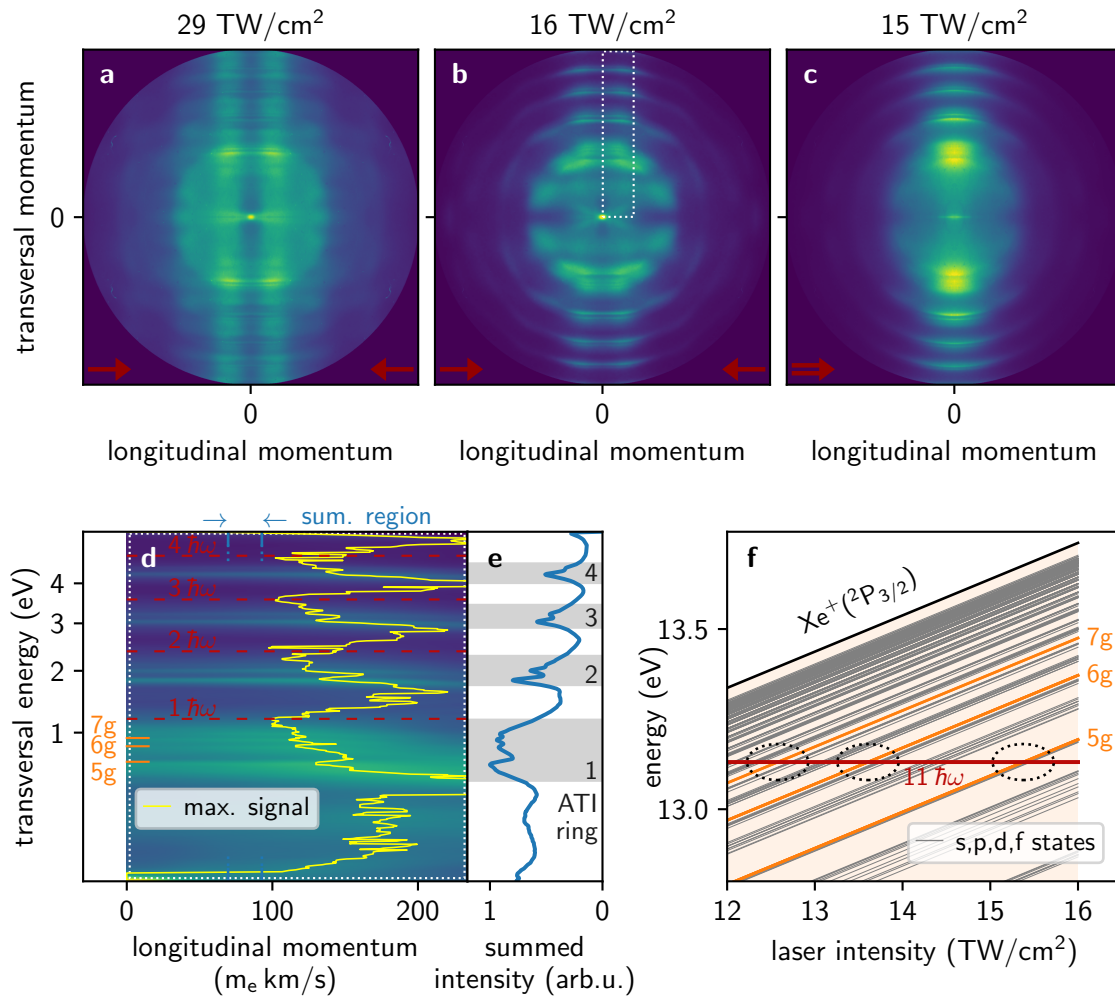


Figure 4.2: VMI images of xenon with a picosecond pedestal pulse revealing the high-intensity Kapitza-Dirac effect. **a** and **b** show ionization in standing waves; **c** with a traveling wave. The red arrows indicate directions of the laser beams. All images are symmetrized along both axes. Note that the two vertical lines are not present in **c**. A zoom on the dotted rectangle is shown in **d**. The image is smoothed with a 5-pixel Gaussian in the longitudinal direction. The yellow line indicates the momentum of the maximum signal for each transverse energy. The energy and momentum calibration is based on fitting the 6g resonance in the first three ATI rings. The red dashed lines mark the photon energies, corresponding to electrons ionized at a channel closing. **e** The signal integrated over the marked summation region with assigned rings. **f** Energy diagram of xenon Rydberg states shifting with the ponderomotive potential, adapted from Fig. 8 in Publication 3.2. The most dominant resonances with the 5g, 6g and 7g states are marked with dotted ellipses.

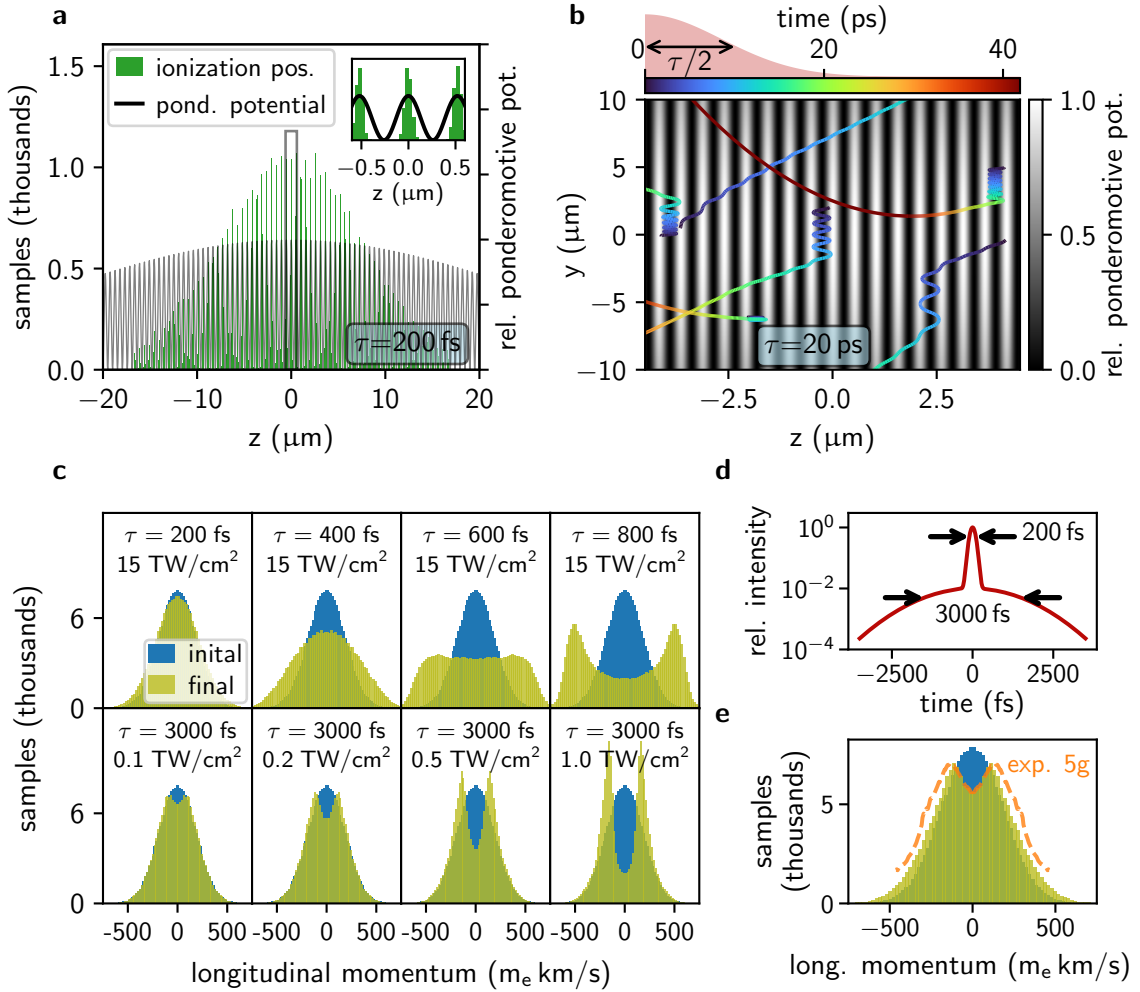


Figure 4.3: Monte Carlo simulation of classical electron trajectories in standing waves. **a** 100 000 samples of ionization positions are randomly drawn from a three-dimensional (z , y , t) multivariate distribution for a pulse of FWHM-length of $\tau = 200$ fs, assuming a 12th-order nonlinearity. The inset shows a zoom on the central antinode indicated by the gray box. **b** Six example trajectories of electrons ionized in a standing wave with a pulse length of $\tau = 20$ ps and maximum intensity $15 \text{ TW}/\text{cm}^2$. **c** Comparison of initial and final longitudinal momentum distributions for different laser parameters. The initial energy at ionization is assumed to be normally distributed with a width of 100 meV in the longitudinal direction together with a random transverse component between 0 and 2 eV . The electrons are propagated for 5τ . **d** Pulse shape consisting of a 200 fs short pulse with a 3000 fs long pedestal at 1% of the maximum intensity of $15 \text{ TW}/\text{cm}^2$, resulting in the distribution shown in **e**. The dashed orange line corresponds to the experimentally measured electron momenta for the $5g$ resonance (compare Fig. 4.2). More details on the calculations can be found in the text.

4.2.1 Classical electron trajectories in standing waves

Similar to the work of Bucksbaum *et al.* [150], the experimental results can be understood with classical electron trajectories. Here, they are integrated in two dimensions with the explicit Runge-Kutta method of order 4(5) [154]. The time-dependent ponderomotive potential is determined from two counter-propagating pulses, forming a standing wave with a transversal Gaussian beam waist radius of 25 μm . The gradient along the laser direction z is calculated numerically and the gradient in transverse direction y is derived analytically. In y -direction an additional extraction field of 25 mV/ μm mimics the experimental conditions.

Figure 4.3 shows the results of the classical Monte Carlo simulations. The ionization positions and times for the initial conditions, depicted in Fig. 4.3 **a**, are sampled from a three-dimensional multivariate distribution. The nonlinearity of the ionization process is assumed to be of order 12, corresponding to the minimum photon number of xenon MPI at 15 TW/cm², which results in ionization occurring only at the antinodes. Figure 4.3 **b** shows six example trajectories in the regime of a long 20-ps pulse. Analogous to Fig. 4.1 most trajectories are trapped by the ponderomotive potential, oscillating in the nodes of the standing wave with a period of ~ 2 ps until they eventually escape. The influence of the extraction field is low and can only be seen for the slowest electrons at times > 40 ps.

The maximum intensity in the antinodes of 15 TW/cm² corresponds to a ponderomotive potential of $U_p = 1.45$ eV. According to Eq. (2.9), the spatial structure of the potential along the axis is

$$U(z) = U_p |\cos(kz)|^2. \quad (4.1)$$

Taking the first term of the Taylor expansion in a node, e.g. at $z' = z - \pi/(2k)$, yields $U(z') = U_p k^2 z'^2$. A comparison with a harmonic oscillator with the potential $U = 1/2 m \omega_0^2 z^2$ gives us the maximum oscillation frequency $w_0 = \sqrt{2U_p m^{-1}} k$ for small amplitudes, corresponding to the minimum period $T_{\min} = 2\pi \omega_0^{-1} \approx 1.46$ ps. Slow electrons starting near an antinode need at least $T_{\min}/4$ to reach the first node. If an electron is ionized at the peak of a Gaussian pulse with a FWHM width of τ , the light intensity and thus the ponderomotive potential after τ is strongly reduced to $e^{-4 \ln 2} = 1/16$. This estimation shows that pulses with $\tau < T_{\min}/4$ do not allow for a classical electron oscillation. This can also be seen in the calculated electron momenta after the interaction as shown in Fig. 4.3 **c**. The histograms are symmetrized because the simulation has no preferred direction. For the pulses with $\tau \leq 400$ fs, the momentum distribution is broadened only because the electrons gain more energy as they move down the potential hill at the antinode of their ionization. For longer pulses, a double peak structure is formed, similar to the electron distribution in [150] using 100-ps pulses. The intensity of the pulse alters the contrast and the separation of the two peaks. At an intensity of 15 TW/cm², which corresponds to the measurement in Fig. 4.2, the final momentum would peak at $\sim 500 m_e k\text{m/s}$. Since the experimental pulses with $\tau = 200(20)$ fs [49] are too short for oscillations and the observed splitting is much smaller, it makes sense to attribute the experimental double peak to a longer, weaker pedestal pulse. Fig. 4.3 **d** shows an additional pedestal pulse with $\tau = 3$ ps and with 1% of the maximum intensity of the main pulse, corresponding to $\sim 13\%$ of the pulse energy in the pedestal. This combination can reproduce the experimental momentum distribution very well, as depicted in Fig. 4.3 **e**.

The above analysis has shown that the high-intensity Kapitza-Dirac effect can be well modeled classically for picosecond pulses. For pulses so short that the ionized electrons

do not reach the ponderomotive potential around the neighboring antinode, this model predicts only a smearing of the observed momentum distribution. The question of whether there are observable effects beyond this prediction for ultrashort pulses is discussed in the following section.

4.3 Observed effects of a standing wave on ATI for femtosecond pulses

Addressing the question from the previous section, the data presented below results from measurements where the compressor is "carefully" aligned. This should ensure a high contrast between the main 200-fs pulse and any residual longer components.

Figure 4.4 shows a comparison between the ATI electron momenta for a traveling and a standing ionizing field. The intensity range covers both the MPI regime, where the emission is dominated by the ring-shaped ATI peaks, and the tunnel ionization regime with a nearly homogeneous momentum distribution along the laser polarization. The maximum intensities are calculated from the transmitted light, assuming a waist radius of $22\ \mu\text{m}$. The necessary extrapolation of the photodiode calibration results in an uncertainty of approximately 25 % in the absolute intensity values.

Although there are no clear vertical lines visible, which are a distinct signal of the high-intensity Kapitza-Dirac effect in Fig. 4.2, the images for emission in standing waves differ strongly from the emission in traveling waves. In the following, these differences are discussed in more detail. First, in a standing wave there are much fewer counts for the same intensity. This can be explained by the strongly reduced ionization volume. As pointed out in the Publication 3.4, the intensity envelope along the propagation axis shrinks from twice the Rayleigh length $2z_R = 3\ \text{mm}$ to the spatial pulse overlap of $\tau_{\text{FWHM}}c = 60\ \mu\text{m}$. The \sin^2 substructure of the standing wave has an additional influence. Assuming that due to the high nonlinearity of the MPI process, ionization only occurs near antinodes at intensities of $> 0.9I_{\text{max}}$, the ionization volume shrinks to $1 - 2/\pi \arcsin(\sqrt{0.9}) \approx 20\%$. In total, this results in a count rate reduced by a factor of 250.

A second difference between the two pulse geometries is a feature present only in intense standing wave ionization, best seen at the bottom of Fig. 4.4 **b**ⁱⁱⁱ, marked by a dotted rectangle. The electron momenta are distributed in horizontal lines along the propagation direction. This might correspond to the broadening of an initially narrow momentum distribution due to the ponderomotive acceleration away from the antinodes as calculated classically in Fig. 4.3. A third effect in standing waves, visible for the two highest intensities, is a small horizontal splitting of the central spot.

For a more detailed analysis of the last two effects, Fig. 4.5 shows a zoom on the momentum distributions at the highest intensities. The gain of the microchannel plate (MCP) detector and the camera is reduced for these measurements to ensure low noise.

For traveling waves, the ionization region may extend significantly along the propagation axis if the intensity is high enough to fully ionize all xenon atoms in the focus. A large ionization volume leads to aberrations in the momentum imaging and could explain why the perpendicular polarization does not result in a circular momentum pattern but in a broad line elongated along the propagation axis.

For standing waves, the longitudinal momentum distribution in the TI regime is not only a single broad peak, but it shows a substructure. For small transversal momenta ($p_t < 100\ \text{m}_e\text{km/s}$) along the polarization axis, a double peak appears with a minimum

4.3 Observed effects of a standing wave on ATI for femtosecond pulses

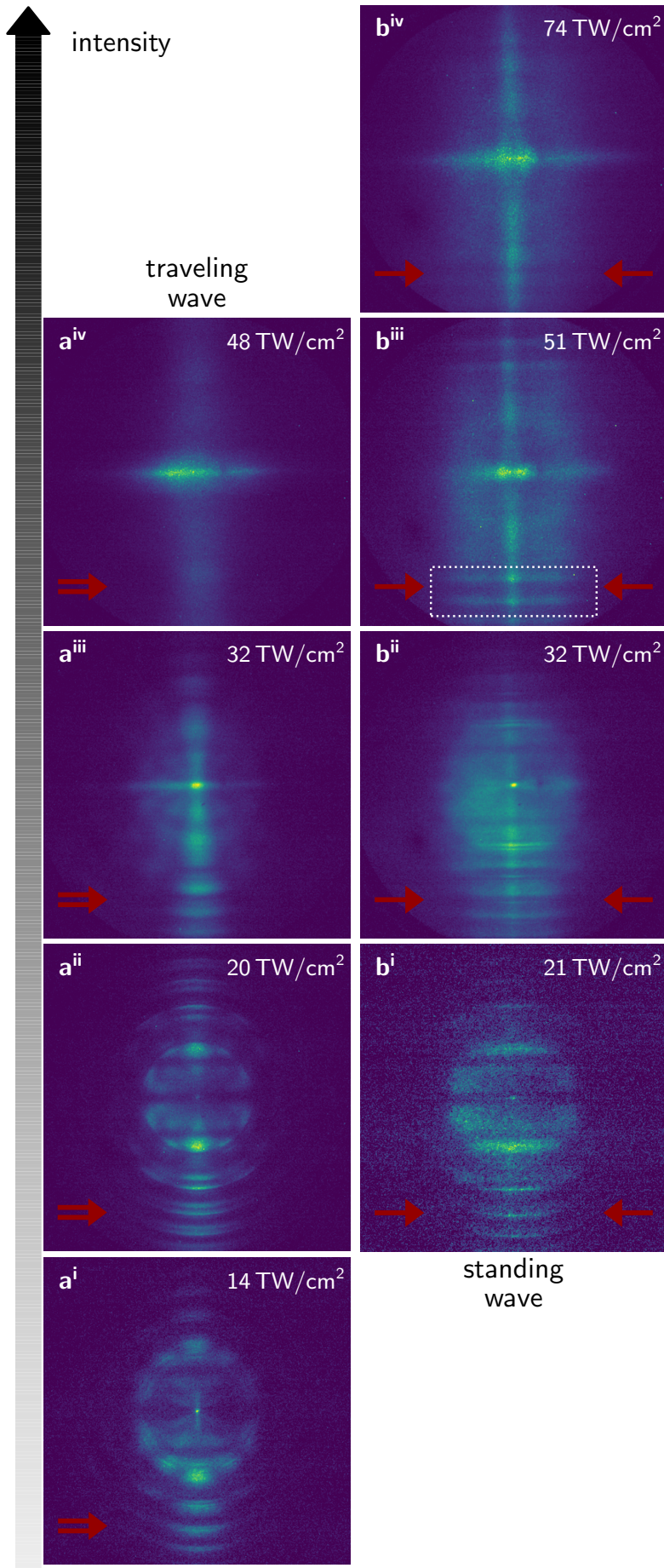


Figure 4.4: Comparison of ATI in xenon triggered by traveling (a) and standing waves (b) for different laser intensities. The red arrows indicate the propagation direction and the distribution of the total light energy in one or two pulses. The dotted rectangle highlights a feature described in the text.

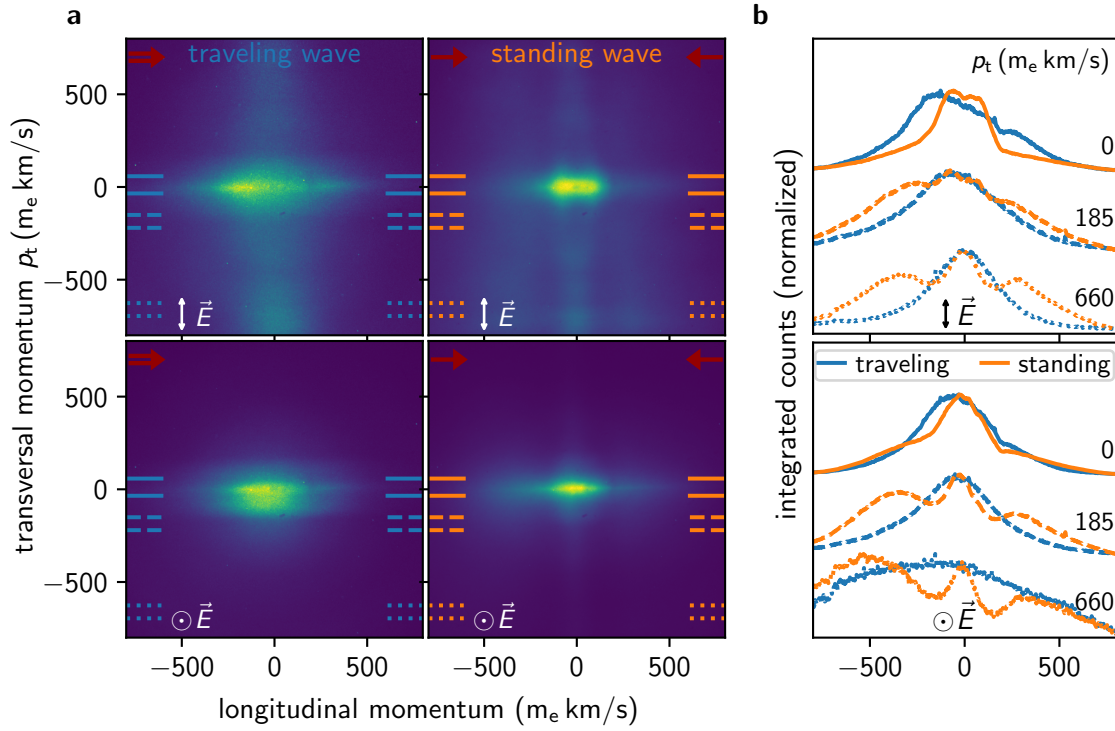


Figure 4.5: **a** Momentum distributions of slow electrons resulting from tunnel ionization with traveling waves (left column) and standing waves (right column). For the upper row the light polarization is aligned parallel to the detector, for the lower row the polarization is pointing towards the detector. Blue and orange lines indicate the integration regions for the lineouts shown in **b**. They correspond to transversal momenta of $0 m_e \text{ km/s}$, $185 m_e \text{ km/s}$ and $660 m_e \text{ km/s}$. The maximum intensity is $\sim 40 \text{ TW/cm}^2$ for traveling, and $\sim 70 \text{ TW/cm}^2$ for standing waves. Note the splitting of the momentum distributions for standing waves depending on the transversal momentum.

at $p = 0$. However, for higher p_t the gap closes and a triple peak pattern appears. This structure does not result from a specific atomic resonance and a subsequent high angular momentum electron emission as for lower intensities, since it is the same for the orthogonal projection depicted in the lower row of Fig. 4.5. Classical electron trajectories also fail to reproduce this result, even when potential pedestal pulses are taken into account.

In conclusion, the ionization of xenon with ultrashort standing waves leads to an interesting modulation of the longitudinal momentum distribution, which changes as a function of the transverse momentum. The origin of this is beyond a classical ponderomotive picture and remains to be determined.

4.3.1 Influence of the ionization position on the electron momentum

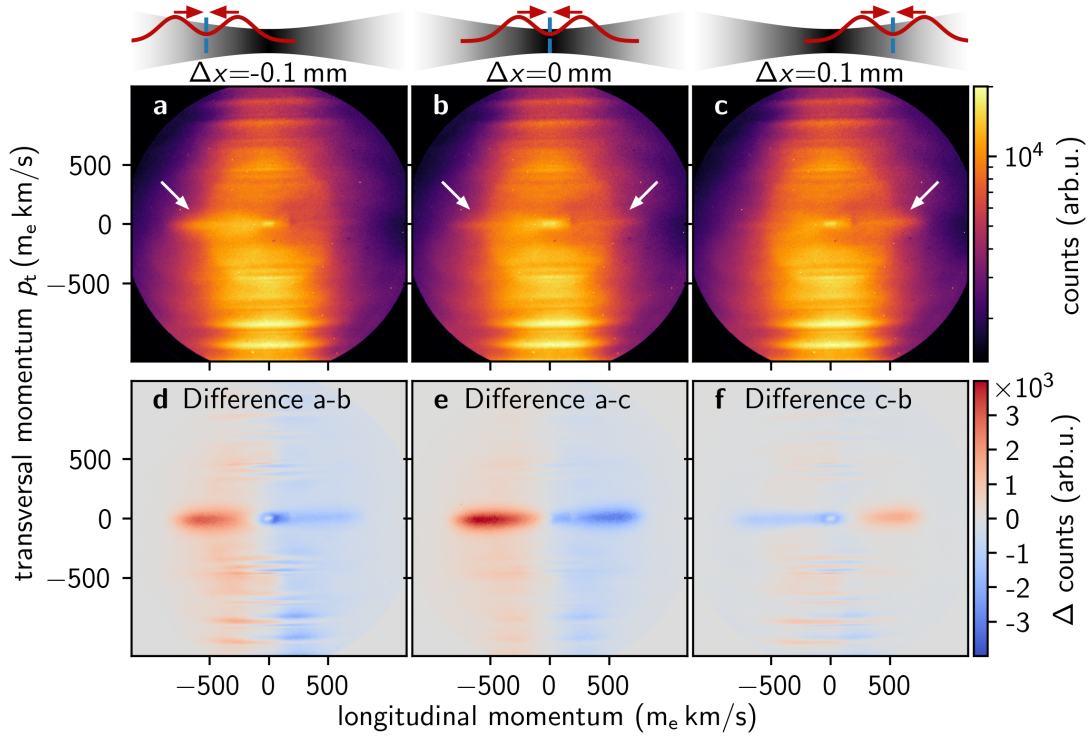


Figure 4.6: Dependence of the ionization position on the ATI signal. **a-c** Electron momentum distributions in logarithmic color scale for different ionization positions shown at the top. The ionization position relative to the focus (gray color scale) is changed by introducing a delay in one of the optical branches. For clarity, the Rayleigh length in the illustration has been reduced by a factor of 200. The dominant feature is marked with white arrows. **d-f** Relative changes depending on the ionization position. The polarization is aligned parallel to the detector and the maximum intensity is $\sim 50\text{TW}/\text{cm}^2$.

By introducing a delay in one of the optical branches, the position of the standing wave and thus the ionization position can be shifted away from the focus. The shifts studied are so small that all position dependent aberrations of the VMI setup can be neglected. Figure 4.6 examines the resulting electron momentum distributions. There is a dominant feature at $p_t = 0$, marked with white arrows, that strongly favors the side

of the ionization. The differences shown in Fig. 4.6 **d-f** also reveal a small asymmetry at higher transversal momenta, but this is much less pronounced. The images **d** and **f** show additionally distinct horizontal lines at higher momenta, because the maximum intensity is slightly higher for $\Delta x = 0$. This leads to a different ponderomotive shift of the ATI peaks.

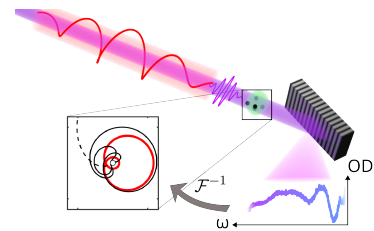
In a naive picture, the dominant asymmetry feature at $p_t = 0$ simply arises because the electrons are pushed away from the higher ponderomotive potential at the focus. However, one has to consider, that the electrons cannot even move $\lambda/4$ within the pulse duration. Therefore, the gradient resulting from the node-antinode modulation should dominate the gradient resulting from the Rayleigh length. This can be seen from a simple argument. While it takes only 130 nm for the ponderomotive potential near an antinode to decrease by half, the Rayleigh length is five orders of magnitude larger. Due to the spread of the ionization positions at an antinode, scattering to the left or to the right should have nearly the same probability, which is in strong disagreement with the good contrast in the experiment.

The explanation for this feature remains an open question. Possible pathways are long-lived Rydberg atoms that could experience more than one standing wave ($t > 10$ ns), or a process that selects electrons with ionization positions exactly at an antinode. It will take further experimental and theoretical efforts to find an explanation for this observation.

5 Concluding discussion

This thesis investigates the nonlinear response of electrons to intense light with different experiments aimed at various length and time scales. The preceding two chapters have presented the published and unpublished results of this thesis. This concluding chapter synthesizes these findings, highlights the connections between them, assesses the advancements over existing research, and proposes new questions that could be addressed using similar methods.

5.1 Measuring electron dynamics at the atomic scale



The fastest time scale studied in this work is given by the period of the NIR light. On this scale, the atomic electrons have not yet escaped the influence of the parent ion, even if they have gained enough energy to do so. Publication 3.1 explores the dynamics of these quasi-free electrons, which can be driven back to their parent ions by a strong NIR pulse, a phenomenon known as recollision.

An all-optical method to study electron recollision

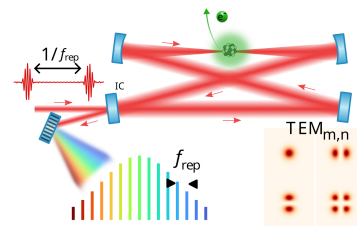
To capture the electron dynamics in the vicinity of an ion, a few-cycle NIR pulse is paired with an XUV pulse of higher energy and even shorter duration. The purpose of the XUV pulse is twofold. First, it elevates the electron energetically from the ground state to the continuum in a delta-like excitation and is therefore a very good trigger to start the clock. Second, the NIR-driven electron dynamics are imprinted on the XUV field by the dipole response of the system. This makes it possible to recover information about the electron trajectories using an all-optical method simply by measuring the absorption spectrum in the XUV. Thus, this new technique provides an alternative way to study electron recollision in addition to other established methods that measure the momenta of the ionized electrons [116, 155]. Naturally, the question arises whether it is possible to simultaneously measure both the optical response and the momenta of the charged fragments in order to take full advantage of the complementary methods. This is challenging because transient absorption spectroscopy requires significantly higher target densities, which are in conflict with the geometry and vacuum constraints of electron spectrometers. However, Hu [156] has recently demonstrated the feasibility of a combined measurement, showing that the electron data can be used to accurately determine the absolute time delay between XUV and NIR, which is otherwise difficult in ATAS.

Possible extensions of the method and comparable approaches

For the work of this thesis, we used this new method to experimentally confirm that recolliding periodic orbits lead to a recollision channel for circularly polarized NIR light, which usually drives the electron away in spirals [11, 157]. The recollisions are only possible because the XUV can ionize the helium before the NIR envelope becomes strong, leading to a small drift velocity, while the delay is small enough not to have a strong dispersion of the electron wave packet [158].

For further studies, it would be very interesting to switch from the noble gas helium to molecules. In these systems, the single active electron approximation breaks down and the extended geometry would lead to an electronic response dependent on the molecular orientation. The physics would be similar to experiments using laser-induced electron diffraction (LIED), which is capable of imaging gas-phase molecules [155, 159, 160], but with all-optical detection. Typical LIED experiments use a reaction microscope (REMI) [29] to capture the full 3D kinematics of electrons and ions in coincidence. This is of course much higher-dimensional data than in an all-optical approach, and it remains to be shown how much information can be extracted from the absorption spectra alone. Due to their ability to measure the complete kinematics in a coincidence scheme, REMIs are generally very powerful machines for studying strong-field atom-light interactions. However, they often require long integration times of weeks because of the kilohertz repetition rates of typical femtosecond lasers with pulse energies sufficient for strong-field ionization (~ 0.1 mJ).

5.2 Femtosecond enhancement cavities for MHz-rate strong-field studies



Using the megahertz repetition rates of laser oscillators directly for strong-field experiments is appealing because it decreases the required integration times by many orders of magnitude and thus allows to capture even rare processes with low cross sections or for comparably low intensities [39]. Unfortunately, the technology of stable femtosecond lasers with kilowatt of average power is not yet developed, although there are promising first results [161]. An elegant solution to reach the required intensities is to recycle the light in femtosecond enhancement cavities (see Subsec. 2.2.2), as first demonstrated to generate frequency combs in the XUV [40, 41].

Advantages of intra-cavity experiments

Passive enhancement in a cavity is the key optical technique for the results on ATI of xenon in this thesis. In addition to the increased intensity, there are several other advantages worth noting. First, the intra-cavity light retains its comb structure of well defined frequencies. This is most important for the generation of XUV frequency combs, but it might also be interesting to explore how the spectral structure can be transferred to electrons or if it can be used for multiphoton spectroscopy. However, narrow atomic transitions will not be easy to measure because the AC Stark effect in the intense light field

is orders of magnitude larger than the comb spacing. One potentially promising target is thorium-229, which possesses a nuclear isomer at only ~ 8.2 eV [45]. Since the nucleus is much smaller than the electronic orbitals, this transition is only weakly affected by external fields. Such a nonlinear excitation is not expected to yield the excellent precision of weak XUV light [46], but it could be the first demonstration of a strong-field clock.

Closely related to the comb structure is the high repetition rate of the pulses. This does not only benefit statistics, but can also allow the interaction of a room temperature atomic target with two or more successive coherent NIR pulses. The diffraction features observed in Subsec. 4.3.1 could already be related to such a multiple interaction. Another peculiarity of intra-cavity light is the existence of transverse modes (see Subsec. 2.2.3). The fundamental Gaussian mode allows the highest intensities and is therefore routinely selected. However, it is also possible to couple predominantly into a higher order transverse mode by adjusting the mode matching. This gives the light field at the focus an additional structure that can be exploited in electron diffraction experiments. Recent theoretical work has predicted inelastic electron scattering in a TEM_{01} mode [162].

The cavity is also useful for realizing an intense standing wave. Forward and backward propagating waves share the same mode and misaligned incoupling light can not resonantly excite other transversal cavity modes since they are shifted in frequency. This means that the foci of both pulses overlap perfectly and the angle between their wavevectors is exactly 180° . The cavity also helps to minimize the power of the beam returning to the oscillator when working with a standing wave. Without a cavity, the pulse energy available at the focus would be reflected back through the amplifier towards the oscillator. With a cavity, this energy is approximately reduced by the enhancement factor, significantly reducing the load on the optical isolators.

Challenges of cavity operation

All advantages of the cavity come at a price, namely higher technical complexity and sensitivity to noise. For maximal operating time, the length of the cavity needs to be locked to the repetition rate of the frequency comb. Any acoustic vibrations or noise of the comb itself reduce the quality of the lock. Alternatively, the length of the cavity can be scanned over the resonance, but this slows down the acquisition rate due to the small duty cycle.

The high intra-cavity power levels also impose significant stress on the cavity mirrors. Their coatings can easily be damaged [163] or contaminated [164], leading to a strong reduction of the circulating power. Maintaining a constant background pressure of an oxygen-ozone mixture has been shown to prevent degradation [164, 165], but this is not feasible during operation of the MCP detector. However, flushing the chamber with such a mixture between measurements has been helpful in reducing degradation effects.

Additionally, spatial requirements must be considered, as the resonance condition links the cavity length l to the repetition rate of the frequency comb by $l = c/f_{\text{rep}}$. For a repetition rate of $f_{\text{rep}} = 100$ MHz, this results in $l \sim 3$ m, necessitating a sufficiently large vacuum chamber. Mirrors can be used to fold the beam path several times, at the price of added complexity and cost. The high repetition rate also makes demands on the detector technology. Coincidence schemes are no longer suitable because of the potentially high count rates. The time of flight of the ions is several orders of magnitude larger than the delay between two consecutive pulses.

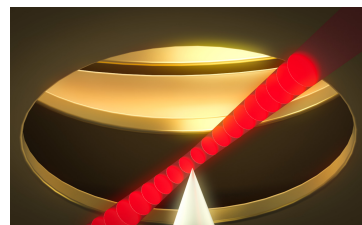
5.3 A velocity-map imaging spectrometer for intra-cavity strong-field experiments



Publication 3.2 presents a VMI spectrometer specifically designed to meet the requirements of the optical setup. The MCP detector with the subsequent fluorescence screen can handle count rates in the order of f_{rep} , but can also be operated to detect single counts with sufficiently high amplification voltages applied. The VMI spectrometer is compact by design and requires very little manual positioning to ensure excellent alignment. Importantly, the spectrometer is shielded with μ -metal to ensure low distortion from external electromagnetic fields. This allows the extraction voltages to be reduced even below 1 V/cm to study very slow electrons. First measurements with these low extraction fields are performed, but their discussion is beyond the scope of this thesis.

The publication also demonstrates the tomographic reconstruction of a PAD, which is only possible because the cavity is designed to be polarization insensitive. While the PAD for xenon with a single linearly polarized pulse can be calculated with the inverse Abel transformation, the tomographic technique is crucial for electron distributions without cylindrical symmetry [149]. This is for example the case for electron vortices [166] and also for a Kapitza-Dirac-diffracted electron distribution. In fact, even at low light intensities, where the splitting studied in Sec. 4.2 was not a dominant feature, the inverse Abel transformation failed and produced negative values near the central axis, indicating that the cylindrical symmetry was broken.

5.4 Studying nanometric objects and crystal structure with intra-cavity standing waves



In Publication 3.3, the crystallographic structure of the tip apex is revealed in the momentum distribution of the emitted electrons, by scanning the phase of the standing wave. The essential feature of the VMI technique to image the momentum of charged particles independent of their position, is not necessary because the nanotip is so small. Placing the tip and its holder between the repeller and the extractor electrode also perturbs the VMI field configuration. However, this study benefits from the good shielding and the nanometric xyz-positioning of the entire spectrometer assembly, including the nanotip, relative to the focus. Compared to the first publication, the relevant length scale is no longer the size of an atom, but rather the size of the crystal structure.

Nanometric imaging methods

In general, there are many techniques to achieve nanometer resolution imaging. The most common methods include diffraction, which is applicable when the de-Broglie wavelength

of the probe is smaller than the object, as is the case with energetic electrons in transmission electron microscopy (TEM) [167]. Alternatively, imaging can be performed by scanning a small probe over the sample. This probe can be an electron beam focus, as in scanning electron microscopy (SEM) [168], a laser focus, as in stimulated emission depletion (STED) microscopy [169], or a nanotip, as in scanning tunneling microscope (STM) [170]. Another method useful to image sharp tips is the projection of electrons, as in field-emission microscopy (FEM) [171], or ions, as in field-ion microscopy (FIM) [172]. The approach presented is primarily related to FEM, but the emission is optically triggered by a scanned standing wave. Interestingly, the concept of enhanced optical confinement along the propagation axis by counter-propagating light was also introduced in confocal imaging as 4π microscopy [173] or standing-wave fluorescence microscopy [174]. The exploitation of a nonlinear process, here photofield emission (see Subsec. 2.3.3), is another method of improving the resolution that is also practiced in microscopy [175]. Thus, by using the nanometric structure of an intense standing wave with strong axial gradients to nonlinearly probe nanometric samples, Publication 3.3 successfully adapts two microscopy concepts to electron emission experiments. This allows not only to control the emission angle on a nanotip, but also to identify the crystallographic planes with the lowest work functions.

In the future, if the pulse length could be reduced to a few cycles, a single dominant antinode would be obtained. With such a field it would be possible to probe even extended geometries ($<z_R$) like complex metasurfaces unambiguously along the beam propagation direction. Another possible line of research is to use the field enhancement of a nanotip geometry to study nearby gas atoms. Electron emission will probably always dominate from the solid-state tip, but an ion signal could originate from ionized gas. This can be easily measured by changing the polarity of the electrodes, allowing the VMI to detect ions instead of electrons.

Cavity effects on electron emission from tips

An interesting question is how a cavity affects these photofield emission experiments. The main effect of a cavity is the enhanced intensity. In principle, however, these high light intensities are not needed because the metal of a nanotip has a much lower work function than typical rare gas ionization thresholds. In addition, nanotips provide an intrinsic field enhancement due to their geometry, and for some materials surface plasmons provide further enhancement. For these reasons pioneering experiments have worked with oscillator power levels [131, 136]. The presented results utilize reduced laser power and position the nanotip at the side of the focus, because intensities exceeding 50 TW/cm^2 , achievable in the cavity focus, will lead to plasma formation and sample damage. But even if one does not want to study the evolution of plasma, there are interesting features of the cavity. First, as discussed above, it is straightforward to obtain structured light, i.e. higher order transverse modes. Second, the high intensities could be used to diffract the emitted electrons by the Kapitza-Dirac effect. In this scenario, a first pulse with polarization along the tip, which is at the side of the focus, triggers an electron emission. A subsequent delayed standing wave with orthogonal polarization, which does not experience the tip enhancement, diffracts the electrons that have moved into the focus. Third, a nanotip inside the cavity mode introduces additional losses and thus reduces the enhancement as a function of the insertion depth.

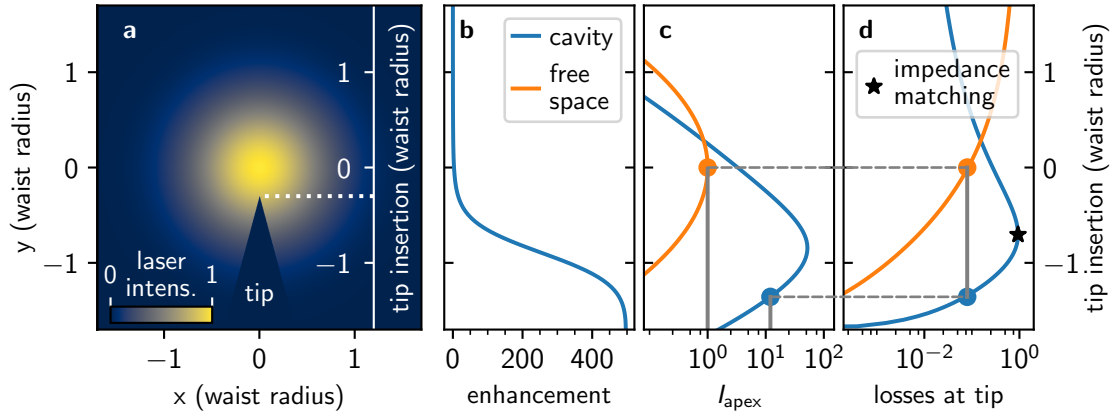


Figure 5.1: Back action of the tip on the cavity. **a** Fundamental Gaussian mode with the shadow of a tip at an exemplary insertion of -0.3 times the waist radius. **b** Calculated cavity enhancement factor (see Subsec. 2.2.1). Relevant parameters are given in the main text. Tip insertion causes additional losses due to its geometric cross section. **c** The intensity at the tip apex depends on the insertion for both cavity and free-space operation. **d** Losses induced by the tip. The gray lines indicate that the intra-cavity intensity at the apex is approximately ten times higher than in free space, given the same losses. The black star shows the position of impedance matching when the round-trip losses are equal to the transmission of the input coupler.

Figure 5.1 numerically explores the relationship between cavity enhancement and tip insertion. The tip opening angle is set to $\alpha = 15^\circ$ and the resonator consists of five highly reflective mirrors $R_{\text{HR}} = 0.9999$ and one input coupler with lower reflectivity $R_{\text{IC}} = 0.993$. The losses are approximated by the geometric cross section of the tip neglecting diffraction. For experiments in free space, it is reasonable to place the tip apex at the focus center, here denoted as tip insertion 0. In contrast, for intra-cavity studies it is better to place the tip further out: The field at the apex is the product of the enhancement factor and the local field strength of the cavity mode, as shown in Fig. 5.1 **c**, with a maximum approximately one waist radius w_0 away from the center. For the chosen parameters, the intensity at this position is 50 times larger than that at the beam center in the free-space case.

This insertion depth of maximum intensity is also close to the point of maximum losses (see Fig. 5.1 **d**). Since the empty cavity is over-coupled, the tip-induced losses can actually improve the impedance matching between the cavity and its driving laser. Losses at the highly reflective mirrors are small, so for impedance matching almost all of the laser power is either absorbed or scattered by the tip, even though it only intercepts the wings of the cavity mode. This should cause very localized heating at the apex, whereas in free-space experiments with the apex in the center of the focus, the weak intensity gradient of the beam heats a larger part of the tip. Furthermore, the cavity can still add an order of magnitude enhancement (marked by gray lines in Fig. 5.1 **c, d**) for an equivalent level of free space losses. Conversely, for the same intensity, the losses at the tip are ten times smaller. These calculations show that intra-cavity experiments allow the study of nanometric tips with a more complex relationship between maximum intensity and effective heating.

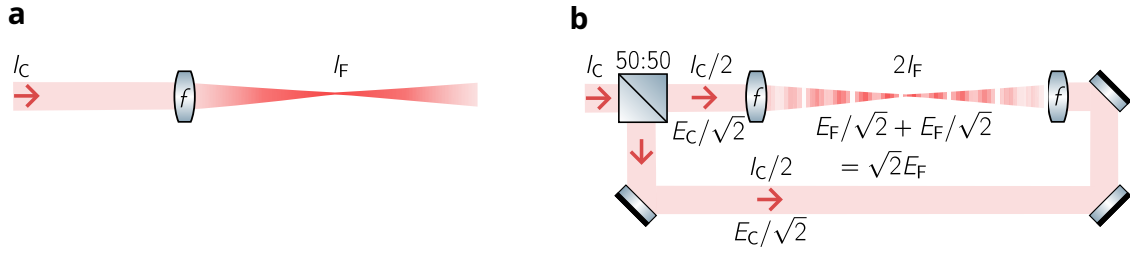
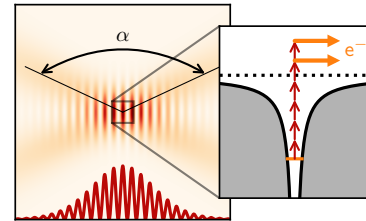


Figure 5.2: Intensity doubling in a standing wave. **a** A collimated beam is focused by a lens with focal length f to maximum intensity I_F . **b** When the beam is split and then superimposed in the opposite direction, the electric fields must be added together, resulting in twice the intensity at an antinode in the focus. For clarity, the delay line is omitted, the node structure is not to scale, and the pulse length is $2f$.

5.5 Standing waves for above-threshold ionization



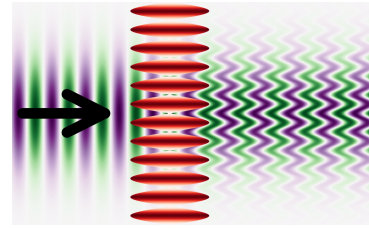
The last Publication 3.4 again uses xenon as a target to study the light-matter interaction in intense standing waves. The relevant investigated length scale is extended to the size of the laser pulse given by $l = c\tau$, with τ its duration.

Due to the nonlinearity of the electron emission, the interaction volume along the beam propagation shrinks from the Rayleigh length to a fraction of the overlap region. The source size reduction is very advantageous for the measurement of electron momenta because the Einzel lens used for electrostatic focusing in traditional VMI is not necessary anymore, lowering significantly the design constraints.

The second key observation of this publication is the doubling of maximum intensity in a standing wave. According to the superposition principle, it is mathematically straightforward why splitting and then recombining a beam leads to higher peak intensities in the antinodes, as shown in Fig. 5.2. In compensation, destructive interference cancels out the intensity in the nodes, so that the volume of the maximum intensity shrinks, as discussed in Sec. 4.3.

What occurs in the general case of arbitrary crossing angles between two focused beams? For crossing angles $\alpha < 180^\circ$, there is no perfect standing wave, but the intensity calculation is the same when the light is polarized perpendicular to the plane of incidence. It is important, however, that α is greater than the divergence θ of the focused beam, otherwise a coherent superposition of the split beams would again require a beam splitter. From Fourier optics, it follows that two coherently crossing beams produce a sinusoidal modulation in the transverse direction with a periodicity of $\lambda/(2 \sin \alpha/2)$, effectively halving the illuminated area. This phenomenon can also be related to the Étendue principle [176]. If the angle α is large enough to clearly separate the beams, the solid angle of the light reaching the focus doubles, allowing the light to be confined to half the area, resulting in a doubling of intensity.

5.6 Ponderomotive control of slow electron matter waves



Publication 3.4 demonstrates that the experimental setup is capable of producing slow electrons within an intense femtosecond standing wave at a high repetition rate of 100 MHz. This is very promising for experiments that use the ponderomotive potential of a standing wave to diffract electrons, as has been pointed out in Chap. 4. The coupling of free electrons to photons is a promising part of quantum electron optics. In ultrafast TEM, concepts such as photon-induced near-field electron microscopy (PINEM) [177] lead to a combined nanometric spatial and attosecond temporal resolution [55–59], which can even be further enhanced by electron interferometry [60, 61]. With bichromatic fields, ponderomotive scattering allows the broadening of electron spectra to compress electron pulses to attosecond duration [178, 179], electron acceleration [180], or the construction of complex quantum states [181].

While these other works have all obtained results for fast electrons with energies in the order of 100 keV, the peculiarities of slow electrons with energies of a few eV have only recently begun to be investigated theoretically. Studies suggest that slow electrons exhibit distinct quantum characteristics. One reason is the breakdown of the nonrecoil approximation, which results in an effective asymmetry between absorption and emission processes [182]. Additionally, slow electrons should demonstrate quantum effects during scattering at surfaces or within evanescent optical fields [183]. It remains to be demonstrated whether intense intra-cavity standing waves can also contribute to this emerging field of low-energy electron matter wave optics.

6 Summary

This thesis explores the ionization and subsequent control of electrons with intense near-infrared laser pulses from the atomic length scale up to the sub-millimeter regime. Both all-optical measurements and direct electron detection were used as complementary approaches. The temporal and spatial gradients of the light field envelopes lead to novel phenomena such as recollisions in circularly polarized light, control of the electron emission angle on a nanotip, and strong confinement of the interaction volume in standing waves. As a cumulative work, this thesis is based on four publications, namely

- Publication 3.1: Attosecond real-time observation of recolliding electron trajectories in helium at low laser intensities
- Publication 3.2: Photoelectron tomography with an intra-cavity velocity-map imaging spectrometer at 100 MHz repetition rate
- Publication 3.3: Nanometric probing with a femtosecond, intra-cavity standing wave
- Publication 3.4: Velocity-map imaging with counter-propagating laser pulses.

Publication 3.1 studies the trajectories of slow electrons in the first femtoseconds after ionization with an attosecond XUV pulse. The concept of dipole reconstruction is used to extract time-dependent information from the continuum part of a transient absorption spectrum. The interpretation of the all-optical data in terms of recolliding electron trajectories is supported by TDSE simulations. For the first time, a theoretically predicted recollision channel in circularly polarized light is experimentally demonstrated by exploiting the strong temporal gradient of the few-cycle pulse envelope.

Publication 3.2 introduces the velocity-map imaging (VMI) spectrometer to measure angle-resolved electron spectra resulting from cavity-enhanced above-threshold ionization (ATI). The femtosecond enhancement cavity allows the frequency comb to reach intensities $> 10^{13} \text{ W/cm}^2$ in the focus even though the repetition rate is 100 MHz. Because of the polarization insensitivity, three-dimensional photoelectron angular distributions can be reconstructed by tomography.

Publication 3.3 uses this setup to investigate the photofield electron emission at a tungsten nanotip in a transient standing wave, formed by two counter-propagating pulses in a ring cavity. The strong field gradients of the nanometric node-antinode structure of the standing wave probe the nanotip dependent on its sub-cycle position. FDTD simulations show that the angle of the maximum near field changes continuously with the relative phase of the standing wave. In contrast, there is a discrete set of emission regions corresponding to the crystallographic planes with the lowest work functions. By controlling the phase of the standing wave, the emitting plane can be changed.

Publication 3.4 shows the implications of using standing waves for ATI. Due to the high nonlinearity of the process, the ionization volume is tightly confined to the spatial overlap of the counter-propagating pulses, which is two orders of magnitude smaller than the Rayleigh length. This makes it possible to obtain sharp momentum images even without the electrostatic lens used in the traditional VMI technique. Additionally, due to

constructive interference, the maximum intensity in the antinodes is doubled compared to laser geometries where one pulse contains the total energy.

In the setup of the last publication, the electrons resulting from ATI are in perfect spatiotemporal overlap with an intense standing wave, making it a suitable system to explore the Kapitza-Dirac effect, which is diffraction from a ponderomotive grating of light. Chapter 4 presents unpublished data investigating the high-intensity regime of the Kapitza-Dirac effect for long pulses exceeding 1 ps, focusing on atomic resonances during multiphoton ionization. At shorter pulse durations, the measured electron spectra show also qualitative changes compared to traveling wave ionization. There is a splitting of the slowest electrons and an asymmetry depending on the ionization position relative to the focus, the origins of which remain to be understood.

This work lays the foundation for many potential future studies. The XUV-NIR technique could be applied to molecules or even strongly correlated materials to gain deeper insights into electron dynamics in complex systems. Similarly, the target complexity of intra-cavity experiments could be increased, from atoms to molecules or from metallic nanotips to metasurfaces. Another approach is to increase the complexity of the light field. Experiments with light structured in high-order Hermite-Gaussian modes or optical vortices are feasible, as are pump-probe schemes or even cavity-enhanced non-classical light. A particularly promising approach is the control of electron matter waves. A femtosecond electron interferometer could provide invaluable insights by measuring the phase or decoherence induced by neighboring molecules or surfaces.

In conclusion, this thesis has explored various aspects of ionization and electron control using intense exotic light forms such as few-cycle circularly polarized pulses and transient standing waves. In doing so, it has advanced the current state of research and raised new questions in the ongoing quest to understand our ultrafast quantum world.

Bibliography

- [1] C. Kost, *Study: Levelized cost of electricity - Renewable energy technologies - Fraunhofer ISE*, <https://www.ise.fraunhofer.de/en/publications/studies/cost-of-electricity.html> (visited on 02/06/2025).
- [2] T. H. Maiman, “Stimulated optical radiation in ruby,” *Nature* **187**, 493–494 (1960).
- [3] P. A. Franken, A. E. Hill, C. W. Peters, and G. Weinreich, “Generation of optical harmonics,” *Physical Review Letters* **7**, 118–119 (1961).
- [4] P. Agostini, F. Fabre, G. Mainfray, G. Petite, and N. K. Rahman, “Free-free transitions following six-photon ionization of xenon atoms,” *Physical Review Letters* **42**, 1127–1130 (1979).
- [5] P. Agostini, J. Kupersztych, L. A. Lompré, G. Petite, and F. Yergeau, “Direct evidence of ponderomotive effects via laser pulse duration in above-threshold ionization,” *Physical Review A* **36**, 4111–4114 (1987).
- [6] H. G. Muller, H. B. van Linden van den Heuvell, P. Agostini, G. Petite, A. Antonetti, M. Franco, and A. Migus, “Multiphoton ionization of xenon with 100-fs laser pulses,” *Physical Review Letters* **60**, 565–568 (1988).
- [7] L. V. Keldysh, “Ionization in the field of a strong electromagnetic wave,” *Journal of Experimental and Theoretical Physics* **20**, 1307–1314 (1965).
- [8] M. Ferray, A. L’Huillier, X. F. Li, L. A. Lompre, G. Mainfray, and C. Manus, “Multiple-harmonic conversion of 1064 nm radiation in rare gases,” *Journal of Physics B: Atomic, Molecular and Optical Physics* **21**, L31 (1988).
- [9] A. l’Huillier, L. A. Lompre, G. Mainfray, and C. Manus, “Multiply charged ions induced by multiphoton absorption in rare gases at 0.53 micrometers,” *Physical Review A* **27**, 2503–2512 (1983).
- [10] D. N. Fittinghoff, P. R. Bolton, B. Chang, and K. C. Kulander, “Observation of nonsequential double ionization of helium with optical tunneling,” *Physical Review Letters* **69**, 2642–2645 (1992).
- [11] P. B. Corkum, “Plasma perspective on strong field multiphoton ionization,” *Physical Review Letters* **71**, 1994–1997 (1993).
- [12] M. Lewenstein, P. Balcou, M. Y. Ivanov, A. L’Huillier, and P. B. Corkum, “Theory of high-harmonic generation by low-frequency laser fields,” *Physical Review A* **49**, 2117–2132 (1994).
- [13] M. Lewenstein, K. C. Kulander, K. J. Schafer, and P. H. Bucksbaum, “Rings in above-threshold ionization: A quasiclassical analysis,” *Physical Review A* **51**, 1495–1507 (1995).
- [14] Nobel Prize Outreach, *The Nobel Prize in Physics 2023*, (2023) <https://www.nobelprize.org/prizes/physics/2023/summary/> (visited on 01/29/2025).

- [15] E. Goulielmakis, Z.-H. Loh, A. Wirth, R. Santra, N. Rohringer, V. S. Yakovlev, S. Zherebtsov, T. Pfeifer, A. M. Azzeer, M. F. Kling, S. R. Leone, and F. Krausz, “Real-time observation of valence electron motion,” *Nature* **466**, 739–743 (2010).
- [16] A. R. Beck, D. M. Neumark, and S. R. Leone, “Probing ultrafast dynamics with attosecond transient absorption,” *Chemical Physics Letters* **624**, 119–130 (2015).
- [17] M. Wu, S. Chen, S. Camp, K. J. Schafer, and M. B. Gaarde, “Theory of strong-field attosecond transient absorption,” *Journal of Physics B: Atomic, Molecular and Optical Physics* **49**, 062003 (2016).
- [18] H. Wang, M. Chini, S. Chen, C.-H. Zhang, F. He, Y. Cheng, Y. Wu, U. Thumm, and Z. Chang, “Attosecond time-resolved autoionization of argon,” *Physical Review Letters* **105**, 143002 (2010).
- [19] C. Ott, A. Kaldun, L. Argenti, P. Raith, K. Meyer, M. Laux, Y. Zhang, A. Blättermann, S. Hagstotz, T. Ding, R. Heck, J. Madroño, F. Martín, and T. Pfeifer, “Reconstruction and control of a time-dependent two-electron wave packet,” *Nature* **516**, 374–378 (2014).
- [20] M. Lucchini, A. Ludwig, T. Zimmermann, L. Kasmi, J. Herrmann, A. Scrinzi, A. S. Landsman, L. Gallmann, and U. Keller, “Anisotropic emission in quantum-beat spectroscopy of helium excited states,” *Physical Review A* **91**, 063406 (2015).
- [21] J. E. Bækhoj and L. B. Madsen, “Light-induced structures in attosecond transient-absorption spectroscopy of molecules,” *Physical Review A* **92**, 023407 (2015).
- [22] Y. Cheng, M. Chini, X. Wang, A. González-Castrillo, A. Palacios, L. Argenti, F. Martín, and Z. Chang, “Reconstruction of an excited-state molecular wave packet with attosecond transient absorption spectroscopy,” *Physical Review A* **94**, 023403 (2016).
- [23] M. Schultze, E. M. Bothschafter, A. Sommer, S. Holzner, W. Schweinberger, M. Fiess, M. Hofstetter, R. Kienberger, V. Apalkov, V. S. Yakovlev, M. I. Stockman, and F. Krausz, “Controlling dielectrics with the electric field of light,” *Nature* **493**, 75–78 (2013).
- [24] N. Di Palo, G. Inzani, G. L. Dolso, M. Talarico, S. Bonetti, and M. Lucchini, “Attosecond absorption and reflection spectroscopy of solids,” *APL Photonics* **9**, 020901 (2024).
- [25] C. Ott, A. Kaldun, P. Raith, K. Meyer, M. Laux, J. Evers, C. H. Keitel, C. H. Greene, and T. Pfeifer, “Lorentz meets Fano in spectral line shapes: A universal phase and its laser control,” *Science* **340**, 716–720 (2013).
- [26] V. Stooß, S. Cavaletto, S. Donsa, A. Blättermann, P. Birk, C. Keitel, I. Brezinová, J. Burgdörfer, C. Ott, and T. Pfeifer, “Real-time reconstruction of the strong-field-driven dipole response,” *Physical Review Letters* **121**, 173005 (2018).
- [27] D. Roy and D. Tremblay, “Design of electron spectrometers,” *Reports on Progress in Physics* **53**, 1621 (1990).
- [28] J. Ullrich, R. Moshhammer, R. Dörner, O. Jagutzki, V. Mergel, H. Schmidt-Böcking, and L. Spielberger, “Recoil-ion momentum spectroscopy,” *Journal of Physics B: Atomic, Molecular and Optical Physics* **30**, 2917 (1997).

- [29] J. Ullrich, R. Moshhammer, A. Dorn, R. Dörner, L. P. H. Schmidt, and H. Schmidt-Böcking, “Recoil-ion and electron momentum spectroscopy: Reaction-microscopes,” *Reports on Progress in Physics* **66**, 1463 (2003).
- [30] D. H. Parker and A. T. J. B. Eppink, “Photoelectron and photofragment velocity map imaging of state-selected molecular oxygen dissociation/ionization dynamics,” *The Journal of Chemical Physics* **107**, 2357–2362 (1997).
- [31] T. Remetter, P. Johnsson, J. Mauritsson, K. Varjú, Y. Ni, F. Lépine, E. Gustafsson, M. Kling, J. Khan, R. López-Martens, K. J. Schafer, M. J. J. Vrakking, and A. L’Huillier, “Attosecond electron wave packet interferometry,” *Nature Physics* **2**, 323–326 (2006).
- [32] J. Mauritsson, P. Johnsson, E. Mansten, M. Swoboda, T. Ruchon, A. L’Huillier, and K. J. Schafer, “Coherent electron scattering captured by an attosecond quantum stroboscope,” *Physical Review Letters* **100**, 073003 (2008).
- [33] Y. Huismans, A. Rouzée, A. Gijsbertsen, J. H. Jungmann, A. S. Smolkowska, P. S. W. M. Logman, F. Lépine, C. Cauchy, S. Zamith, T. Marchenko, J. M. Bakker, G. Berden, B. Redlich, A. F. G. van der Meer, H. G. Muller, W. Vermin, K. J. Schafer, M. Spanner, M. Y. Ivanov, O. Smirnova, D. Bauer, S. V. Popruzhenko, and M. J. J. Vrakking, “Time-resolved holography with photoelectrons,” *Science* **331**, 61–64 (2011).
- [34] G. Sansone, F. Kelkensberg, J. F. Pérez-Torres, F. Morales, M. F. Kling, W. Siu, O. Ghafur, P. Johnsson, M. Swoboda, E. Benedetti, F. Ferrari, F. Lépine, J. L. Sanz-Vicario, S. Zherebtsov, I. Znakovskaya, A. L’Huillier, M. Y. Ivanov, M. Nisoli, F. Martín, and M. J. J. Vrakking, “Electron localization following attosecond molecular photoionization,” *Nature* **465**, 763–766 (2010).
- [35] J. Itatani, J. Levesque, D. Zeidler, H. Niikura, H. Pépin, J. C. Kieffer, P. B. Corkum, and D. M. Villeneuve, “Tomographic imaging of molecular orbitals,” *Nature* **432**, 867–871 (2004).
- [36] S. Haessler, J. Caillat, and P. Salières, “Self-probing of molecules with high harmonic generation,” *Journal of Physics B: Atomic, Molecular and Optical Physics* **44**, 203001 (2011).
- [37] D. Shafir, H. Soifer, B. D. Bruner, M. Dagan, Y. Mairesse, S. Patchkovskii, M. Y. Ivanov, O. Smirnova, and N. Dudovich, “Resolving the time when an electron exits a tunnelling barrier,” *Nature* **485**, 343–346 (2012).
- [38] T. T. Luu, M. Garg, S. Y. Kruchinin, A. Moulet, M. T. Hassan, and E. Goulielmakis, “Extreme ultraviolet high-harmonic spectroscopy of solids,” *Nature* **521**, 498–502 (2015).
- [39] J. Nauta, J.-H. Oelmann, A. Ackermann, P. Knauer, R. Pappenberger, A. Borodin, I. S. Muhammad, H. Ledwa, T. Pfeifer, and J. R. C. López-Urrutia, “100 MHz frequency comb for low-intensity multi-photon studies: Intra-cavity velocity-map imaging of xenon,” *Optics Letters* **45**, 2156–2159 (2020).
- [40] R. J. Jones, K. D. Moll, M. J. Thorpe, and J. Ye, “Phase-coherent frequency combs in the vacuum ultraviolet via high-harmonic generation inside a femtosecond enhancement cavity,” *Physical Review Letters* **94**, 193201 (2005).

- [41] C. Gohle, T. Udem, M. Herrmann, J. Rauschenberger, R. Holzwarth, H. A. Schuessler, F. Krausz, and T. W. Hänsch, “A frequency comb in the extreme ultraviolet,” *Nature* **436**, 234–237 (2005).
- [42] J. Nauta, “An extreme-ultraviolet frequency comb enabling frequency metrology with highly charged ions,” PhD thesis (Ruprecht-Karls-Universität Heidelberg, July 29, 2020).
- [43] A. Ozawa and Y. Kobayashi, “VUV frequency-comb spectroscopy of atomic xenon,” *Physical Review A* **87**, 022507 (2013).
- [44] E. Peik and C. Tamm, “Nuclear laser spectroscopy of the 3.5 eV transition in Th-229,” *Europhysics Letters (EPL)* **61**, 181–186 (2003).
- [45] S. Kraemer, J. Moens, M. Athanasakis-Kaklamanakis, S. Bara, K. Beeks, P. Chhetri, K. Chrysalidis, A. Claessens, T. E. Cocolios, J. G. M. Correia, H. D. Witte, R. Ferrer, S. Geldhof, R. Heinke, N. Hosseini, M. Huyse, U. Köster, Y. Kudryavtsev, M. Laatiaoui, R. Lica, G. Magchiels, V. Manea, C. Merckling, L. M. C. Pereira, S. Raeder, T. Schumm, S. Sels, P. G. Thirolf, S. M. Tunhuma, P. Van Den Bergh, P. Van Duppen, A. Vantomme, M. Verlinde, R. Villarreal, and U. Wahl, “Observation of the radiative decay of the 229Th nuclear clock isomer,” *Nature* **617**, 706–710 (2023).
- [46] C. Zhang, T. Ooi, J. S. Higgins, J. F. Doyle, L. von der Wense, K. Beeks, A. Leitner, G. A. Kazakov, P. Li, P. G. Thirolf, T. Schumm, and J. Ye, “Frequency ratio of the 229mTh nuclear isomeric transition and the 87Sr atomic clock,” *Nature* **633**, 63–70 (2024).
- [47] C. Lyu, C. H. Keitel, and Z. Harman, “Ultrastable and ultra-accurate clock transitions in open-shell highly charged ions,” *Communications Physics* **8**, 3 (2025).
- [48] J. Nauta, A. Borodin, H. B. Ledwa, J. Stark, M. Schwarz, L. Schmöger, P. Micke, J. R. C. López-Urrutia, and T. Pfeifer, “Towards precision measurements on highly charged ions using a high harmonic generation frequency comb,” *Nuclear Instruments and Methods in Physics Research Section B: Beam Interactions with Materials and Atoms* **408**, 285–288 (2017).
- [49] J.-H. Oelmann, “Highly nonlinear light-matter interaction using cavity-enhanced frequency combs,” PhD thesis (Ruprecht-Karls-Universität Heidelberg, Apr. 19, 2023).
- [50] A. Hartung, S. Eckart, S. Brennecke, J. Rist, D. Trabert, K. Fehre, M. Richter, H. Sann, S. Zeller, K. Henrichs, G. Kastirke, J. Hoehl, A. Kalinin, M. S. Schöffler, T. Jahnke, L. P. H. Schmidt, M. Lein, M. Kunitski, and R. Dörner, “Magnetic fields alter strong-field ionization,” *Nature Physics* **15**, 1222–1226 (2019).
- [51] A. Hartung, S. Brennecke, K. Lin, D. Trabert, K. Fehre, J. Rist, M. Schöffler, T. Jahnke, L. P. H. Schmidt, M. Kunitski, M. Lein, R. Dörner, and S. Eckart, “Electric nondipole effect in strong-field ionization,” *Physical Review Letters* **126**, 053202 (2021).
- [52] K. Lin, S. Brennecke, H. Ni, X. Chen, A. Hartung, D. Trabert, K. Fehre, J. Rist, X.-M. Tong, J. Burgdörfer, L. P. H. Schmidt, M. S. Schöffler, T. Jahnke, M. Kunitski, F. He, M. Lein, S. Eckart, and R. Dörner, “Magnetic-field effect in high-order above-threshold ionization,” *Physical Review Letters* **128**, 023201 (2022).

- [53] D. V. Rezvan, K. Klysek, S. Grundmann, A. Pier, N. M. Novikovskiy, N. Strenger, D. Tsitsonis, M. Kircher, I. Vela-Peréz, K. Fehre, F. Trinter, M. S. Schöffler, T. Jahnke, R. Dörner, and P. V. Demekhin, “Observation of nondipole-induced asymmetry in the angular emission distribution of photoelectrons from fixed-in-space CO molecules,” *Physical Review Letters* **129**, 253201 (2022).
- [54] P. L. Kapitza and P. A. M. Dirac, “The reflection of electrons from standing light waves,” *Mathematical Proceedings of the Cambridge Philosophical Society* **29**, 297–300 (1933).
- [55] A. Feist, K. E. Echternkamp, J. Schauss, S. V. Yalunin, S. Schäfer, and C. Ropers, “Quantum coherent optical phase modulation in an ultrafast transmission electron microscope,” *Nature* **521**, 200–203 (2015).
- [56] Y. Morimoto and P. Baum, “Diffraction and microscopy with attosecond electron pulse trains,” *Nature Physics* **14**, 252–256 (2018).
- [57] A. Ryabov, J. W. Thurner, D. Nabben, M. V. Tsarev, and P. Baum, “Attosecond metrology in a continuous-beam transmission electron microscope,” *Science Advances* **6**, eabb1393 (2020).
- [58] D. Nabben, J. Kuttruff, L. Stolz, A. Ryabov, and P. Baum, “Attosecond electron microscopy of sub-cycle optical dynamics,” *Nature* **619**, 63–67 (2023).
- [59] F. J. García de Abajo and C. Ropers, “Spatiotemporal electron beam focusing through parallel interactions with shaped optical fields,” *Physical Review Letters* **130**, 246901 (2023).
- [60] T. Bucher, H. Nahari, H. Herzig Sheinfux, R. Ruimy, A. Niedermayr, R. Dahan, Q. Yan, Y. Adiv, M. Yannai, J. Chen, Y. Kurman, S. T. Park, D. J. Masiel, E. Janzen, J. H. Edgar, F. Carbone, G. Bartal, S. Tsesses, F. H. L. Koppens, G. M. Vanacore, and I. Kaminer, “Coherently amplified ultrafast imaging using a free-electron interferometer,” *Nature Photonics* **18**, 809–815 (2024).
- [61] J. H. Gaida, H. Lourenço-Martins, M. Sivis, T. Rittmann, A. Feist, F. J. García de Abajo, and C. Ropers, “Attosecond electron microscopy by free-electron homodyne detection,” *Nature Photonics*, 1–7 (2024).
- [62] K. Lin, S. Eckart, H. Liang, A. Hartung, S. Jacob, Q. Ji, L. P. H. Schmidt, M. S. Schöffler, T. Jahnke, M. Kunitski, and R. Dörner, “Ultrafast Kapitza-Dirac effect,” *Science* **383**, 1467–1470 (2024).
- [63] U. Keller, *Ultrafast lasers*, 1868-4513 (Springer International Publishing, 2021).
- [64] J. D. Pickering, *Ultrafast lasers and optics for experimentalists*, 2053-2563 (IOP Publishing, 2021).
- [65] J. Ye and S. T. Cundiff, *Femtosecond optical frequency comb: Principle, operation and applications* (Springer-Verlag US, 2005).
- [66] E. Treacy, “Optical pulse compression with diffraction gratings,” *IEEE Journal of Quantum Electronics* **5**, 454–458 (1969).
- [67] R. L. Fork, O. E. Martinez, and J. P. Gordon, “Negative dispersion using pairs of prisms,” *Optics Letters* **9**, 150–152 (1984).
- [68] R. Szipöcs, K. Ferencz, C. Spielmann, and F. Krausz, “Chirped multilayer coatings for broadband dispersion control in femtosecond lasers,” *Optics Letters* **19**, 201–203 (1994).

- [69] R. L. Fork, C. H. B. Cruz, P. C. Becker, and C. V. Shank, “Compression of optical pulses to six femtoseconds by using cubic phase compensation,” *Optics Letters* **12**, 483–485 (1987).
- [70] D. H. Sutter, G. Steinmeyer, L. Gallmann, N. Matuschek, F. Morier-Genoud, U. Keller, V. Scheuer, G. Angelow, and T. Tschudi, “Semiconductor saturable-absorber mirror-assisted Kerr-lens mode-locked Ti:sapphire laser producing pulses in the two-cycle regime,” *Optics Letters* **24**, 631–633 (1999).
- [71] A. J. DeMaria, D. A. Stetser, and H. Heynau, “Self mode-locking of lasers with saturable absorbers,” *Applied Physics Letters* **8**, 174–176 (1966).
- [72] U. Keller, “Ultrafast solid-state laser oscillators: A success story for the last 20 years with no end in sight,” *Applied Physics B* **100**, 15–28 (2010).
- [73] D. E. Spence, P. N. Kean, and W. Sibbett, “60-fsec pulse generation from a self-mode-locked Ti:sapphire laser,” *Optics Letters* **16**, 42–44 (1991).
- [74] S. T. Cundiff, “Phase stabilization of ultrashort optical pulses,” *Journal of Physics D: Applied Physics* **35**, R43 (2002).
- [75] H. Telle, G. Steinmeyer, A. Dunlop, J. Stenger, D. Sutter, and U. Keller, “Carrier-envelope offset phase control: A novel concept for absolute optical frequency measurement and ultrashort pulse generation,” *Applied Physics B* **69**, 327–332 (1999).
- [76] S. A. Diddams, D. J. Jones, J. Ye, S. T. Cundiff, J. L. Hall, J. K. Ranka, R. S. Windeler, R. Holzwarth, T. Udem, and T. W. Hänsch, “Direct link between microwave and optical frequencies with a 300 THz femtosecond laser comb,” *Physical Review Letters* **84**, 5102–5105 (2000).
- [77] D. J. Jones, S. A. Diddams, J. K. Ranka, A. Stentz, R. S. Windeler, J. L. Hall, and S. T. Cundiff, “Carrier-envelope phase control of femtosecond mode-locked lasers and direct optical frequency synthesis,” *Science* **288**, 635–639 (2000).
- [78] T. W. Hänsch, “Nobel lecture: Passion for precision,” *Reviews of Modern Physics* **78**, 1297–1309 (2006).
- [79] J. L. Hall, “Nobel lecture: Defining and measuring optical frequencies,” *Reviews of Modern Physics* **78**, 1279–1295 (2006).
- [80] J. K. Ranka, R. S. Windeler, and A. J. Stentz, “Visible continuum generation in air-silica microstructure optical fibers with anomalous dispersion at 800 nm,” *Optics Letters* **25**, 25–27 (2000).
- [81] N. Picqué and T. W. Hänsch, “Frequency comb spectroscopy,” *Nature Photonics* **13**, 146–157 (2019).
- [82] A. Cingöz, D. C. Yost, T. K. Allison, A. Ruehl, M. E. Fermann, I. Hartl, and J. Ye, “Direct frequency comb spectroscopy in the extreme ultraviolet,” *Nature* **482**, 68–71 (2012).
- [83] J. Nauta, J.-H. Oelmann, A. Borodin, A. Ackermann, P. Knauer, I. S. Muhammad, R. Pappenberger, T. Pfeifer, and J. R. C. López-Urrutia, “XUV frequency comb production with an astigmatism-compensated enhancement cavity,” *Optics Express* **29**, 2624–2636 (2021).
- [84] I. Pupeza, C. Zhang, M. Högner, and J. Ye, “Extreme-ultraviolet frequency combs for precision metrology and attosecond science,” *Nature Photonics* **15**, 175–186 (2021).

- [85] I. Coddington, N. Newbury, and W. Swann, “Dual-comb spectroscopy,” *Optica* **3**, 414–426 (2016).
- [86] T. Fortier and E. Baumann, “20 years of developments in optical frequency comb technology and applications,” *Communications Physics* **2**, 1–16 (2019).
- [87] J. L. Klocke, M. Mangold, P. Allmendinger, A. Hugi, M. Geiser, P. Jouy, J. Faist, and T. Kottke, “Single-shot sub-microsecond mid-infrared spectroscopy on protein reactions with quantum cascade laser frequency combs,” *Analytical Chemistry* **90**, 10494–10500 (2018).
- [88] H. W. Norman Hodgson, *Laser resonators and beam propagation: Fundamentals, advanced concepts, applications*, 2nd ed. (Springer Berlin, Heidelberg, Dec. 19, 2005).
- [89] D. Meschede, *Optik, Licht und Laser*, 2nd ed. (Vieweg+Teubner Verlag Wiesbaden, 2005), pp. 196–209.
- [90] M. Pollnau and M. Eichhorn, “Spectral coherence, part I: Passive-resonator linewidth, fundamental laser linewidth, and Schawlow-Townes approximation,” *Progress in Quantum Electronics* **72**, 100255 (2020).
- [91] A. K. Mills, T. J. Hammond, M. H. C. Lam, and D. J. Jones, “XUV frequency combs via femtosecond enhancement cavities,” *Journal of Physics B: Atomic, Molecular and Optical Physics* **45**, 142001 (2012).
- [92] N. Lilienfein, C. Hofer, S. Holzberger, C. Matzer, P. Zimmermann, M. Trubetskov, V. Pervak, and I. Pupeza, “Enhancement cavities for few-cycle pulses,” *Optics Letters* **42**, 271–274 (2017).
- [93] A. Surzhykov and R. Müller, *Lecture notes: Light-matter interaction 1*, https://www.ptb.de/cms/fileadmin/internet/institute/fpm/LMI_2018/Skript/lecture_strong_fields.pdf, Accessed: 2025-23-01, 2018.
- [94] D. Bauer, D. B. Milošević, and W. Becker, “Strong-field approximation for intense-laser-atom processes: The choice of gauge,” *Physical Review A* **72**, 023415 (2005).
- [95] J. Zhang and T. Nakajima, “Influence of coulomb potential for photoionization of H atoms in an elliptically polarized laser field: velocity gauge versus length gauge,” *Physical Review A* **77**, 043417 (2008).
- [96] F. Grossmann, *Theoretical femtosecond physics: Atoms and molecules in strong laser fields* (Springer Cham, Apr. 4, 2018).
- [97] Q. Su and J. H. Eberly, “Model atom for multiphoton physics,” *Physical Review A* **44**, 5997–6008 (1991).
- [98] W. Witschel, “Ordered operator expansions by comparison,” *Journal of Physics A: Mathematical and General* **8**, 143 (1975).
- [99] P. Bader, S. Blanes, and F. Casas, “Solving the Schrödinger eigenvalue problem by the imaginary time propagation technique using splitting methods with complex coefficients,” *The Journal of Chemical Physics* **139**, 124117 (2013).
- [100] E. J. Heller, “Time-dependent approach to semiclassical dynamics,” *The Journal of Chemical Physics* **62**, 1544–1555 (1975).
- [101] D. M. Wolkow, “Über eine Klasse von Lösungen der Diracschen Gleichung,” *Zeitschrift für Physik* **94**, 250–260 (1935).

- [102] J. H. Bauer, “Keldysh theory re-examined,” *Journal of Physics B: Atomic, Molecular and Optical Physics* **49**, 145601 (2016).
- [103] M. V. Fedorov, “L. V. Keldysh’s ‘Ionization in the field of a strong electromagnetic wave’ and modern physics of atomic interaction with a strong laser field,” *Journal of Experimental and Theoretical Physics* **122**, 449–455 (2016).
- [104] H. G. Muller, A. Tip, and M. J. v. d. Wiel, “Ponderomotive force and AC stark shift in multiphoton ionisation,” *Journal of Physics B: Atomic and Molecular Physics* **16**, L679 (1983).
- [105] P. Kruit, J. Kimman, H. G. Muller, and M. J. van der Wiel, “Electron spectra from multiphoton ionization of xenon at 1064, 532, and 355 nm,” *Physical Review A* **28**, 248–255 (1983).
- [106] E. Fiordilino and M. H. Mittleman, “Kinematics of multiphoton ionisation in a laser pulse,” *Journal of Physics B: Atomic and Molecular Physics* **18**, 4425 (1985).
- [107] T. S. Luk, T. Graber, H. Jara, U. Johann, K. Boyer, and C. K. Rhodes, “Subpicosecond ultraviolet multiphoton electron spectroscopy of rare gases,” *Journal of the Optical Society of America B* **4**, 847–852 (1987).
- [108] J. G. Story, D. I. Duncan, and T. F. Gallagher, “Channel closing in multiphoton ionization of Mg,” *Physical Review A* **49**, 3875–3880 (1994).
- [109] P. Hansch, M. A. Walker, and L. D. Van Woerkom, “Eight- and nine-photon resonances in multiphoton ionization of xenon,” *Physical Review A* **57**, R709–R712 (1998).
- [110] R. R. Freeman, P. H. Bucksbaum, H. Milchberg, S. Darack, D. Schumacher, and M. E. Geusic, “Above-threshold ionization with subpicosecond laser pulses,” *Physical Review Letters* **59**, 1092–1095 (1987).
- [111] M. D. Perry, A. Szoke, and K. C. Kulander, “Resonantly enhanced above-threshold ionization of helium,” *Physical Review Letters* **63**, 1058–1061 (1989).
- [112] P. Agostini, P. Breger, A. L’Huillier, H. G. Muller, G. Petite, A. Antonetti, and A. Migus, “Giant stark shifts in multiphoton ionization,” *Physical Review Letters* **63**, 2208–2211 (1989).
- [113] H. Rottke, B. Wolff, M. Brickwedde, D. Feldmann, and K. H. Welge, “Multiphoton ionization of atomic hydrogen in intense subpicosecond laser pulses,” *Physical Review Letters* **64**, 404–407 (1990).
- [114] G. N. Gibson, R. R. Freeman, and T. J. McIlrath, “Verification of the dominant role of resonant enhancement in short-pulse multiphoton ionization,” *Physical Review Letters* **69**, 1904–1907 (1992).
- [115] L. Pan, L. Armstrong, and J. H. Eberly, “Comments on the effect of the ponderomotive potential in the above-threshold ionization processes,” *Journal of the Optical Society of America B* **3**, 1319–1322 (1986).
- [116] S. Li, D. Sierra-Costa, M. J. Michie, I. Ben-Itzhak, and M. Dantus, “Control of electron recollision and molecular nonsequential double ionization,” *Communications Physics* **3**, 1–8 (2020).
- [117] J. Biegert, F. Calegari, N. Dudovich, F. Quéré, and M. Vrakking, “Attosecond technology(ies) and science,” *Journal of Physics B: Atomic, Molecular and Optical Physics* **54**, 070201 (2021).

- [118] S. Augst, D. D. Meyerhofer, D. Strickland, and S. L. Chin, “Laser ionization of noble gases by Coulomb-barrier suppression,” *Journal of the Optical Society of America B* **8**, 858–867 (1991).
- [119] A. M. Perelomov, V. S. Popov, and M. V. Terent’ev, “Ionization of atoms in an alternating electric field,” *Soviet Journal of Experimental and Theoretical Physics* **23**, 924 (1966).
- [120] M. V. Ammosov, N. B. Delone, and V. P. Krainov, “Tunnel ionization of complex atoms and of atomic ions in an alternating electromagnetic field,” *Soviet Journal of Experimental and Theoretical Physics* **64**, 1191 (1986).
- [121] F. A. Ilkov, J. E. Decker, and S. L. Chin, “Ionization of atoms in the tunnelling regime with experimental evidence using Hg atoms,” *Journal of Physics B: Atomic, Molecular and Optical Physics* **25**, 4005 (1992).
- [122] Z. Chang, *Fundamentals of attosecond optics* (CRC Press, 2011), pp. 176–199.
- [123] H. R. Reiss, “Effect of an intense electromagnetic field on a weakly bound system,” *Physical Review A* **22**, 1786–1813 (1980).
- [124] H. R. Reiss, “Limits on tunneling theories of strong-field ionization,” *Physical Review Letters* **101**, 043002 (2008).
- [125] M. J. Southon, *Field emission and field ionization*, edited by J. J. Hren and S. Ranganathan (Springer US, Boston, MA, 1968), pp. 6–27.
- [126] M. Schenk, M. Krüger, and P. Hommelhoff, “Strong-field above-threshold photoemission from sharp metal tips,” *Physical Review Letters* **105**, 257601 (2010).
- [127] R. H. Fowler and L. Nordheim, “Electron emission in intense electric fields,” *Proceedings of the Royal Society of London. Series A, Containing Papers of a Mathematical and Physical Character* **119**, 173–181 (1928).
- [128] R. G. Forbes, “Refining the application of Fowler–Nordheim theory,” *Ultramicroscopy* **79**, 11–23 (1999).
- [129] R. G. Forbes and J. H. Deane, “Reformulation of the standard theory of Fowler–Nordheim tunnelling and cold field electron emission,” *Proceedings of the Royal Society A: Mathematical, Physical and Engineering Sciences* **463**, 2907–2927 (2007).
- [130] A. Kyritsakis and J. P. Xanthakis, “Derivation of a generalized Fowler–Nordheim equation for nanoscopic field-emitters,” *Proceedings of the Royal Society A: Mathematical, Physical and Engineering Sciences* **471**, 20140811 (2015).
- [131] C. Ropers, D. R. Solli, C. P. Schulz, C. Lienau, and T. Elsaesser, “Localized multiphoton emission of femtosecond electron pulses from metal nanotips,” *Physical Review Letters* **98**, 043907 (2007).
- [132] S. Thomas, G. Wachter, C. Lemell, J. Burgdörfer, and P. Hommelhoff, “Large optical field enhancement for nanotips with large opening angles,” *New Journal of Physics* **17**, 063010 (2015).
- [133] P. Dombi, Z. Pápa, J. Vogelsang, S. V. Yalunin, M. Siviš, G. Herink, S. Schäfer, P. Groß, C. Ropers, and C. Lienau, “Strong-field nano-optics,” *Reviews of Modern Physics* **92**, 025003 (2020).
- [134] L. Wu and L. K. Ang, “Nonequilibrium model of ultrafast laser-induced electron photofield emission from a dc-biased metallic surface,” *Physical Review B* **78**, 224112 (2008).

- [135] F. V. Bunkin and M. V. Fedorov, “Cold emission of electrons from the surface of a metal in a strong radiation field,” *Journal of Experimental and Theoretical Physics* **21**, 896 (1965).
- [136] P. Hommelhoff, Y. Sortais, A. Aghajani-Talesh, and M. A. Kasevich, “Field emission tip as a nanometer source of free electron femtosecond pulses,” *Physical Review Letters* **96**, 077401 (2006).
- [137] M. Krüger, C. Lemell, G. Wachter, J. Burgdörfer, and P. Hommelhoff, “Attosecond physics phenomena at nanometric tips,” *Journal of Physics B: Atomic, Molecular and Optical Physics* **51**, 172001 (2018).
- [138] D. L. Freimund, K. Aflatooni, and H. Batelaan, “Observation of the Kapitza–Dirac effect,” *Nature* **413**, 142–143 (2001).
- [139] H. Batelaan, “The Kapitza-Dirac effect,” *Contemporary Physics* **41**, 369–381 (2000).
- [140] H. Batelaan, “Colloquium: illuminating the Kapitza-Dirac effect with electron matter optics,” *Reviews of Modern Physics* **79**, 929–941 (2007).
- [141] P. L. Gould, G. A. Ruff, and D. E. Pritchard, “Diffraction of atoms by light: the near-resonant Kapitza-Dirac effect,” *Physical Review Letters* **56**, 827–830 (1986).
- [142] O. Nairz, B. Brezger, M. Arndt, and A. Zeilinger, “Diffraction of complex molecules by structures made of light,” *Physical Review Letters* **87**, 160401 (2001).
- [143] E. M. Rasel, M. K. Oberthaler, H. Batelaan, J. Schmiedmayer, and A. Zeilinger, “Atom wave interferometry with diffraction gratings of light,” *Physical Review Letters* **75**, 2633–2637 (1995).
- [144] A. D. Cronin, J. Schmiedmayer, and D. E. Pritchard, “Optics and interferometry with atoms and molecules,” *Reviews of Modern Physics* **81**, 1051–1129 (2009).
- [145] B. Gadway, D. Pertot, R. Reimann, M. G. Cohen, and D. Schneble, “Analysis of Kapitza-Dirac diffraction patterns beyond the Raman-Nath regime,” *Optics Express* **17**, 19173–19180 (2009).
- [146] V. Stooß, M. Hartmann, P. Birk, G. D. Borisova, T. Ding, A. Blättermann, C. Ott, and T. Pfeifer, “XUV-beamline for attosecond transient absorption measurements featuring a broadband common beam-path time-delay unit and in situ reference spectrometer for high stability and sensitivity,” *Review of Scientific Instruments* **90**, 053108 (2019).
- [147] P. Birk, V. Stooß, M. Hartmann, G. D. Borisova, A. Blättermann, T. Heldt, K. Bartschat, C. Ott, and T. Pfeifer, “Attosecond transient absorption of a continuum threshold,” *Journal of Physics B: Atomic, Molecular and Optical Physics* **53**, 124002 (2020).
- [148] M. Möller, Y. Cheng, S. D. Khan, B. Zhao, K. Zhao, M. Chini, G. G. Paulus, and Z. Chang, “Dependence of high-order-harmonic-generation yield on driving-laser ellipticity,” *Physical Review A* **86**, 011401 (2012).
- [149] M. Wollenhaupt, M. Krug, J. Köhler, T. Bayer, C. Sarpe-Tudoran, and T. Baumert, “Three-dimensional tomographic reconstruction of ultrashort free electron wave packets,” *Applied Physics B* **95**, 647–651 (2009).
- [150] P. H. Bucksbaum, D. W. Schumacher, and M. Bashkansky, “High-intensity Kapitza-Dirac effect,” *Physical Review Letters* **61**, 1182–1185 (1988).

- [151] J. Chen, J. G. Story, and R. G. Hulet, “Evolution of atomic motion in an intense standing wave,” *Physical Review A* **47**, 2128–2138 (1993).
- [152] H. Helm, N. Bjerre, M. J. Dyer, D. L. Huestis, and M. Saeed, “Images of photoelectrons formed in intense laser fields,” *Physical Review Letters* **70**, 3221–3224 (1993).
- [153] V. Schyja, T. Lang, and H. Helm, “Channel switching in above-threshold ionization of xenon,” *Physical Review A* **57**, 3692–3697 (1998).
- [154] J. R. Dormand and P. J. Prince, “A family of embedded Runge-Kutta formulae,” *Journal of Computational and Applied Mathematics* **6**, 19–26 (1980).
- [155] T. Zuo, A. D. Bandrauk, and P. B. Corkum, “Laser-induced electron diffraction: A new tool for probing ultrafast molecular dynamics,” *Chemical Physics Letters* **259**, 313–320 (1996).
- [156] S. Hu, “Attosecond dynamics of dipole-coupled doubly excited states in helium,” PhD thesis (Ruprecht-Karls-Universität Heidelberg, Dec. 2023).
- [157] W. Becker, F. Grasbon, R. Kopold, D. B. Milošević, G. G. Paulus, and H. Walther, “Above-threshold ionization: From classical features to quantum effects,” in , Vol. 48 (Academic Press, 2002), pp. 35–98.
- [158] J. Dubois, C. Chandre, and T. Uzer, “Envelope-driven recollisions triggered by an elliptically polarized pulse,” *Physical Review Letters* **124**, 253203 (2020).
- [159] M. Meckel, D. Comtois, D. Zeidler, A. Staudte, D. Pavicic, H. C. Bandulet, H. Pépin, J. C. Kieffer, R. Dörner, D. M. Villeneuve, and P. B. Corkum, “Laser-induced electron tunneling and diffraction,” *Science* **320**, 1478–1482 (2008).
- [160] K. Chirvi and J. Biegert, “Laser-induced electron diffraction: Imaging of a single gas-phase molecular structure with one of its own electrons,” *Structural Dynamics* **11**, 041301 (2024).
- [161] S. Goncharov, K. Fritsch, and O. Pronin, “Amplification-free GW-level, 150 W, 14 MHz, and 8 fs thin-disk laser based on compression in multipass cells,” *Optics Letters* **49**, 2717–2720 (2024).
- [162] S. Ebel and N. Talebi, “Inelastic electron scattering at a single-beam structured light wave,” *Communications Physics* **6**, 1–8 (2023).
- [163] A. Rudelis, B. Hu, J. Sinclair, E. Bytyqi, A. Schwartzman, R. Brenes, T. K. Zhitomirsky, M. Schleier-Smith, and V. Vuletić, “Degradation of Ta₂O₅ / SiO₂ dielectric cavity mirrors in ultra-high vacuum,” *Optics Express* **31**, 39670–39680 (2023).
- [164] B. Bernhardt, A. Ozawa, A. Vernaleken, I. Pupeza, J. Kaster, Y. Kobayashi, R. Holzwarth, E. Fill, F. Krausz, T. W. Hänsch, and T. Udem, “Vacuum ultraviolet frequency combs generated by a femtosecond enhancement cavity in the visible,” *Optics Letters* **37**, 503–505 (2012).
- [165] G. Porat, C. M. Heyl, S. B. Schoun, C. Benko, N. Dörre, K. L. Corwin, and J. Ye, “Phase-matched extreme-ultraviolet frequency-comb generation,” *Nature Photonics* **12**, 387–391 (2018).
- [166] D. Pengel, S. Kerbstadt, D. Johannmeyer, L. Englert, T. Bayer, and M. Wollenhaupt, “Electron vortices in femtosecond multiphoton ionization,” *Physical Review Letters* **118**, 053003 (2017).

- [167] E. Ruska, “The development of the electron microscope and of electron microscopy,” *Reviews of Modern Physics* **59**, 627–638 (1987).
- [168] M. von Ardenne, “Das Elektronen-Rastermikroskop,” *de, Zeitschrift für Physik* **109**, 553–572 (1938).
- [169] T. A. Klar and S. W. Hell, “Subdiffraction resolution in far-field fluorescence microscopy,” *Optics Letters* **24**, 954–956 (1999).
- [170] G. Binnig and H. Rohrer, “Scanning tunneling microscopy,” *Surface Science* **126**, 236–244 (1983).
- [171] E. W. Müller, “Die Abhängigkeit der Feldelektronenemission von der Austrittsarbeit,” *de, Zeitschrift für Physik* **102**, 734–761 (1936).
- [172] E. W. Müller, “Das Feldionenmikroskop,” *de, Zeitschrift für Physik* **131**, 136–142 (1951).
- [173] S. Hell and E. H. K. Stelzer, “Properties of a 4pi confocal fluorescence microscope,” *Journal of the Optical Society of America A* **9**, 2159–2166 (1992).
- [174] B. Bailey, D. L. Farkas, D. L. Taylor, and F. Lanni, “Enhancement of axial resolution in fluorescence microscopy by standing-wave excitation,” *Nature* **366**, 44–48 (1993).
- [175] W. Denk, J. H. Strickler, and W. W. Webb, “Two-photon laser scanning fluorescence microscopy,” *Science* **248**, 73–76 (1990).
- [176] J. Chaves, *Introduction to nonimaging optics* (CRC Press, Dec. 19, 2017), 772 pp.
- [177] S. T. Park, M. Lin, and A. H. Zewail, “Photon-induced near-field electron microscopy (PINEM): Theoretical and experimental,” *New Journal of Physics* **12**, 123028 (2010).
- [178] M. Kozák, T. Eckstein, N. Schönenberger, and P. Hommelhoff, “Inelastic ponderomotive scattering of electrons at a high-intensity optical travelling wave in vacuum,” *Nature Physics* **14**, 121–125 (2018).
- [179] M. Tsarev, J. W. Thurner, and P. Baum, “Nonlinear-optical quantum control of free-electron matter waves,” *Nature Physics* **19**, 1350–1354 (2023).
- [180] M. Kozák and T. Ostatnický, “Asynchronous inelastic scattering of electrons at the ponderomotive potential of optical waves,” *Physical Review Letters* **129**, 024801 (2022).
- [181] W. C.-W. Huang, H. Batelaan, and M. Arndt, “Kapitza-Dirac blockade: A universal tool for the deterministic preparation of non-Gaussian oscillator states,” *Physical Review Letters* **126**, 253601 (2021).
- [182] M. Eldar, Z. Chen, Y. Pan, and M. Krüger, “Self-trapping of slow electrons in the energy domain,” *Physical Review Letters* **132**, 035001 (2024).
- [183] A. P. Synanidis, P. A. D. Gonçalves, C. Ropers, and F. J. G. de Abajo, “Quantum effects in the interaction of low-energy electrons with light,” *Science Advances* **10**, eadp4096 (2024).

Acknowledgments

Diese Arbeit wäre in dieser Form ohne die Unterstützung von einigen Menschen nicht möglich gewesen. Dafür bin ich wahnsinnig dankbar.

Lieber José, dir möchte ich als erstes danken, für die Aufnahme in die EBIT-Gruppe, dafür dass du an den Erfolg dieser Arbeit geglaubt hast und für die vielen Dinge, die ich von dir lernen konnte. Dein großer Erfahrungsschatz über Elektronik, Vakuumtechnik, Konstruktion, Materialien, wissenschaftliches Schreiben, Spektroskopie und alles was ein Experimentalphysiker noch so wissen muss hat diese Arbeit sehr bereichert. Auch wenn wir nicht immer einer Meinung waren, die Diskussionen waren wertvoll und ich schätze sehr die Fürsorge, die du jedem einzelnen Gruppenmitglied entgegenbringst.

Ein großer Dank geht an Selim Jochim für die Bereitschaft die Zweitkorrektur dieser Arbeit zu übernehmen.

Ebenfalls möchte ich mich bei Christian Ott, Jonathan Dubois und Thomas Pfeifer bedanken für die vielen Treffen, bei denen wir gemeinsam daran getüftelt haben die Elektronenrekollisionen besser zu verstehen. Ich habe viel bei diesem Prozess gelernt, auch als es für mich erstmals darum ging die Physik in einen kompakten, konsistenten Artikel zu gießen.

Thomas, dir möchte ich auch noch besonders für die letzten sieben Jahre in deiner Abteilung danken. Ich erinnere mich noch daran, wie du mich damals auf dem Flur willkommen heißen hast, als ich als Praktikant angefangen habe. Du leitest diese Abteilung nicht nur mit einem faszinierenden physikalischen Verständnis, sondern auch mit einer großartigen Wertschätzung jedem einzelnen gegenüber. Vielen Dank dafür.

Diese Arbeit wäre auch nicht möglich gewesen ohne den Support der ganzen Infrastruktur des Instituts. An alle Menschen aus den Werkstätten, der Konstruktion, der Elektronik, der IT und der Verwaltung, die mich unterstützt haben geht ein herzliches Dankeschön!

Lieber Jan, deine Hilfe, dein Zuspruch, dein Einsatz und deine Freundschaft haben diese Arbeit auf ganz besondere Weise ermöglicht. Auch wenn sie manchmal ein bisschen wackeln, sind deine optischen Aufbauten famos und haben für die Ergebnisse dieser Arbeit die Basis gelegt. Ob bei nächtlichen Messabenteuern im Labor, oder beim Bürosnack, durch deine Gesellschaft sind die Probleme kleiner geworden und die Chancen und Erfolge größer. Ich habe so viel von dir, deinen Optik-Kenntnissen, deinem Elan, deinem Optimismus, deiner Sorgfalt und Schaffenskraft gelernt. Danke für alles!

Lieber Lennart, dass du zum XUV-Comb Team dazu gekommen bist, war ein riesiger Glücksfall. Mit deiner strukturierten Arbeit, deiner absoluten Zuverlässigkeit, deiner Geduld, deinem Fleiß und deiner Motivation hast du dieses Experiment wahnsinnig voran gebracht. Vielen Dank für deine große Bereitschaft Verantwortung zu übernehmen und für all deine Hilfe!

Danke Janko, dass du mit deiner Arbeit den Grundstein für dieses Experiment gelegt hast und für deine Geduld mir alle Fragen zu beantworten.

Vielen Dank Lukas für deinen unermüdlichen Einsatz. Es hat mir immer sehr viel Spaß gemacht dich zu betreuen und deine große Neugierde, dein vielfältiges Engagement und deine bemerkenswerte Begeisterungsfähigkeit sind sehr inspirierend.

Acknowledgments

Thank you Anant, for all your hard, diligent work and your help with proofreading.

Danke auch an Thomas und an all die ehemaligen Mitglieder des XUV-Comb Teams Nele, Fiona, Prachi, Nick, Stepan, Roman, Matthias, Hannah und Simon, die meine Zeit an diesem Experiment geprägt haben, sei es im Labor oder am Kickertisch. Es hat Spaß gemacht mit euch zusammen das Experiment voran zu bringen und ich konnte durch die (Mit-)Betreuung eurer Arbeiten viel lernen.

Ebenfalls möchte ich mich bei allen Mitgliedern der EBIT-Gruppe bedanken. Ihr seid nicht nur die fleißigsten KuchenbäckerInnen des Instituts, sondern auch immer hilfsbereit und verlässlich. Danke für die tolle kollegiale Atmosphäre.

Zuletzt möchte ich mich von ganzem Herzen bei meinen Freunden und meiner Familie bedanken, die mich immer unterstützt und begleitet haben. Es tut so gut, dass ich mich immer auf euch verlassen kann.

Danke Anni, für deine riesige Unterstützung, dein Verständnis und deine Liebe.

Danke Nora, dass es dich gibt.

Danke!